EFFECTS OF CONTINUOUS MAGNETIC FIELD MANIPULATION ON HIGH-RESOLUTION EDDY-CURRENT PATTERN FOR ARTIFICIAL PERCEPTION APPLICATIONS

A Dissertation
Presented to
The Academic Faculty

by

Chun-Yeon Lin

In Partial Fulfillment
of the Requirements for the Degree
Doctor of Philosophy in the
School of Mechanical Engineering

Georgia Institute of Technology
December 2017

EFFECTS OF CONTINUOUS MAGNETIC FIELD MANIPULATION ON HIGH-RESOLUTION EDDY-CURRENT PATTERN FOR ARTIFICIAL PERCEPTION APPLICATIONS

Approved by:

Dr. Kok-Meng Lee, Advisor
School of Mechanical Engineering
Georgia Institute of Technology

Dr. Jun Ueda
School of Mechanical Engineering
Georgia Institute of Technology

Dr. Yan Wang
School of Mechanical Engineering
Georgia Institute of Technology

Dr. Boris I. Prilutsky
School of Biological Sciences
Georgia Institute of Technology

Dr. Zhigang Zhu
School of Engineering
The City College of New York

Date Approved: 11/8/2017

[To my parents Chii-Ruey Lin and Ming-Yea Chen]

ACKNOWLEDGEMENTS

I would like to sincerely thank my advisor Dr. Kok-Meng Lee for his exemplary guidance and encouragement during my Ph.D. study. He is knowledgeable and expertise in broad spectrums of mechatronics research and very enthusiasm in instructing his students. To me, he is not only the advisor for my research, but also a mentor in my life in United States. It is also my pleasure thank my reading committee: Dr. Jun Ueda, Dr. Yan Wang, Dr. Boris I. Prilutsky, and Dr. Zhigang Zhu who have provided invaluable advice and suggestions.

I feel lucky that I have the opportunity to participate as Graduate Research Assistant for the National Science Foundation M3C project (EFRI-M3C 1137172) at Georgia Tech and as Summer Intern in the 973 program funded by National Basic Research Program of China at Huazhong University of Science and Technology. This international research experience expands my research application scopes. I would like to acknowledge my current and former colleagues in AIMRL lab, Min Li, Yang Xie, Jiajie Guo, Kun Bai, Jungyoul Lim, Donghai Wang, Bingjie Hao, Lei Li, Yang Huang, Ying Chen, Jingjing Ji, Liman Yang, Wei Wang, Xiao Liang, Xianmin Chen for their assistances on my research and fulfill my Ph.D. life.

Finally, I wish to give my special thanks to my parents, Chii-Ruey Lin and Ming-Yea Chen. My father, a professor in mechanical engineering in Taiwan always inspires me to do some interdisciplinary studies such as mechatronics systems and my mother always encourages me during my Ph.D. study. Without their endless loves and cares, my youthful dream cannot come true.

The financial supports of the National Science Foundation (NSF) EFRI-M3C 1137172, NSF grant number CMMI-1662700, and National Basic Research Program of China (973 Program, Grant No. 2013CB035803), and Taiwan Government Scholarship for Studying Abroad are gratefully acknowledged.

TABLE OF CONTENTS

LIST OF TABLES

LIST OF FIGURES

LIST OF SYMBOLS AND ABBREVIATIONS

Capitalized Symbols

A_0	The input current amplitude constant of the EM
B_{cr}, B_{cz}	r, z direction magnetic flux density contributed by the conductor
B_{er}, B_{ez}	r, z direction magnetic flux density contributed by the EM
B_r, B_z	Magnetic flux density in r, z coordinate system
B_x, B_y, B_z	Magnetic flux density in x, y, z coordinate system
C_E	Current passes through the circular wire
C_a	Absorption coefficient
C_f	Source term
C_t	Damping or mass coefficient (s/m^2)
D_w	Diameter of wire to outer radius of EM
E_ϕ	Tangential direction electric field
E_ℓ	ℓ component electric field
$E_{\ell \mathrm{Re}}$	Real part ℓ component electric field
$E_{\ell \mathrm{Im}}$	Imagine part ℓ component electric field
F_{no}, F_{n1}	Variable of Neumann boundary condition
H	Thickness of the plate to half-length of EM
H_e	Ratio of element thickness to half-length of EM
H_p	Ratio of plate thickness to half-length of EM
J_0	Current density of the EM
$J_1(\bullet)$	Bessel function of the first kind and one order

J_A	Eddy current density determined by the analytical solution
J_E	Uniform current density
L_I	L-axis of Lab color system (brightness)
L_a	a-axis of Lab color system
L_b	b-axis of Lab color system
N_e	Number of electromagnets
N_{fx}, N_{fy}	x, y direction frame pixel numbers
N_{sx}, N_{sy}	x, y direction sensor pixel numbers
N_{ex}, N_{ey}	x, y direction electromagnet numbers
N_i	Number of image pixel
N_w	Number of wire
Q_r	Resistive loss (W/m^3)
R	Element position in r direction to outer radius of EM
R_e	Ratio of element length in r direction to outer radius of the EM
R_p	Ratio of plate radius to outer radius of the EM
Z	Element position in z direction to outer radius of EM
Z_p	Ratio of sensor plate distance to half-length of EM
$\mathbf{A}$	Magnetic vector potential
$\mathbf{A}_{\mathrm{EM}}$	The input current matrix of electromagnet
$\mathbf{B}$	Magnetic flux density
$\mathbf{B_c}$	Magnetic flux density contributed by the conductor
$\mathbf{B_e}$	Magnetic flux density contributed by the EM
$\mathbf{B}_{\mathrm{s}}$	2D axial-symmetrical magnetic flux density generated by the eddy-current density from analytical solutions
$\mathbf{B}_{\mathrm{sc}}$	2D axial-symmetrical magnetic flux density generated by the conductor of the eddy-current density from analytical solutions

$\mathbf{B}_{se}$	2D axial-symmetrical magnetic flux density generated by the electromagnet of the eddy-current density from analytical solutions
$\mathbf{C}_{d}$	Diffusion coefficient (1)
$\mathbf{C}_{e}$	Time Derivative Diffusion coefficient (s)
$\mathbf{C}_{\alpha}$	Conservative flux convection coefficient (1/m)
$\mathbf{C}_{\beta}$	Conservative coefficient (1/m)
$\mathbf{E}$	Electric field intensity
$\mathbf{H}$	Magnetic field intensity
$\mathbf{H}_{we}$	Homogeneous transformation from world coordinate to an EM coordinate
$\mathbf{I}_{a}$	Input array of the artificial neural network
$\mathbf{J}$	Total induced Eddy-currents
$\mathbf{J}_{C}$	Induced Eddy-currents contributed by the conductor elements
$\mathbf{J}_{E}$	Induced Eddy-currents contributed by the EM
$\mathbf{J}_{Re}$	Real part Eddy-current densities
$\mathbf{J}_{Im}$	Imagine part Eddy-current densities
$\mathbf{J}_{xRe}$, $\mathbf{J}_{yRe}$, $\mathbf{J}_{zRe}$	x, y, z component of the real part Eddy-current densities
$\mathbf{J}_{xIm}$, $\mathbf{J}_{yIm}$, $\mathbf{J}_{zIm}$	x, y, z component of the imaginary part Eddy-current densities
$\mathbf{O}_{a}$	Output array of the artificial neural network
$\mathbf{P}_{E}$	Point in the EM coordinate
$\mathbf{P}_{w}$	Point in the world coordinate
$\mathbf{R}_{we}$	Rotation matrix from world coordinate to an EM coordinate
$\mathbf{T}_{we}$	Translation matrix from world coordinate to an EM coordinate
$[\mathbf{A}_{C}]$	Magnetic vector potential contributed by the conductor elements
$[\mathbf{A}_{E\ell}]$	ℓ component magnetic vector potential contributed by the EM

$[\mathbf{Q}]$	Constraint matrix
$[\mathbf{Q_B}]$	Constraint matrix for boundary condition
$[\mathbf{Q}_{\mathbf{B}n}]$	Constraint matrix for tangential direction boundary condition
$[\mathbf{Q}_{\mathbf{B}t}]$	Constraint matrix for normal direction boundary condition
$[\mathbf{Q_C}]$	Constraint matrix for conservation law

Lower Case Symbols

a	Half-length of EM
a_i	Inner radius of EM
a_o	Outer radius of EM
a_p	Input current parameter of EM
a_x, a_y	x, y direction input amplitudes
d	The distance between the plate and sensor
d_h	Hole diameter
d_w	Diameter of wire
f	Input current frequency
h	Thickness of the plate
h_e	Element thickness
h_p	Plate thickness
k_a	Number of node for the output layer of ANN
m_a	Number of time instance for ANN
n_a	Number of sensor for ANN
n_s	Number of source

n_v	Number of volume element
p	Vertex of element
r	Element position in r direction
$s_{di,j}$	2D/3D: The length of i^{th} element, j^{th} line/the area of i^{th} element, j^{th} surface
r_{bi}	Boundary radius
r_e	Element length in r direction
$s_{i\ell\pm}$	The i^{th} element $\ell \pm$ surface, $\ell: x, y, z$
v	Volume of element
v_{di}	2D/3D: The area/volume of i^{th} element
v_i	3D: The volume of i^{th} element, 2D: the area of i^{th} element
w_p	Non-ferrous metal plate width
w_x, w_y	x, y direction plate width
x_i, y_i, z_i	Position of i^{th} element
x_s, y_s	Position in the global stimulating plane
x_u, y_u	Position in the EM local coordinate
z	Element position in z direction
z_p	The distance between the plate and sensor
$\mathbf{e}_x$, $\mathbf{e}_y$	Unit vector along the x, y directions
$\mathbf{e}_\theta$	Unit vector along the tangential direction
$\mathbf{n}_{i\ell\pm}$	The i^{th} element $\ell \pm$ normal vector, $\ell: x, y, z$
$\boldsymbol{n}_{i,j}$	The normal vector of i^{th} element j^{th} surface
$\mathbf{p}_{r,pw}$	A point **p** in the word coordinate for homogeneous transformation
$\mathbf{p}_{r,pe}$	A point **p** in the EM coordinate for homogeneous transformation
$\mathbf{r}_j$	Position of the j^{th} element of the plate

$\mathbf{t}_{i\ell\pm}$	The i^{th} element $\ell\pm$ tangential vector, $\ell: x, y, z$

Greek

ρ_i	Ratio of inner radius to outer radius
ρ_a	Ratio of half-length to outer radius
μ_0	Magnetic permeability of free space (=4×10^{-7}(H·m^{-1}))
γ_{cij}	The modified kernel function to calculate the j_{th} element conductor magnetic vector potential contributed by the unit current density of the i^{th} element conductor
σ	Electrical conductivity
ω	Angular frequency of the current
δ	Skin depth
Δ	Ratio of skin depth to outer of the outer radius of the EM
ε_0	Permittivity of vacuum (=8.854×10^{-12}(F·m^{-1}))
ε_r	Relative permittivity
ε_{r_R}	Real part relative permittivity
ε_{r_I}	Imagine part relative permittivity
$s_{i,j}$	3D: the area of i^{th} element, j^{th} surface, 2D: the length of i^{th} element, j^{th} line
ϕ	Physical field value
θ_r	Rotation angle in the homogeneous transformation
$\boldsymbol{\alpha}_{de(i)}$	i^{th} row of state matrix [$\boldsymbol{\alpha}_d$] accounting for i^{th} element
$\boldsymbol{\alpha}_{ds(i,j)}$	j^{th} surface of $\boldsymbol{\alpha}_{de(i)}$

$\boldsymbol{\beta}_{de(i)}$	i^{th} row of state matrix [$\boldsymbol{\beta}_d$] accounting for i^{th} element
$\boldsymbol{\beta}_{ds(i,j)}$	j^{th} surface of $\boldsymbol{\beta}_{de(i)}$
$\boldsymbol{\gamma}_{\mathbf{E}}$	The magnetic vector potential contributed by the unit current EM divided by the magnetic permeability of free space
$\boldsymbol{\eta}_{cr}$, $\boldsymbol{\eta}_{cz}$	r and z component of magnetic flux density contributed by the conductor of the unit current density
$\boldsymbol{\eta}_{er}$, $\boldsymbol{\eta}_{ez}$	r and z component of magnetic flux density contributed by the EM of the unit current density
$\boldsymbol{\eta}_{E}$	The magnetic flux density contributed by the EM of unit input current
υ	Half of distance between two EM
$\boldsymbol{\lambda}_{vi}$	Unit vector to map the corresponding i^{th} volume element
$\boldsymbol{\lambda}_{sk}$	Unit vector to map the corresponding s^{th} source element
$\boldsymbol{\varphi}_{E}$	Magnetic vector potential of a single point generated from the EM
$\boldsymbol{\varphi}_{C}$	Magnetic vector potential of a single point generated from the conductors
$\boldsymbol{\Lambda}_{\mathbf{d}}$	Difference vector of neighboring elements
$\boldsymbol{\Lambda}_{\mathbf{b}}$	Difference vector of boundary elements
[$\boldsymbol{\alpha}_d$] , [$\boldsymbol{\alpha}_e$]	State matrix of distributed parameter element method
[$\boldsymbol{\beta}_d$], [$\boldsymbol{\beta}_e$]	Input matrix of distributed parameter element method
[$\boldsymbol{\alpha}_f$]	State matrix of first order eddy-current field
[$\boldsymbol{\beta}_f$]	Input matrix of first order eddy-current field
[$\boldsymbol{\alpha}_s$]	State matrix of second order eddy-current field
[$\boldsymbol{\beta}_s$]	Input matrix of second order eddy-current field

Abbreviations

2D	two dimensional
3D	three dimensional
ANN	artificial neural network
CDF	cumulative distribution function
DCS	distributed current source
DPE	distributed parameter element
ECD	eddy-current density
EM	electromagnet
FEA	finite element analysis
MFD	magnetic flux density
NDT	non-destructive testing
PDF	probability density function
TMS	transcranial magnetic stimulation

SUMMARY

Motivated by two applications (retinal prosthesis and nondestructive damage detection), this research develops a new actuating method utilizing magnetic and electric fields as media to enable manipulation of a relatively high-resolution magnetic or electric patterns with a relatively small number of electromagnets or electrodes based on the distributed parameter element method. Unlike traditional methods where discrete points are stimulated, the synthetized magnetic or electric fields are accurately controlled between adjacent electromagnets or electrodes. Two parts are needed for design analysis of this mechanism: Magnetic and electric field modeling and transduce optical color images to magnetic/eddy patterns.

Most physical fields can be represented by the linear partial differential equations (PDEs). Each point of the physical fields obeys the continuity equation and boundary condition. A distributed parameter element method to model the physical fields is proposed. The distributed parameter element method divides the irregular shape physical fields into distributed elements and formulate the physical field value of each element in state-space representation. The divergence theorem is applied that the continuity equation at each discrete element can be extended to the conservation law for considering the irregular shape of each element. However, the governing equation of eddy-current induced magnetic field exists the curl operator and cross product terms and make the calculation complicated. Therefore, another kind of the distributed parameter element method, the distributed current source, which considers each element of the conductor is a current source for mutual inductance, is utilized to calculate the magnetic/eddy-current fields

induced in non-ferrous metal and biological tissue to avoid the complicated calculations of the curl operator and cross product.

Electromagnet (EM) arrays have been widely used in many applications ranging from electric motors to haptic devices in medical robotics. This paper is motivated by two applications: The first, potentially an emerging neuro-medical application, is to develop prosthetic eyes with contactless stimulation that corresponds to high-resolution optical image on retina with a small number of electrodes. The second responds to a practical need of nondestructive testing (DNT) for a relative large area without moving sensors. A common problem in these applications involves high-resolution control of magnetic/eddy-current (M/EC) continuous fields on an electrically conductive surface using an EM array. A method utilizing an EM array to transduce optical color images to magnetic and eddy-current patterns based on the concept of continuous-field motion control is introduced. This magnetic field scanning method by using an EM array can be extended to the electric field scanning by the electrode array. The distributed parameter element method and the magnetic and electrical field scanning method are numerally verified and experimentally demonstrated for the artificial perception and nondestructive damage detection applications, which include design analysis of the retinal prosthesis of magnetic simulation by using a micro electromagnet array, electrode placement for electrical muscle stimulation, and edge and hole detections for the eddy-current sensing system.

CHAPTER 1. INTRODUCTION

1.1 Motivation

A general modeling method, referred to here as a distributed parameter element (DPE) method is developed to model the physical field for two applications involving magnetics, electric and eddy currents fields. In 1997, the US Census Bureau reported that about 8 million individuals over the age of 15 had difficulty seeing and of those, 1.8 million were unable to read. Some photoreceptor degeneration diseases, such as retinitis pigmentosa (RP) and age-related macular degeneration (AMD), affect only rods and cones, leaving intact remaining layers. If ganglion cells preserve their functionalities, some artificial stimulation of nervous cells may recover vision [1]. One method is epiretianl implant, which implants the electrode near the ganglion cells and some research successfully make the subjects feel the lights. But, the drawback of the implanted electrodes is that with relatively low-density retinal implants, simple visual tasks with the blind subject's natural light perception vision are impossible to be accomplished [2]. G. Bonmassar etc. at Harvard medical school demonstrated that a single sub-millimeter coil can activate neuronal tissue [3]. They recorded from rabbit retinal ganglion cells while stimulating with the small coils and found that μMS does induce neural activity. This result raises the possibility of the magnetic simulation for retinal prosthesis by micro coils.

In non-destructive damage detection application, as a non-contact sensing device capable of measuring various properties of the non-ferrous metal objects both statically and dynamically, eddy-current (EC) sensors are widely used in many applications due to their fast response, high sensitivity and harsh-environment workability. High-precision

magnetic sensors with advantages of small size, fast response and low power consumption, which can fulfill measurement requirements at both high and low frequencies while ensuring compact structure integrity of the EC sensor, are now widely available at low cost. However, the potentials of EC sensors for manufacturing applications are underexploited because the relationships between the geometrical/material parameters and the measured magnetic fields are highly coupled and spatially nonlinear. For the above two applications, an efficient, intuitive physical field modelling method for design analysis of these devices is needed.

1.2 Prior and Related Works

The following review of the prior and related work is organized in three parts. The first part reviews the method to solve PDE particularly for the electric field and eddy-current fields. Next, some retinal prosthesis methods are investigated. The last part summarizes some applications using eddy-current devices.

1.2.1 PDE and Eddy-Current Modelling Methods

Physical fields can be formulated as PDEs. The dynamic behaviors of the fields can be investigated by solving the PDEs. The methods to solve PDEs can be classified into two categories; analytical solutions and numerical solutions. There are some classical methods of the analytical solutions such as the separation of variables and the method of characteristics. Analytical solutions generally assume idealized shapes and boundary conditions. For the computation of complicated geometric physical fields, numerical solutions are often needed. Three most widely used numerical methods to solve PDEs are the finite element method (FEM), finite difference methods (FDM), and finite volume

method (FVM). FEM uses variationl methods from the calculus of variations to approximate a solution by minimizing an associated error function. FDM uses finite difference equations to approximate derivatives, such as the heat transfer problem. In FVM, the divergence term is converted to surface integrals using the divergence theorem. FVM is formulated to allow for unstructured meshes and often used in computational fluid dynamics. Compared among these three methods, FEM is more mathematically involved but less physically significance. FDM and FVM require far more efforts for irregular geometries. Besides, a discrete modeling method, referred as a flexible space division algorithm (FSDA), is proposed for design and real-time applications of mechatronic and manufacturing systems [4]. The thermal fields can be modeled in state-space for objects with regular shapes such as cubic or cylinder.

For modeling eddy-current, Dodd *et al.* [5] derived an analytical model to calculate the eddy current induced by a cylindrical coil in a plane. Jeng [6] numerically calculated the eddy current distribution of a 2D axisymmetric conducting slab with a flaw by separating the conductor to many rings. Theodoros *et al.* [7][8] proposed a truncated region eigenfunction expansion method to replace integral expressions for the axisymmetric electromagnetic field and impedance of the eddy current coil [7][8]. In general, axisymmetric solutions assume idealized shapes to derivate simplified solutions. Driven by the needs to simulate the induced eddy currents in biological tissues, the impedance method (IM) which subdivides the object into a number of cells was developed for transcranial magnetic stimulation (TMS); each cell is replaced by an equivalent impedance for calculating the power deposition by the eddy currents. This method was later extended to the independent impedance method (IIM) [9][10] to improve the conditionality and

speed up the numerical convergences. The IM and IIM methods [11][12] account for the boundary effects but neglect mutual inductances because of the low electrical conductivity of the biological tissues. The analyses of EC devices often involve complex geometry in a 3D space, which are solved numerically.

Besides these methods, a distributed multiple model (DMP) method was proposed to characterize the MFD fields of a permanent-magnet (PM) or electromagnet (EM) for design/control of PM actuators/sensors [13][14], and its extension equivalent-PM [15]. More recently, a similar but more general approach, referred to here as a distributed current source (DCS) method, was developed in [16], which derives closed-form solutions to model the magnetic/electric fields of an EM component for the design of electromagnetic actuators using layout optimization [17]. Unlike FEM that requires a sufficiently large air space to enclose all the magnetic fields of both the EM and the EC to ensure its solution accuracy, the DCS method uses point sources to eliminate the need to include air space.

1.2.2 Retinal Prosthesis

Photoreceptor degeneration diseases, such as retinitis pigmentosa (RP) and age-related macular degeneration (AMD), affect only rods and cones, leaving intact remaining layers. If ganglion cells preserve their functionalities, some artificial stimulation of nervous cells may recover vision. Depending on the location of stimulating electrodes, visual prosthesis can be divided to three groups; retinal, optic nerve, and visual cortex stimulation devices [1]. Retinal prosthesis has the potential to provide increased vision to some subjects who are blind from retina degeneration, such as retinitis pigmentosa (RP) and age-related macular degeneration (AMD). Retinal prosthesis can be classified to epiretinal and

subretinal stimulations and extraocular devices for transcretinal stimulation. Epiretinal approaches place electrodes on the top side of the retina near ganglion cells for direct stimulation [18]-[20]. Subretinal approaches [21][22] place electrodes and most of the electronics underneath the retina in the location of the degenerated photoreceptors between the retinal pigment epithelium. Some research implants the photodiodes under the retina to generate currents that stimulate the retina. In the extraocular approach, electrodes are placed on the posterior scleral surface of the eye. Between 2002 and 2004, Argus^{TM} 16 device, which consists of 16 disc-shaped platinum electrodes, is implanted on six blind subjects and has enabled blind subjects to detect when lights are on or off, describes an object's motion, counts distinct item, as well as locates and distinguishes different basic objects in the environment [18], [23]. In early 2007, The Argus^{TM} II device, which has a thin-film array of 60 platinum electrodes that are attached to the epiretinal surface, received the FDA approval to conduct a clinical study. Another epiretinal implant device is Intelligent Medical Implants (IMI) AG [24] where involves a thin-film polyimide array of 49 platinum electrodes. The subjects were able to distinguish between different points and recognized simple patterns such as horizontal bars [25].

For the amplitudes of stimulating currents, the stimulating thresholds are measured in vitro on the Rabbit retinas [26]. The threshold current densities for 125- and 500-μm diameter electrodes short latency response (3-5 ms) are 32.6 A/m^2 and 10.186 A/m^2. The electrodes do not need to place exactly at the body for the stimulation. But, the threshold increases when the distance between the cell body of retinal ganglion cell and electrode increases. Magnetic stimulation of neural tissue is an intriguing technology because stimulation may be affected without direct contact to the tissue. Some research

discusses to use magnetic stimulation on the neural excitation [27][28]. Some approaches model the response of an axon to extracellular stimulation by a point current source [29]-[31], and magnetic stimulation [32]. G. Bonmassar etc. at Harvard medical school demonstrated that a single sub-millimeter coil can activate neuronal tissue [3]. They recorded from rabbit retinal ganglion cells while stimulating with the small coils and found that μTMS does induce neural activity. This result raises the possibility for the nervous tissue stimulation of micro coils. However, this experiment is designed for a single point magnetic stimulation by a single coil. A 2D plane magnetic stimulation for the retina ganglion cells by an EM array has still not been mentioned.

1.2.3 Eddy-Current Device Applications

Eddy-current (EC) devices have been widely used, ranging from biomedical to manufacturing applications. In biomedical applications, TMS induces EC in the neural stimulations [33]-[37]. In manufacturing, electromagnetic force generated by the electromagnets (EMs) can be utilized for vibration suppression of a beam [38]-[42]. Electromagnetic induction heating has been developed to achieve a rapid mold surface heating [43]-[47]. EC testing is one of the most extensively used non-destructive techniques for inspecting electrically conductive materials at high speed [48]. EC displacement sensor is a common device to measure the position and movement of objects [49][50]. Commonly, three kinds of magnetic sensor are utilized for measurement of eddy-current fields: inductive pick-up coil, AMR, and GMR sensors [51]. Pick-up coils have good linearity but show decreasing sensitivity at lower frequencies. Compared with GMR sensors [52][53], the magnetic field limited resolution of AMR sensors is higher than GMR

sensors. Commercial eddy-current sensors employ a single sinusoidal excitation for the measurement of the displacement between the sensor and conductor workpiece. In [54]-[56], the electrical conductivity of a metal plate is measured by the sensing coils with the broadband frequency input currents. As an effective media for energy conversion among magnetic, electric and mechanical force/displacement fields, EM arrays can be widely found in many applications ranging from industrial sensor/actuator systems, to data storage devices, to robotic human-machine interfaces, and more recently to emerging biomedical mechatronics.

There are broad applications of an EM array, which can be divided to two groups depending on the control media. The *first* group controls the magnetic field and hence renders the magnetic force for applications such as haptics devices ([57]-[60]) and user interfaces [61][62]. For examples, graphical tactile displays use a micro coils array to vibrate the flexible membranes for visually-impaired people [59]; EM arrays were used in a variety of haptic devices; a pin-array that renders forces in [58]; and near-surface haptic feedback on tabletops in [61]. Besides planar EM arrays, EM arrays are also used in spherical motors [64] and micro-manipulation of a micro robot [65][66]. The *second* group controls the induced eddy-current field in the conductor. In biomedical applications, coil arrays are used for TMS for nerve cells [67][68]. In DNT applications, eddy-currents are commonly used to detect surface or sub-surface defects. An EM array that generates an eddy-current pattern providing much richer and more comprehensive data sets than traditional methods using single eddy-current sensor scan [69], is widely accepted as a preferred NDT technique for flaw reconstruction. In [70], a 16 × 16 flat coil-array was used to inspect a surface without the need for mechanical scanning.

1.3 Problem Descriptions and Objectives

This thesis aims at developing a new actuating method utilizing electric and/or magnetic fields as a media to create a relatively high-resolution electric/magnetic pattern with a relatively small number of electromagnets for artificial perception and manufacturing applications. Figure 1-1 shows the two applications using conventional discrete point manipulation; visual assistant methods for blind people and non-destructive testing (NDT) damage detection of machined surface.

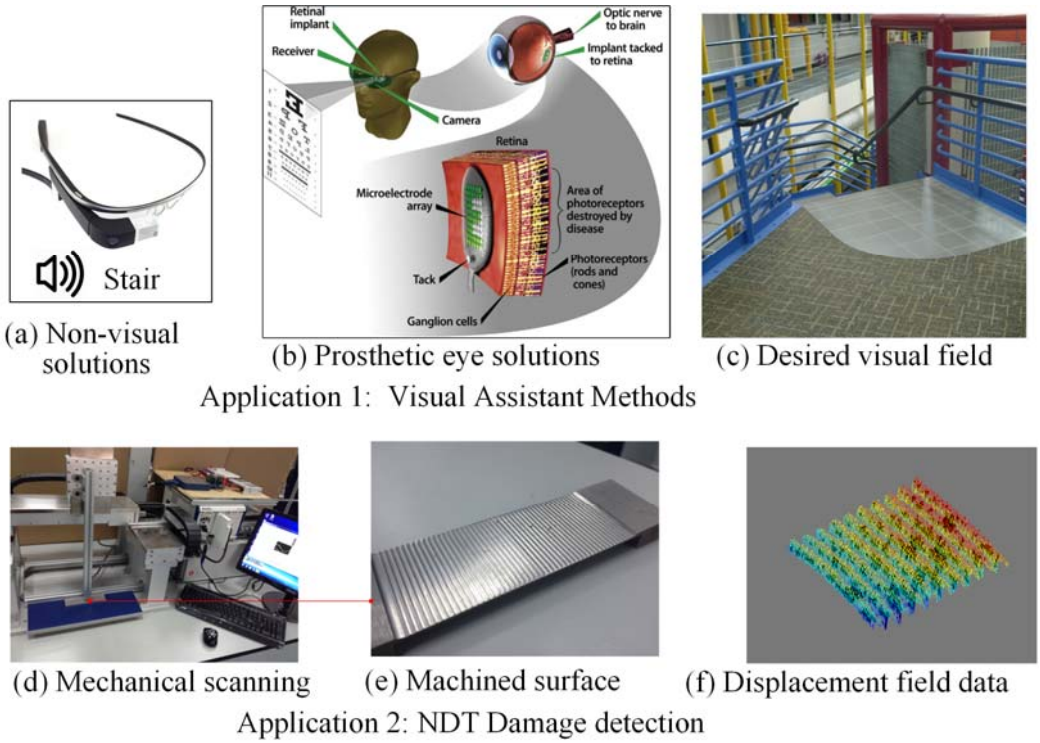

Figure 1-1 Applications with discrete manipulation

Figs 1-1(a) and 1-1(b) compare two methods (nonvisual and prosthetic eye) typically with a digital camera for *Application 1*, typically with a digital camera to help blind people perceive their environment. Given a digitally captured optical image, non-

visual methods convert it into other human sensible signals (such as audio or tactile), whereas prosthetic eye solutions use an array of microelectrodes to electrically stimulate the retinal ganglion cells to create visual information. As each stimulated point requires a dedicated electrode, existing prosthetic eyes have very limited resolution. In dangerous environment such as stepping down a stair (Fig. 1-1(c)), both existing nonvisual and low-resolution prosthetic eyes solutions are inadequate. Fig. 1-1(d) illustrates an example NDT process for *Application 2*, where a laser beam is moved mechanically while scanning the machined surface profile to detect potential damages. In contrast to human perception of the machined surface (Fig.1-1(e)), machine relies on signals digitally measured from the reflected beam (Fig. 1-1(f)) to derive a decision in Application 2. As mechanical scanning is often costly and time-consuming, it is desired that surface can be inspected without mechanical scanning. For the above reasons, this thesis develops a new concept of utilizing magnetic and electric fields to induce and manipulate relatively high-resolution eddy-current patterns on an electrically conductive surface in Fig. 1-2.

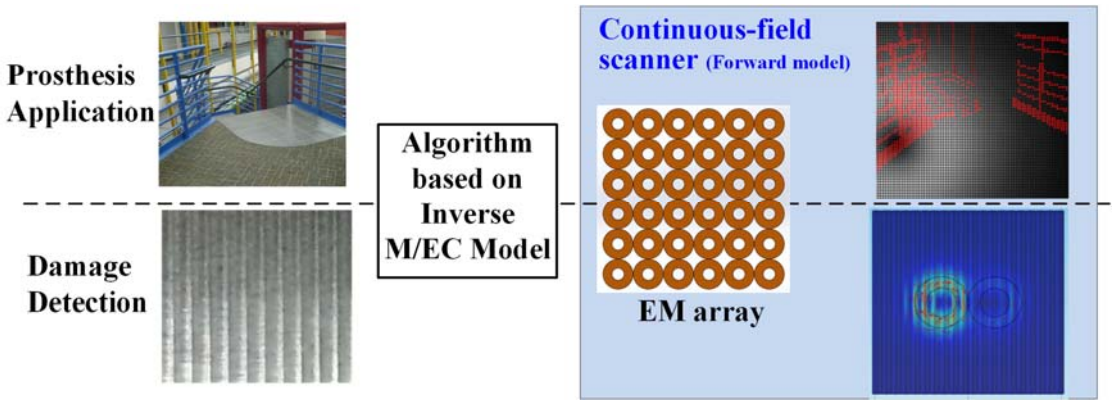

Figure 1-2 High-resolution eddy-current patterns

As in a conventional design, essential information is extracted from light-based images captured from the CCD camera. However, the proposed method transduces these light-based images into continuous eddy-current patterns using the EM-array to stimulate the retinal ganglion cells. In the design for prosthetic eye applications, an array of miniature coils is designed to be placed close to the macular that is the main region (approximately 5 mm diameter in size) for the with healthy to sense the converted light-to-electric signals. Such techniques where the EC pattern can be generated on the workpiece by an EM array can be used in damage detection applications to detect defects by means of magnetic sensors which continuously monitor and compare measured patterns against a pre-determined patterns. To achieve this design goal, the synthesized M/EC fields must be accurately controlled by an array consisting of a relatively small number of EMs without mechanical moving parts. Technical challenges include that the spatially nonlinear properties of the magnetic flux density generated by an EM, the (geometrical and material) effects of the magnetic and electric fields on the retina, and the methods to investigate the effects numerically and experimentally. Three tasks were completed to overcome these problems; a continuous field-manipulation method, a numerical method based on distributed parameter element (DPE), and an in-depth analysis using DPE-simulations to investigate the effects of continuous field-manipulation on the two applications that have motivated this thesis:

(1) In the first task, a continuous-field actuation method that utilizes the magnetic field as a media for transducing an optical color image to the magnetic/eddy-current pattern has been developed. To reduce the mathematic models for

design analysis into a trackable form, Gaussian approximations are utilized to characterize the MFD fields.

(2) In the second task, a DPE method based on a vector or a scalar potential for the modeling the magnetic and electric fields has been developed, which provides a basis for subsequent stationary, time dependent, and harmonic analysis of the physical field. The two- or three-dimensional irregular shaped physical (magnetic and electric) fields have been formulated in state-space representation with the application of the divergence theorem to satisfy the conservation law and to account for the boundary conditions on each element.

(3) The continuous-field actuation method developed in the first task and the DPE method in the second task provide the basis to investigate the effects of transducing the optical color image to magnetic/eddy-current field patterns on biological tissues and for NDT of non-ferrous metallic objects in Task 3. As an intermediate step, the concept feasibility of the continuous-field actuation method was experimentally demonstrated on a human-arm muscle.

1.4 Thesis Outline

The remainder of this dissertation is organized as follows.

Chapter 2 presents a method utilizing an EM array to transduce optical color images to magnetic and eddy-current patterns based on the concept of continuous-field motion control for MFD peak or ECD center. Both the forward and inverse models are formulated. the former solves for the continuous-fields generated by the EM array with the analytical

solution whereas the latter determines the input currents to the EM array for a given optical image.

Chapter 3 presents a new method, called the DPE method to model the two or three dimensional irregular shape magnetic and electric field in state-space representation by applying the divergence theorem on each element to satisfy the conservation law and boundary conditions to account for the geometry, which provides a basis for the subsequent stationary, time dependent, and harmonic analysis. The DPE method improves the geometry limitation of the analytical solution for the physical field formulation.

Chapter 4 illustrates the applications of artificial perceptions based on the DPE-based magnetic/electric scanning method. Three examples (μ-EM array magnetic stimulation, μ-electrode array electrical stimulation, a multiple layer retinal structure electrical stimulation) are illustrated for design analysis of the artificial perception. In addition, a numerical illustration of the non-mechanical ECD scanning method along with the artificial neural network (ANN) for edge and hole detections is presented.

Chapter 5 experimentally evaluates the method of the spatial accuracy of 1D and 2D peak-MFD scanning and 2D center-ECD of a non-ferrous plate by measuring the MFD in space with the magnetic sensor and an intermediate setup of using the muscle electrical stimulation by an electrode array for alternative perception. The DPE method is verified by the frequency response and boundary effects of hole and edge detections on the non-ferrous metal plate by the means of the eddy-current sensing.

CHAPTER 2. ALTERNATIVE PERCEPTION

This chapter presents a continuous-field actuation method by using the magnetic and electric fields as a media to transduce optical color images to magnetic/eddy-current patterns for alternative perception. First, a method utilizing an EM array to transduce optical color images to magnetic and eddy-current patterns based on the concept of continuous-field motion control for MFD peak or ECD center is introduced. Both the forward and inverse models are formulated; the former solves for the continuous-fields generated by the EM array with the analytical solution whereas the latter determines the input currents to the EM array for a given optical image. Unlike the forward model for off-line analyses, the algorithm for the inverse model must be computed in real-time. The method will be illustrated numerically in the context of an emerging prosthetic-eye application that potentially can be used to help blind people perceive their environment. The spatial accuracy of 1D and 2D peak-MFD scanning was investigated experimentally. Second, the theory for generating the synthetized MFD that has the Gaussian function properties and three design criteria evaluating its performance as well as the magnetic scanning algorithm for implementing it on the 2D EM-array are detailed.

2.1 Algorithm for Converting an Optical Color Image to Magnetic/Eddy-Current Patterns

As illustrated in Fig. 1-1, the algorithm for transducing an optical color image transduced to an electric/magnetic pattern begins with feature images where essential information is extracted from light-based color images captured typically by a wearable

digital camera. In this work, the image is described in device-independent Lab model where the brightness L_l-axis increases from the bottom to the top of the 3-axis model; the a-b are color-opponent dimensions with L_a-axis extending from green ($-L_a$) to red ($+L_a$), and b-axis from blue ($-L_b$) to yellow ($+L_b$). The color clusters in a-b domains are analyzed using the k-means clustering algorithm for color-based image segmentation. The resulting color-clustered image is then filtered to remove fragments that have a blob size smaller than a specified threshold (0.1% of the $N_{fx} \times N_{fy}$ image). Small connected components of objects with pixel size are smaller than the threshold value are merged to the background. The four steps involved in the algorithm are summarized as follows:

Step 1: Transfer pixels from RGB to Lab color system.

Step 2: Apply k-means clustering on data in L_a-L_b domain.

Step 3: Assign pixels of the largest cluster to the background. Other clusters represent different objects. The maximum clustering points are considered as the background and will not be scanning for the next step.

Step 4: Perform connected-component labeling on objects and filter out small size segments.

Fig. 2-1 illustrates the three clusters in the L_a-L_b domain and the result after performing k-means clustering and blob size-filtering on the “stair” image

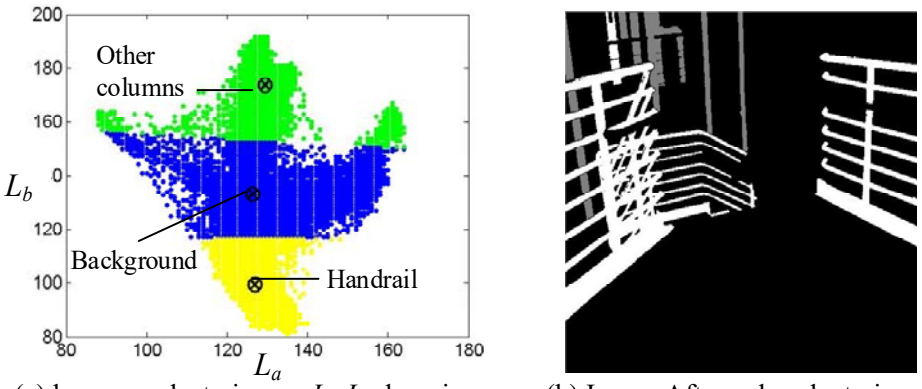

(a) k-means clustering on L_a-L_b domains

(b) Image After color clustering and blob filtering

Figure 2-1 Color-based clustering results

2.1.1 EM Input Currents Manipulation

Once the k-level feature image is obtained, the (N_{fx}×N_{fy}) image pixels of the labeled image are matched onto the (N_{sx}×N_{sy}) points (k-level amplitude) of the stimulating plane (w_x×w_y) through the (N_{ex}×N_{ey}) EM array as illustrated in Fig. 2-1:

$$\frac{N_{fx}}{N_{fy}} = \frac{N_{ex}}{N_{ey}} = \frac{N_{sx}}{N_{sy}} = \frac{w_x}{w_y}$$

As seen in Fig. 2-2(c, d), the basic unit is a 2×2 EM unit with local normalized coordinates (a_x, a_y). The scanning strategy is to turn on a 2×2 EM unit at any time instant and control its peak M/EC within the region bounded by the four EM centers. Thus, the inverse model can then be reduced to calculate the input currents to the 4 EMs for a specified peak-MFD position. To facilitate the design, the z-component MFD distribution $B_z(x_c, y_c)$ of a plane perpendicular to a cylindrical air-cored EM coil with unit input current is modeled as a modified Gaussian-like function in the normalized form Eq. (2.1), where (x_c, y_c) are the local coordinates with its origin at the EM coil center:

$$\frac{B_z(x_c, y_c)}{B_o} = \exp\left[-\frac{x_c^2 + y_c^2}{2\sigma_m^2}\right] \quad \text{where } \sigma_m > 1 \tag{2.1}$$

In Eq. (2.1), B_o and σ_m describe the peak value and shape of the MFD distribution of an EM respectively. The position of the peak MFD value can be controlled to move linearly on the stimulating plane based on a push-pull operational principle given by (2.2) where A_{ci} (with i=1,..,4) is the relative current amplitude (dimensionless) of the i^{th} EMs and υ is the half spacing between two adjacent coils in x or y direction defined in Fig. 2-2(d):

$$A_{ci}(a_{xi}, a_{yi}) = \frac{(1-a_{xi})(1-a_{yi})}{\bar{B}(a_x, a_y; \sigma_c, \upsilon)} \tag{2.2a}$$

$$\text{where } \begin{pmatrix} a_{xi} & a_{yi} \end{pmatrix} = \begin{cases} \begin{pmatrix} a_x & -a_y \end{pmatrix} & i \text{ is an odd number} \\ \begin{pmatrix} -a_x & a_y \end{pmatrix} & i \text{ is an even number} \end{cases} \tag{2.2b}$$

$$a_x = \frac{x_u}{\upsilon} - 1; \; a_y = \frac{y_u}{\upsilon} - 1; \tag{2.2c, d}$$

$$\bar{B}(a_x, a_y; \sigma_c, \upsilon) = \sum_{i=1}^{4} (1-a_{xi})(1-a_{yi}) \exp\left[-\frac{(a_x - \bar{\upsilon}_{xi})^2 + (a_y - \bar{\upsilon}_{yi})^2}{2(\sigma_c / \upsilon)^2}\right] \tag{2.2e}$$

$$\text{and } \left(-\bar{\upsilon}_{x1} = -\bar{\upsilon}_{y1}\right) = \left(\bar{\upsilon}_{x2} = -\bar{\upsilon}_{y2}\right) = \left(-\bar{\upsilon}_{x3} = \bar{\upsilon}_{y3}\right) = \left(\bar{\upsilon}_{x4} = \bar{\upsilon}_{y4}\right) = 1$$

In Eq. (2.2a), $\bar{B}$ is introduced to maintain a constant peak MFD value B_o for compensating the variation in MFD due to the push-pull operation. Eq. (2.2c), (2.2d) provide the linear mapping between (x_u, y_u) and (a_x, a_y) defined in Fig. 2-2(d).

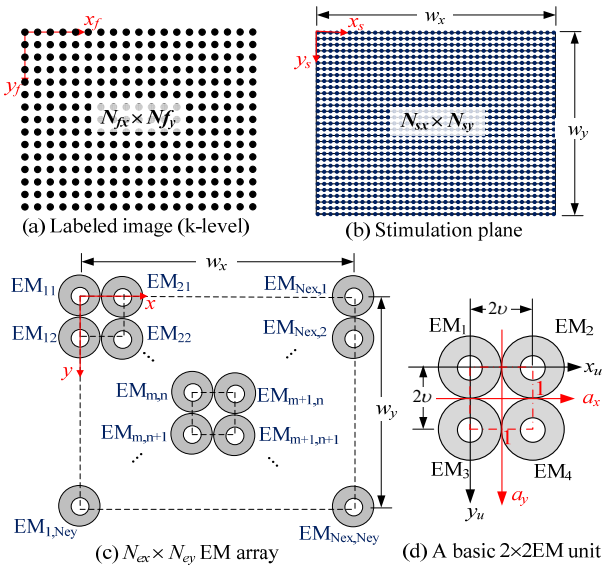

Figure 2-2 Relationship between image and scanner

Equations Eq. (2.2a)~(2.2e) provides the function A_{ci} to determine the input currents to control the peak MFD (with value equal to B_0) at a desired position within the operating range of a 2×2 EM unit. The last part of the algorithm must sequentially determine a 2×2 EM unit and its appropriate four input currents to faithfully execute the overall scanning path in terms of stimulating points. The algorithm involves the following three steps:

Step a: Determine the 2×2 EM unit ($EM_{m,n}$, $EM_{m+1,n}$ $EM_{m,n+1}$ $EM_{m+1,n+1}$) and its specified peak-MFD position in (x_u, y_u) coordinates. This includes a coordinate transformation from the (x_s, y_s) coordinates of the stimulating plane in the range of $N_{ex}\times N_{ey}$ EM array to the local coordinates (x_u, y_u) of the 2×2 EM unit. To account for the edge effects,

$$\begin{bmatrix} m \\ n \\ x_u \\ y_u \end{bmatrix} = \begin{cases} \begin{bmatrix} Q_x+1 & Q_y+1 & R_x & R_y \end{bmatrix}^{\mathrm{T}} & \text{If } x_s \neq w_x \text{ and } y_s \neq w_y \\ \begin{bmatrix} Q_x & Q_y+1 & 2\upsilon & R_y \end{bmatrix}^{\mathrm{T}} & \text{If } x_s = w_x \text{ and } y_s \neq w_y \\ \begin{bmatrix} Q_x+1 & Q_y & R_x & 2\upsilon \end{bmatrix}^{\mathrm{T}} & \text{If } x_s \neq w_x \text{ and } y_s = w_y \end{cases} \tag{2.3}$$

where $Q_x = floor\left(x_s / 2\upsilon\right)$; $Q_y = floor\left(x_y / 2\upsilon\right)$;

and $\left(R_x, R_y\right) = \left(x_s, y_s\right) \bmod 2\upsilon$.

In Eq. (2.3), *floor*(*x*) is the largest integer not greater than *x;* and "*x* mod 2*υ*" (abbreviation of "*x* modulo 2*υ*) is the remainder of the Euclidean division of *x* by 2*υ*.

Step b: Calculate the (a_x, a_y) component currents for the 2×2 EM unit from the local position (x_u, y_u) using Eq. (2.2c, d).

Step c: Determine the input currents for the 2×2 EM unit ($EM_{m,n}$, $EM_{m+1,n}$ $EM_{m,n+1}$ $EM_{m+1,n+1}$). All other EM currents of the N_{ex}×N_{ey} EM array are zeros. The input currents are specified by the dimensionless amplitude $A_{ci}(a_x, a_y)$ from Eq. (2.2a) multiplied by a scaling factor a_i defined by Eq. (2.4) where B_i and E_i are the desired MFD and ECD amplitudes divided by the peak MFD B_0 or maximum ECD value E_0 generated by an EM with unit input current:

$$\mathbf{I}_u = \begin{bmatrix} I_{m,n} & I_{m+1,n} \\ I_{m,n+1} & I_{m+1,n+1} \end{bmatrix} = \begin{bmatrix} a_1 A_{c1} & a_2 A_{c2} \\ a_3 A_{c3} & a_4 A_{c4} \end{bmatrix} \tag{2.4}$$

where $a_i = \begin{cases} B_i / B_0 & \text{MFD, } \sigma_c = \sigma_m \\ \left(E_i / \mathrm{E}_0\right) \sin \omega t & \text{ECD, } \sigma_c = 2\sigma_m \end{cases}$

The reason to double σ_c in ECD scanning is because of the skin effect causing the ECD to spatially decay more linearly as compared to the MFD scanning with the same gap between the EM and the plane surface.

Step d: Map the k-cluster image ($N_{fx}\times N_{fy}$) to the stimulating plane ($N_{sx}\times N_{sy}$) by the EM array ($N_{ex}\times N_{ey}$) with maximum input current amplitude a_{max}. The background cluster-points of the image are labeled as 1 and transformed to an amplitude of 0 (as they are not be transduced during scanning) and other labels are given a non-zero L_j-level amplitude:

$$L_j = \frac{j_k - 1}{k - 1} a_{\max}, \;\; j_k = 1, 2, \; ..., \; k \tag{2.5}$$

With Eq. (2.5), the labeled pixels are mapped onto the stimulating plane using nearest neighbor interpolation to retain the k-levels. The N points with non-zero amplitude ($L_i \neq 0$) on the stimulating plane can be concatenated to an N-columns matrix $\mathbf{X_p}$ given in Eq. (2.6):

$$\mathbf{X_p} = \begin{bmatrix} x_{s1} & x_{s2} & \cdots & x_{sN} \\ y_{s1} & y_{s2} & \cdots & y_{sN} \\ L_1 & L_2 & \cdots & L_N \end{bmatrix} \tag{2.6}$$

Step e: The scanning currents of the $N_{ex}\times N_{ey}$ EMs can be expressed as a matrix $\mathbf{I_E}$ in (2.7), where the subscripts (m, n) of I refer to the EMs, and the column number in bracket (i=1,…,N_i) refers to the non-zero stimulating points.

$$\mathbf{I_E} = \begin{bmatrix} I_{1,1}(1) & I_{1,1}(2) & \cdots & I_{1,1}(N) \\ I_{1,2}(1) & I_{1,2}(2) & & I_{1,2}(N) \\ \vdots & & \ddots & \vdots \\ I_{Nex,Ney}(1) & & \cdots & I_{Nex,Ney}(N) \end{bmatrix} \tag{2.7}$$

The procedures involved the algorithm for the inverse model, along with the geometrical parameters characterizing a 2×2 EM unit, is summarized in the flowchart (Fig. 2-3)

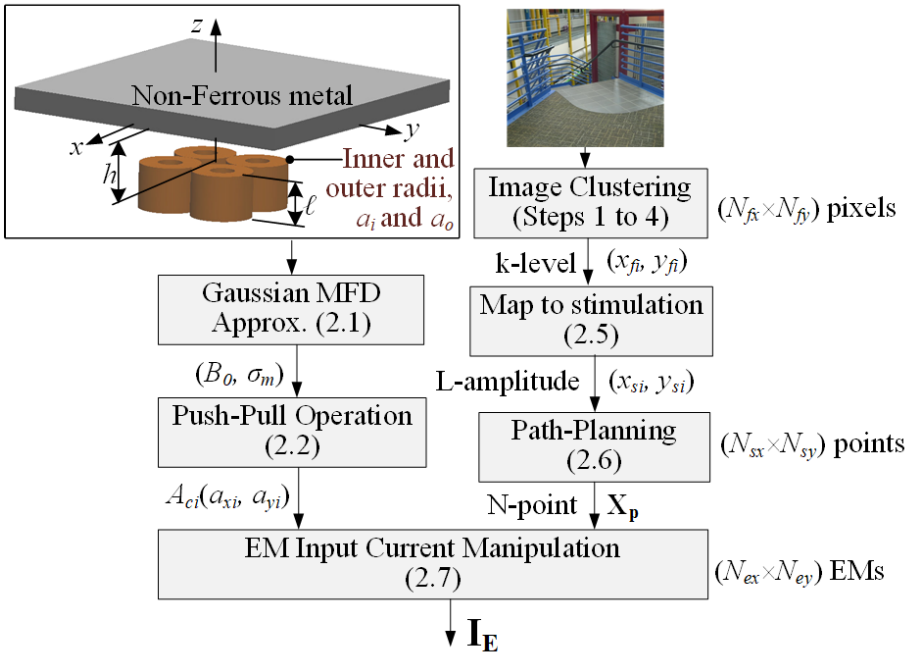

Figure 2-3 Flowchart illustrating the inverse model

The synthesized M/EC fields of the 2-by-2 EM array in three dimension can be determined by Eq. (2.8). $\mathbf{B_i}$, $\mathbf{E_i}$ are the M/EC fields in three dimension transferred from the M/EC fields in cylinder coordinate in Eq. (A.1), (A.2).

$$\mathbf{F_p}(\mathbf{x}) = \sum_{i=1}^{4} A_i \mathbf{F_{pi}}(\mathbf{x}; \upsilon_{xi}, \upsilon_{yi}) \tag{2.8}$$

$$\text{where } \mathbf{F_{pi}}(\mathbf{x}; \upsilon_{xi}, \upsilon_{yi}) = \begin{cases} \mathbf{B_i}(\mathbf{x}; \upsilon_{xi}, \upsilon_{yi}) & \text{MFD in free space} \\ \mathbf{E_i}(\mathbf{x}; \upsilon_{xi}, \upsilon_{yi}, \omega) & \text{ECD induced} \end{cases}$$

2.1.2 Numerical Illustration

Table 2-1 shows a conceptual retinal prosthesis, where a 6×6 micro-coil array is utilized to transduce images on a metal film sandwiched between macular and retinal cells. The "stair" image is used as an example in this illustration, which is transduced into MFD pattern in free space and an ECD pattern induced on a thin metal film by the coil array. Parametric values used in the simulation are shown in Table 2-1.

Simulation results are displayed in Fig. 2-4, where the k-level image (obtained after the sequential color-based clustering and blob size-filtering image segmentation processes) provides the input to the algorithm for the inverse model. Fig. 2-4(a) shows a partial image indicating k(=3)-level of labels which can be calculated from Eq. (2.5) (with a_{max}=1):

L_1 (black) = 0, background,

L_2 (gray) = 0.5, columns in the back, and

L_3 (white) =1, handrails.

Since the background points are ignored during scanning, only points with L_3 (white) and L_2 (gray) are transduced onto the stimulating plane as shown in Eq. (2.7), with respective field amplitudes (B_0, E_0) and (B_0/2, E_0/2) respectively for a (MFD or ECD) continuous-field scanning (line by line from left-to-right, up to down). The overall solutions to the inverse model, expressed as a matrix in Eq. (2.7), are plotted in Fig. 2.4(b) where the vertical and horizontal axes correspond to the row ($EM_{m,n}$) and column or the non-zero stimulating points (i=1,…,47015) of Eq. (2.7). The columns are implemented

sequentially in time domain; for each non-zero labeled point, only 4 of the 36 EMs (forming a 2×2 EM unit) calculated from Eq. (2.4) are excited.

Table 2-1 Parameters in Simulation (Geometry in mm)

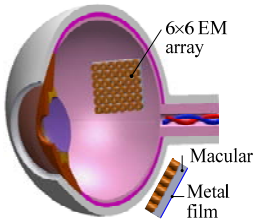	**6×6 micro-coil array** a_i=0.2, a_o=0.5, l= h=1 **Metal film** (aluminum); μ=4π×10^{-7} H/m, σ=3.774×10^7 S/m **Input current** ω=50k rad/s
B_0=26.69μT, σ_m=0.62mm E_0 =8.71A/mm^2.	**Image** N_{fx}=N_{fy}=501 pixels **Stimulating plane:** w_x=w_y=5mm, N_{sx}=N_{sy}=501 points

To help gain intuitive insights into the inverse and forward models, a handrail point located at (x=0.5mm and y=3.5mm) in the stimulating plane is used in the following discussion. Denoted as A in Fig. 2-4(a) and Fig. 2-4(b), point A is transduced at 44221th time instant and because it is at the center of the 2×2 EM unit (formed by $EM_{1,4}$, $EM_{1,5}$, $EM_{2,4}$, and $EM_{2,5}$) , the currents of EMs have the same values as shown in Fig. 2-4(a); I_m=0.294 and I_e=0.26sin(50kt), with unit Amperes, for MFD and ECD scanning respectively. As validated in Fig. 2-4(b), the four input currents correspond to the four interceptions made by the four ($EM_{1,4}$, $EM_{1,5}$, $EM_{2,4}$, $EM_{2,5}$) horizontal dash lines and the vertical (44221th) dashed line.

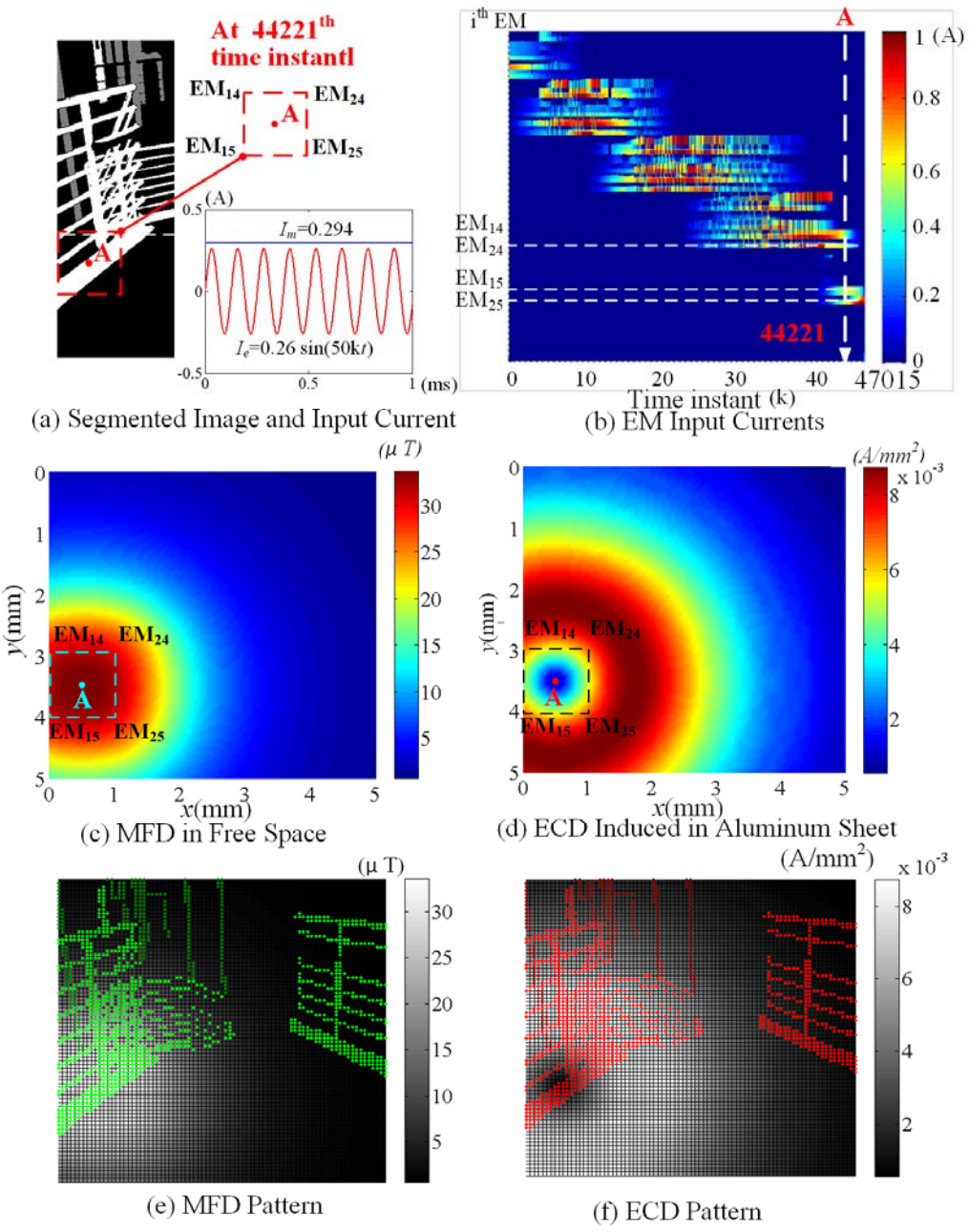

Figure 2-4 Eddy-current scanning application

As shown in Figs. 2-4(c) and 2-4(d) where the distributions of the MFD in free space and the ECD induced in the aluminum sheet at 44221th time instant are graphed, the MFD has a Gaussian shape whereas the ECD has a donut shape, and peak-MFD/ECD-

center are at point *A*. The stimulating points shown in Fig. 2-4(e), (f) are transduced in two levels. The amplitudes of dark points are half of light points. In Fig. 2-4(e), (f), green/red points are total 47015 points for transducing the "stair" image. The stimulating path is line by line from left-to-right, up to down. Amplitudes of dark color points are half of light color points. The gray level intensities of the background in Fig. 2-4(e), (f) are the norm of MFD and ECD for transducing the MFD peak/ECD center at point A at 44221th time instant. The norm of MFD/ECD can be calculated by taking the norm operation of B_x, B_y, B_z, E_x, E_y, which can be obtained by the modeling method for the exciting four EMs.

2.2 Effects of EM-Array Magnetic Scanning Method

Figure 2-5 illustrates the design concept of a magnetic scanner capable of moving the peak of the maximum magnetic flux density (MFD) on a plane at high speed. As shown in Fig. 2-5(b), the system consists of an $N_e \times N_e$ array of electromagnets (EMs). By appropriately manipulating the input currents of individual EMs, the peak of the resultant MFD can be manipulated.

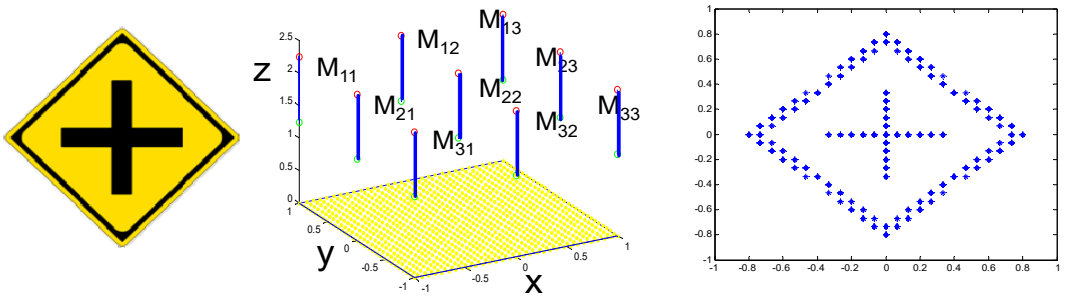

(a) Crossroad Sign (b) Array of EM actuators (c) Path of maximum MFD

Figure 2-5 Magnetic scanning for visual or tactile sensation

To enable high-resolution motion control of the maximum MFD with a few number of EM electrodes, design criteria are established for controlling the maximum MFD

between a pair of EMs based on a modified push-pull principle. As will be shown, this fundamental unit can be extended to 2D magnetic scanning with relatively high resolution.

2.2.1 Gaussian Approximation of MFD

To facilitate illustrating the design concept, consider the cylindrical air-cored EM coil (with length ℓ, and inside and outside diameters of $2a_i$ and $2a_o$ respectively) as shown in Fig. 2-6(a). The z-component of its MFD distribution on the plane at $z = h + \ell / 2$ can be modeled as a modified Gaussian-like function in the normalized form:

$$\frac{B_z(u,v)}{B_o} = A\exp\left[-\frac{(u-\mu_u)^2+(v-\mu_v)^2}{2\sigma^2}\right] \tag{2.9a}$$

where $(u, v)=(x, y)/a_o$. In Eq. (2.9a), B_o is the MFD of the EM at (0, 0, h) when 1A current passes through it; (μ_u, μ_v) define the EM center; and σ is the scaling factor resembling the standard deviation. The MFD distribution can be determined from analytical solutions, numerical simulation or reconstructed from experimental measurements. For a symmetrical EM where $\mu_u = \mu_v = 0$ and $\sigma_u=\sigma_v=\sigma$, the shape parameters (B_0 and σ) of a Gaussian function can be computed from $B_{zu}=B_z(u, 0)$ and the z-component value of the measuring plane is $2H+L$, where $L=l/(2a_o)$ and $H=h/(2a_o)$:

$$B_0 = \frac{1}{\sqrt{2\pi}\sigma}\int_{-\infty}^{\infty} B_{zu}du \quad \text{and} \quad \sigma^2 = \frac{\int_{-\infty}^{\infty} u^2 B_{zu}du}{\int_{-\infty}^{\infty} B_{zu}du} \tag{2.9b,c}$$

The parametric effects of the normalized EM geometries (which are a_i/a_o, L and H) on the shape of the MFD distribution are shown in Fig. 2-6. The results suggest that σ

increases with H but at the expense of the peak value. For a specified EM geometry, the shape (B_o and σ) of the MFD distribution depends primarily on the location h. In the following discussion, only the z-component of the MFD is considered.

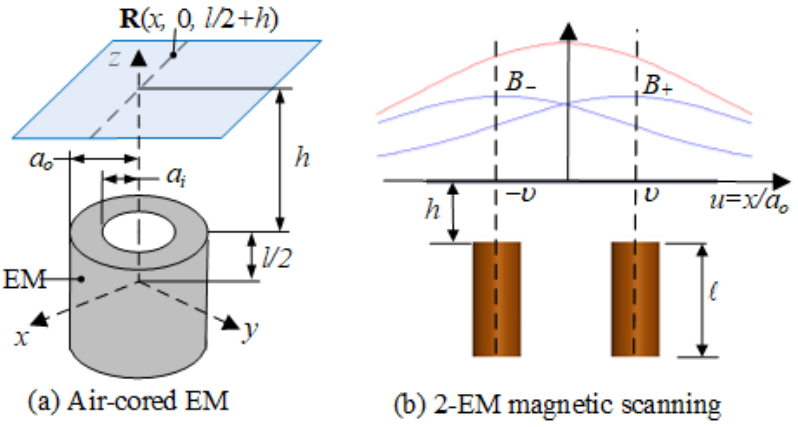

Figure 2-6 Schematics illustrating 1D Push-pull magnetic scanning

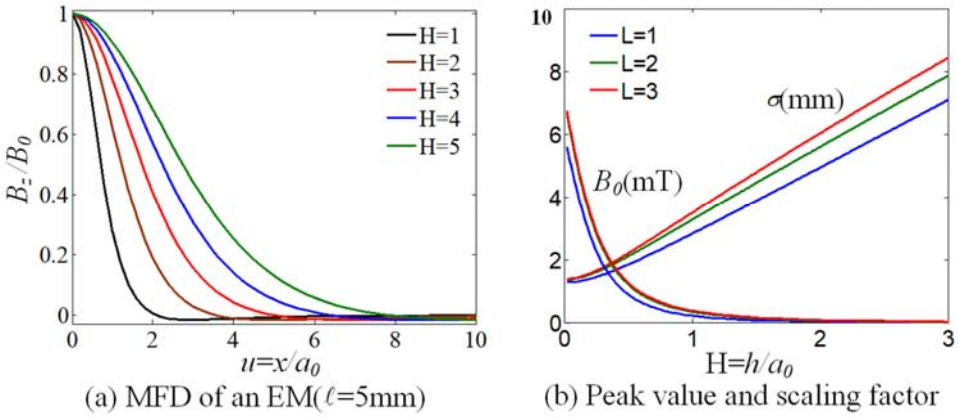

Figure 2-7 Magnetic flux density distribution of an EM (a_i=1mm, a_o=2.5mm)

2.2.2 Magnetic Scanning based on Push-Pull Principle

Consider a linear magnetic system (Fig. 2-6b) consisting of two EMs with circumferentially uniform MFD located at $x = \pm\upsilon/2,\ y = z = 0$. Their resultant MFD at

$z = h + \ell / 2$ along the *x* direction can be computed from the principle of superposition and characterized by a 1D Gaussian function:

$$B(u) = B_z / B_o = A_+ e^{-(u-\upsilon)^2/(2\sigma^2)} + A_- e^{-(u+\upsilon)^2/(2\sigma^2)} \tag{2.10}$$

The peak of the resultant MFD satisfies two conditions:

$$\frac{dB}{du} = 0,\ A_+(u-\upsilon)e^{u\upsilon/\sigma^2} + A_-(u+\upsilon)e^{-u\upsilon/\sigma^2} = 0 \tag{2.11a}$$

$$\frac{dB}{du} = 0,\ \frac{A_+}{A_-} + \frac{\left[\sigma^2 - (u+\upsilon)^2\right]}{\left[\sigma^2 - (u-\upsilon)^2\right]} e^{\frac{-2u\upsilon}{\sigma^2}} > 0 \tag{2.11b}$$

Operated on a push-pull principle,

$$A_\pm = A_o(1 \pm a_p) \text{ where } -1 \le a_p \le 1 \tag{2.11c}$$

The condition $dB_z/du=0$ becomes

$$u - \upsilon \tanh\left(\frac{u\upsilon}{\sigma^2}\right) + au \tanh\left(\frac{u\upsilon}{\sigma^2}\right) - a_p\upsilon = 0 \tag{2.12}$$

For magnetic scanning along a linear path, the resultant MFD must have a unique peak. The uniqueness implies that only one peak appears in the operating range. To offer intuitive insights into Eq. (2.12), the hyperbolic tangent function is divided into three regions of approximation:

$$\tanh\left(\frac{u\upsilon}{\sigma^2}\right)\approx\begin{cases}1 & u\upsilon\geq\sigma^2\\ u\upsilon/\sigma^2 & -\sigma^2<u\upsilon<\sigma^2\\ -1 & u\upsilon\leq-\sigma^2\end{cases} \tag{2.13}$$

For the two regions ($u\upsilon\geq\sigma^2$ and $u\upsilon\leq-\sigma^2$ with $A_{\pm}\neq 0$), the extreme value which can be derived by substituting $\tanh(u\upsilon/\sigma^2)=\pm 1$ into Eq. (2.12) occurs at $u=\pm\upsilon$. For the region $|u\upsilon|<\sigma^2$, Eq. (2.12) can be reduced similarly but the resulting form is a 2nd order equation in *u*:

$$f(u)=\left(\frac{a_p\upsilon}{\sigma^2}\right)u^2+\left(1-\frac{\upsilon^2}{\sigma^2}\right)u-a_p\upsilon=0 \tag{2.14a}$$

Since $f(u=\pm 1)=\pm\left(1-\upsilon^2\sigma^{-2}\right)-a_p\upsilon\left(1-\sigma^{-2}\right)$, we have (2.14b) for the range $-\upsilon\leq u\leq\upsilon$:

$$f(u=1)f(u=-1)\begin{cases}<0 & \sigma^2\geq\upsilon^2 \text{ and } 0<a,\upsilon\leq 1\\ \geq 0 & \sigma^2\geq\upsilon^2,\ a\geq 1 \text{ and } \upsilon=1\end{cases} \tag{2.14b}$$

The above implies that if $\sigma^2>1$ and $\left(a_p,\upsilon\right)<1$, there exists only one root in the ($-1\leq u/\upsilon\leq 1$) range indicating a local maximum based on the 2nd order derivative from Eq. (2.12):

$$\frac{1+a_p}{1-a_p}+\frac{1-\left[(u+\upsilon)/\sigma\right]^2}{1-\left[(u-\upsilon)/\sigma\right]^2}e^{-u\upsilon/\sigma^2}>0\Rightarrow\frac{d^2B_z}{du^2}<0$$

When $\sigma^2>1,\ \upsilon=1$ and $a_p>1$, two roots are in the $-\upsilon\leq u\leq\upsilon$ range. For magnetic scanning based on a single MFD peak in the range ($-1\leq u/\upsilon\leq 1$), the following two

conditions must be satisfied: $\sigma^2>1$ and $\left(a_p,\upsilon\right)\le 1$. The above discussions are best explained numerically with Fig. 2-8 which illustrates the parametric effects on the MFD:

- The first row, Fig. 2-8(a), demonstrates the effect of σ on the resultant MFD. When σ=0.5 (<1), two peaks are near $u=\pm\upsilon$ and a local minimum occurs in the range $(-1\le u/\upsilon\le 1)$. When σ=1, the MFD distribution is flat near u=0. When σ=2 (>1), there is only one peak in the range $(-1\le u/\upsilon\le 1)$ and has a good Gaussian shape.
- Similarly, the second row, Fig. 2-8(b), shows the effect of a on the resultant MFD. In general, the input range linearly maps onto the displacement range:

$$(-1\le a\le 1)\Leftrightarrow(-\upsilon\le u\le\upsilon)$$

Clearly, the resultant MFD distribution exhibits a peak at the limit $u=\upsilon$ when a=1.

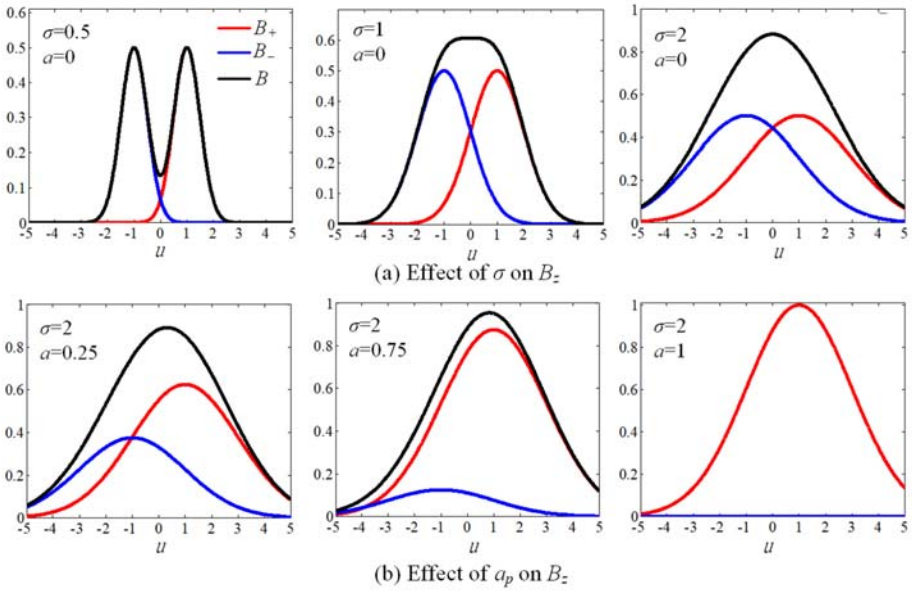

Figure 2-8 Magnetic flux density distribution, ($\mathbf{A}_{EM}$=0.5 and υ=1)

Gaussian approximation and 1D Scanning Example

The z-component MFD distribution of the cylinder air-core EM (Table 2-2) numerically integrated is graphed in Fig. 2-9(a).

Table 2-2 Values of the air-core EM parameters

EM (AWG 26 wire)	**Geometry** (mm)		**Gaussian fit**	
Inside radius	a_i	1	$\mu_u = \mu_v = 0$	
Outside radius	a_o	2.5	B_0 (mT)	0.0632
Length	ℓ	5	σ (mm)	5.1471
Distance from surface	H	10	A_0	0.5

The parameters of a 2D Gaussian fit Eq. (2.9a) that characterizes the computed MFD in Fig. 2-9(a) can then be derived from Eq. (2.9b, c). Given in the right column of Table 2-8, B_0=0.0632mT and σ=5.15. The percentage error distribution of the Gaussian fit B_G relative to the analytical solution B_A as defined in Eq. (2.15) is graphed in Fig. 2-9(b):

$$\varepsilon_G = 100(B_A - B_G)/B_{Amax} \tag{2.15}$$

The mean square and maximum errors are 0.011μT and 1.078μT respectively.

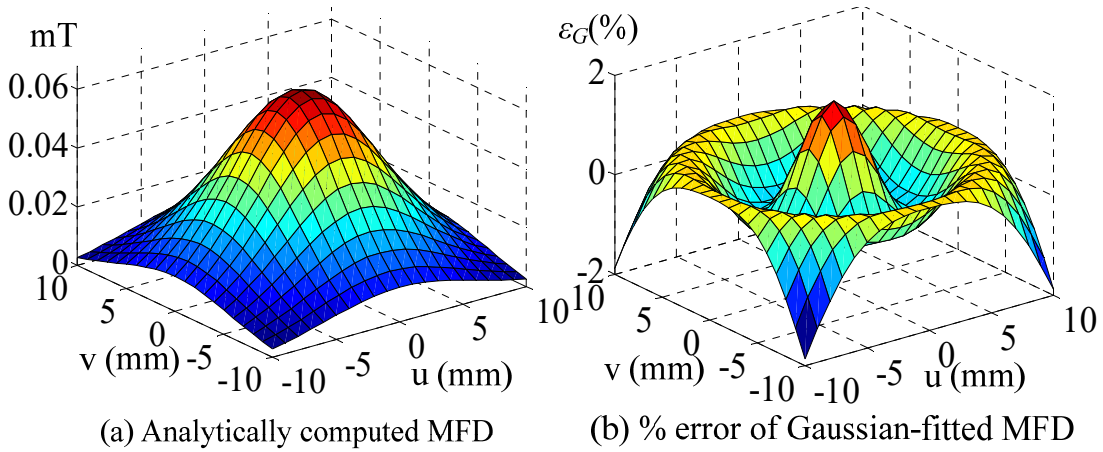

(a) Analytically computed MFD (b) % error of Gaussian-fitted MFD

Figure 2-9 z-component of MFD distribution of a multilayer EM (z=h)

To evaluate the concept feasibility of the magnetic scanning along a linear path, the effects of the push-pull operational principle Eq. (2.11c) on the resultant MFD Eq. (2.10) were investigated numerically in terms of the following performance criteria:

1) Linearity in the peak position u^* derived from Eq. (2.12) when mapping from $(-1 \le a \le 1)$ to $(-a\upsilon \le u \le a\upsilon)$

2) Synthesis of a resultant MFD B_c from the pair of EMs

3) Uniformity in maintaining the same MFD peak value

The linearity and synthesis are evaluated using the mean square errors (MSEs) defined in Eq. (2.16) and Eq. (2.17) respectively:

$$MSE_{linearity} = \frac{1}{2}\int_{-1}^{1}\left(u^* - a\upsilon\right)^2 da \tag{2.16}$$

$$MSE_{synthesis} = \frac{1}{4\upsilon}\int_{-\upsilon}^{\upsilon}\int_{-1}^{1}\left(B_c(u,a) - B_s(u,a)\right)^2 dadu \tag{2.17}$$

The MSE in Eq. (2.17), formulated as the mean square error of B_s with respect to B_c in the range $(-\upsilon \le u \le \upsilon;\ -1 \le a \le 1)$, provides an effective means to evaluate the effect of a single Gaussian $B_s(u, a)$ for fitting the sum of two Gaussians $B_c(u, a)$. The synthetized MFD compensated for uniformity can be generated from Eq. (2.18):

$$\frac{B_c(u,a)}{2A_o} = \frac{\left[\cosh(\frac{u\upsilon}{\sigma^2}) + a\sinh(\frac{u\upsilon}{\sigma^2})\right] e^{\frac{-u^2+(a\upsilon)^2}{2\sigma^2}}}{\left[\cosh\left(\frac{a\upsilon^2}{\sigma^2}\right) + a\sinh\left(\frac{a\upsilon^2}{\sigma^2}\right)\right]} \tag{2.18}$$

Some observations from the results given in Figs. 2-10 and 2-11 are discussed as follows:

– As shown in Fig. 2-10, the mapping linearity improves as σ increases. The maximum deviations from the $u^*=a$ line occur at $a=\pm 0.5$. When $\sigma \geq 2\upsilon$, the synthetized MFD is expected to exhibit a good Gaussian shape.

– Fig. 2-11(a), which shows the MSE of the synthesis, indicates the relationship between the standard deviations of the synthetized and original Gaussians (σ_s and σ respectively) is close to linear with σ_s slightly larger than σ.

– The uniformity of the scan is to maintain the MFD peak at a constant value. As shown in Fig. 2-11(b), the trajectory of the peak computed using Eq. (2.18) with $A_0=0.5$ for the range $(\upsilon = 1, -1 \leq a \leq 1)$ can be successfully maintained at unity.

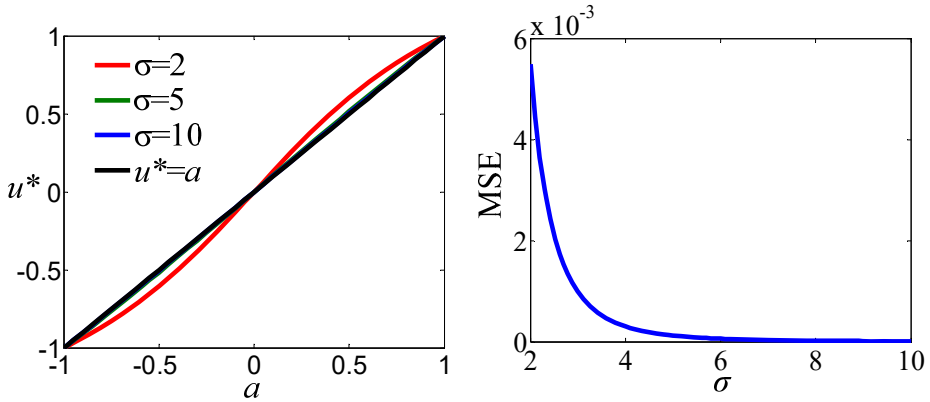

(a) Linearity between a and u^* (b) MSE of linearity

Figure 2-10 Effects of σ on linearity (υ=1)

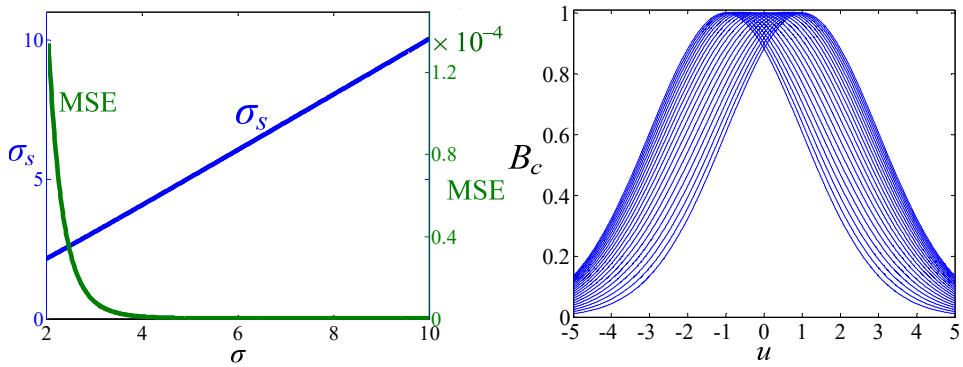

(a) Synthetized MFD (b) Uniformity of MFD Motion

Figure 2-11 Synthetized MFD and uniformity

2.3 Summary

The methods for controlling the continuous motion of its maximum Gaussian-like MFD in a plane at high speed and converting an image to magnetic/eddy-current patterns which includes eddy-current density formulation, input current manipulation, magnetic/electric field calculation, and color-based image segmentation has been presented in this chapter. The synthetized magnetic/electric fields are accurately controlled between adjacent EMs. The design concept and operational principle extend the applications of EM arrays by allowing continuous motion scanning between discrete points in a plane.

CHAPTER 3. DISTRIBUTED PARAMETER ELEMENT METHOD FOR PHYSICAL FIELD MODELING

This chapter presents a new method, called the distributed parameter element (DPE) method, to model the two or three dimensional irregular shape magnetic and electric field in state-space representation by applying the divergence theorem on each element to satisfy the conservation law and boundary conditions and account for the geometry, which provides a basis for the subsequent stationary, time dependent, and harmonic analysis. There are many advantages for control design, optimization due to the ideally available linear algebra tools. Figure 3-1 shows a physical field (ϕ_i) is divided to distributed parameter elements, and the irregular shape physical field is formulated by applying the divergence theorem on each element to satisfy the conservation law and boundary conditions of the linear partial differential equation.

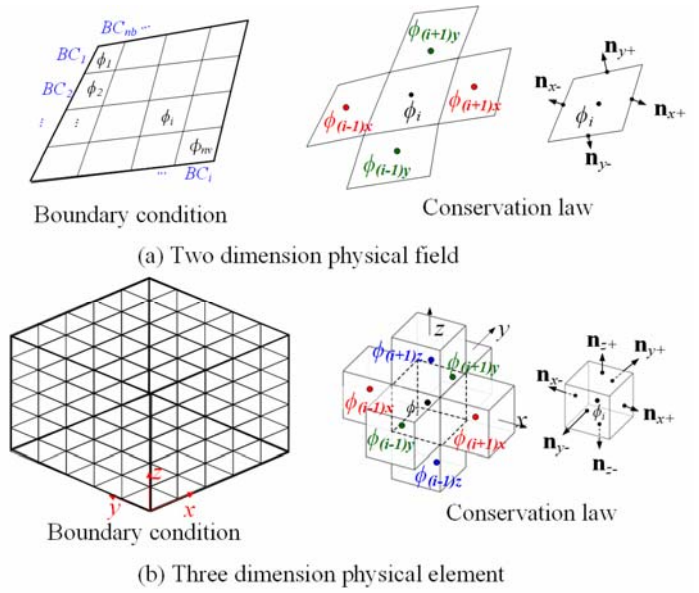

Figure 3-1 The distributed elements for physical field modeling

3.1 Scaler Potential Electric Field

Many physical fields can be formulated by a PDE (Eq. (3.1)) subject to boundary conditions Eq. (3.2a) and Eq. (3.2b) to solve for the scalar physical field value ϕ. Two boundary conditions are considered in the formulation: 1) Dirichlet BC, and 2) Neumann BC. ϕ_b is the fixed physical field boundary value. F_{n0} and F_{n1} are zero and first order coefficients of the inward flux. The definitions and units of coefficients of the linear PDE in Eq. (3.1a) are listed in Table 3-1. C_t, C_f, C_α, ϕ_b, F_{n0}, F_{n1} are scales. $\mathbf{C}_d$, $\mathbf{C}_p$ are $n_d \times n_d$ matrices. $\mathbf{C}_\alpha$, $\mathbf{C}_\beta$ are $n_d \times 1$ column vectors, where n_d (=2 or 3) is the dimension of the space.

$$C_t \frac{\partial \phi}{\partial t} + \nabla \bullet \left(-\mathbf{C}_d \nabla \phi + \mathbf{C}_e \frac{\partial}{\partial t} \nabla \phi - \mathbf{C}_\alpha \phi \right) + \mathbf{C}_\beta \bullet \nabla \phi + C_a \phi = C_f \tag{3.1a}$$

Dirichlet BC: $\phi = \phi_b$ (3.2a)

Neumann BC: $$-\mathbf{n} \bullet \nabla \bullet \left(-\mathbf{C}_d \nabla \phi + \mathbf{C}_p \frac{\partial}{\partial t} \nabla \phi - \mathbf{C}_\alpha \phi \right) = F_{no} - F_{n1} \phi \tag{3.2b}$$

Table 3-1 Coefficients of PDE

Symbol	Definitions	Unit
$\mathbf{C}_d$	Diffusion coefficient	1
C_a	Absorption coefficient	$1/m^2$
C_f	Source term	$1/m^2$
C_t	Damping or mass coefficient	s/m^2
$\mathbf{C}_e$	Time Derivative Diffusion coefficient	s
$\mathbf{C}_\alpha$	Conservative flux convection coefficient	1/m
$\mathbf{C}_\beta$	Conservative coefficient	1/m
ϕ_b	Variable of Dirichlet BC	1
F_{no}, F_{n1}	Variables of Neumann BC	1

The DPE method models the scalar physical field with different boundary conditions into state-space representation. As shown in Table 3-2, **x** is the column vector of scalar physical filed values, and **u** is the column vector of element or surface source values. The governing equations of the electric field are scalar potential partial differential equations (PDEs), and the magnetic field are vector potential PDEs. The electric field can be formulated by a linear PDE with coefficients $\mathbf{C}_d=\sigma\mathbf{I}$, $\mathbf{C}_p=\varepsilon\mathbf{I}$, $\mathbf{C}_\alpha=\mathbf{C}_\beta=\mathbf{0}$, $C_a=0$, $C_f=Q_r$. However, the governing equations of the magnetic field are vector potential PDEs. The physical field values in three dimensions need to be considered. Therefore, the matrix for calculations becomes larger. More importantly, there are the curl operator and cross product in the governing equations of magnetic fields. A distributed current source method based on the mutual induction is applied to avoid the complicated calculations of the curl operator and cross product.

Table 3-2 Distributed Parameter Element Method, Magnetic/Electric Field Equations

Linear PDE:	State-space representation:
$C_t\frac{\partial\phi}{\partial t}-\nabla\cdot\left(\mathbf{C}_d\nabla\phi+\mathbf{C}_e\frac{\partial\nabla\phi}{\partial t}+\mathbf{C}_\alpha\phi\right)$ $+\mathbf{C}_\beta\cdot\nabla\phi+C_a\phi=C_f$	$\dot{\mathbf{x}}=[\boldsymbol{\alpha}]\mathbf{x}+[\boldsymbol{\beta}]\mathbf{u}$ $\mathbf{x}=[\phi_1 \quad \phi_2 \quad \cdots \quad \phi_{nv}]^T$ $\mathbf{u}=[\varphi_1 \quad \varphi_2 \quad \cdots \quad \varphi_{ns}]^T$
Electric Field: $\nabla\cdot\left(\sigma\nabla\mathrm{V}+\frac{\partial\varepsilon\nabla\mathrm{V}}{\partial t}\right)=Q_r,\ \mathbf{E}=-\nabla V$ $\left(\mathbf{C}_d=\sigma\mathbf{I},\mathbf{C}_e=\varepsilon\mathbf{I},\mathbf{C}_\alpha=\mathbf{C}_\beta=\mathbf{0},C_a=0,C_f=Q_r\right)$	Magnetic Field: Harmonic: $\left(j\omega\sigma-\omega^2\varepsilon\right)\mathbf{A}+\nabla\times\left(\mu^{-1}\nabla\times\mathbf{A}\right)=\mathbf{J}_\mathbf{e}$ Time Dependent: $\sigma\frac{\partial}{\partial t}\mathbf{A}+\nabla\times\left(\mu^{-1}\nabla\times\mathbf{A}\right)=\mathbf{J}_\mathbf{e}$

The basic concept of the distributed model is that the physical fields are divided to distributed elements. The irregular shape physical fields can be formulated in state-space representation by applying the divergence theorem on each element to satisfy the conservation law and boundary conditions. This modeling method combines the advantages of the finite difference method (FDM) and finite volume method (FVM), which utilizes the FDM to calculate the first order derivative and the divergence theorem to account for the conservation law. Compared with some existing methods, the DPE method can calculate the irregular geometry physical fields, which finite difference method (FDM) and finite volume method (FVM) requires far more efforts, and the DPE method is more physical intuitive and simpler than the finite element analysis (FEA).

3.1.1 Steady-State Formulation

The second term in Eq. (3.1) can be calculated in an integral form by applying the divergence theorem in Eq. (3.3) for considering the geometry properties of elements. By substituting Eq. (3.3) into Eq. (3.1) and discretizing the equation, the equation of the parameters of each element is obtained in Eq. (3.4), where the subscript i represents i^{th} element. nv is the number of surface and volume element for 2D and 3D respectively.

$$\int_V \nabla \cdot \left(\mathbf{C}_d \nabla \phi + \mathbf{C}_e \frac{\partial \nabla \phi}{\partial t} + \mathbf{C}_\alpha \phi \right) d\mathbf{V} = \oint_s \left(\mathbf{C}_d \nabla \phi + \mathbf{C}_e \frac{\partial \nabla \phi}{\partial t} + \mathbf{C}_\alpha \phi \right) \cdot d\mathbf{s} \tag{3.3}$$

$$C_t \frac{\partial \phi_i}{\partial t} - \sum_{i=1}^{2n_d} s_i \mathbf{n}_i \cdot \left(\mathbf{C}_{di} \nabla \phi_i + \mathbf{C}_{ei} \frac{\partial \nabla \phi_i}{\partial t} + \mathbf{C}_{\alpha i} \phi_i \right) + \mathbf{C}_\beta \cdot \nabla \phi_i + C_{ai} \phi_i = C_{fi}, \ (i = 1, 2, ..., n_v) \tag{3.4}$$

The DPE method concatenates n_v equations of Eq. (3.4) in the matrix form in the state-space representation by considering the boundary conditions of boundary elements

and conservation law of each element in Eq. (3.5a). $\mathbf{x}\left(\in \mathbb{R}^{n_v \times 1}\right)$ is the state vector of the physical field values (ϕ_i, $i=1 \sim n_v$). $\mathbf{u}\left(\in \mathbb{R}^{n_s \times 1}\right)$ is the input vector for the source values. There are two kinds of sources. One is the element source, and the other is boundary source. n_s is equal to n_v plus n_b. n_s is the number of total sources. n_b is the number of boundary source. For the element source, ϕ_i refers to f_i in Eq. (3.4). For the boundary source, ϕ_i refers to ϕ_{bi}, F_{n0i} in Eq. (3.2a), Eq. (3.2b) for Dirichlet and Neumann BC respectively.

$\left[\boldsymbol{\alpha}_\ell\right]\left(\in \mathbb{R}^{n_v \times n_v}\right), \ell = d, e$ and $\left[\boldsymbol{\beta}_\ell\right]\left(\in \mathbb{R}^{n_v \times n_s}\right)$ are the state and input matrices. $\left[\boldsymbol{\alpha}_\ell\right]$ and $\left[\boldsymbol{\beta}_\ell\right]$ are composed of $\boldsymbol{\alpha}_{\ell e(i)}\left(\in \mathbb{R}^{1 \times n_v}\right)$ and $\boldsymbol{\beta}_{\ell e(i)}\left(\in \mathbb{R}^{1 \times n_s}\right)$, $i=1 \sim n_v$ Eq. (3.4b, c). $\boldsymbol{\alpha}_{\ell e(i)}\left(\in \mathbb{R}^{1 \times n_v}\right)$ and $\boldsymbol{\beta}_{\ell e(i)}\left(\in \mathbb{R}^{1 \times n_s}\right)$ are determined from Eq. (3.5d, e). $\boldsymbol{\lambda}_{vi}\left(\in \mathbb{R}^{1 \times n_v}\right)$ and $\boldsymbol{\lambda}_{sk}\left(\in \mathbb{R}^{1 \times ns}\right)$ are unit vectors to map the corresponding i^{th} element in **x** and **u** respectively. $\boldsymbol{\alpha}_{\ell s(i,j)}\left(\in \mathbb{R}^{1 \times n_v}\right)$ and $\boldsymbol{\beta}_{\ell s(i,j)}\left(\in \mathbb{R}^{1 \times n_s}\right)$ account for the divergence theorem of the i^{th} element, j^{th} surface. $\boldsymbol{\lambda}_{\mathbf{(i+1)x}}$, $\boldsymbol{\lambda}_{\mathbf{(i+1)y}}$, $\boldsymbol{\lambda}_{\mathbf{(i+1)z}}$ are the indices to the front, right, up element of the i^{th} element. Three surface types are considered on the DPE method: 1) Inner surface, 2) Dirichlet boundary surface, 3) Neumann boundary surface. Different surface types correspond to different $\boldsymbol{\alpha}_{\ell s(i,j)}\left(\in \mathbb{R}^{1 \times n_v}\right)$, $\boldsymbol{\beta}_{\ell s(i,j)}\left(\in \mathbb{R}^{1 \times n_s}\right)$ in Eq. (3.5f), Eq. (3.5g). For the inner surface, the coefficient of 0.5 in $\boldsymbol{\alpha}_{ds(i,j)}$ indicates the half value of the i^{th} element and its neighboring element. $\boldsymbol{\lambda}_{sk}$ is the index to map to the i^{th} element, j^{th} surface, which equals to the k^{th} boundary surface. The descriptions of variables are shown in Table 3-3. To avoid of divergence, if Δx, Δy, Δz, x_j-x_i, y_j-y_i, z_j-z_i, x_b-x_i, y_b-y_i, z_b-z_i is smaller than a threshold (ε_{th}),

the values are adjusted to infinite. $\mathbf{C_i}$ and $\mathbf{C_j}$ are the diffusion matrices of i^{th} element and the element connecting i^{th} element j^{th} surface respectively.

$$\begin{aligned}&\left[\boldsymbol{\alpha}_d\right]\mathbf{x}+\left[\boldsymbol{\alpha}_e\right]\dot{\mathbf{x}}+\left[\boldsymbol{\beta}_d\right]\mathbf{u}+\left[\boldsymbol{\beta}_e\right]\dot{\mathbf{u}}=0\\&\mathbf{x}=\left[\phi_1 \quad \phi_2 \quad \cdots \quad \phi_{n_v}\right]^{\mathrm{T}}\\&\mathbf{u}=\left[\varphi_1 \quad \varphi_2 \quad \cdots \quad \varphi_{n_s}\right]^{\mathrm{T}}\end{aligned} \tag{3.5a}$$

$$\left[\boldsymbol{\alpha}_\ell\right]=\left[\boldsymbol{\alpha}_{\ell e(1)}^{\mathrm{T}} \quad \boldsymbol{\alpha}_{\ell e(2)}^{\mathrm{T}} \quad \cdots \quad \boldsymbol{\alpha}_{\ell e(n_v)}^{\mathrm{T}}\right]^{\mathrm{T}}, \ell=d,e \tag{3.5b}$$

$$\left[\boldsymbol{\beta}_\ell\right]=\left[\beta_{\ell e(1)}^{\mathrm{T}} \quad \beta_{\ell e(2)}^{\mathrm{T}} \quad \cdots \quad \beta_{\ell e(n_v)}^{\mathrm{T}}\right]^{\mathrm{T}} \tag{3.5c}$$

$$\boldsymbol{\alpha}_{\ell e(i)}=\left(v_i C_t\right)^{-1}\sum_{j=1}^{2n_d}\boldsymbol{\alpha}_{\ell s(i,j)}-C_t^{-1}\mathbf{C}_\beta^T\bullet\boldsymbol{\Lambda}_\phi-C_t^{-1}C_a\boldsymbol{\lambda}_{vi} \tag{3.5d}$$

where $\boldsymbol{\Lambda}_\phi=\left[\dfrac{\boldsymbol{\lambda}_{v(i+1)x}-\boldsymbol{\lambda}_{vi}}{x_{v(i+1)x}-x_{vi}} \quad \dfrac{\boldsymbol{\lambda}_{v(i+1)y}-\boldsymbol{\lambda}_{vi}}{x_{v(i+1)y}-x_{vi}} \quad \dfrac{\boldsymbol{\lambda}_{v(i+1)z}-\boldsymbol{\lambda}_{vi}}{x_{v(i+1)z}-x_{vi}}\right]^{\mathrm{T}}$,

$$\boldsymbol{\lambda}_{vi}\left(\in\mathbb{R}^{1\times n_v}\right)=\begin{cases}1 & i^{th}\text{ volume element}\\0 & \text{others}\end{cases}$$

$$\boldsymbol{\beta}_{\ell e(i)}\left(\in\mathbb{R}^{1\times n_s}\right)=\left(v_i C_t\right)^{-1}\sum_{j=1}^{2n_d}\boldsymbol{\beta}_{\ell s(i,j)}+C_t^{-1}\boldsymbol{\lambda}_{sk} \tag{3.5e}$$

where $\boldsymbol{\lambda}_{sk}\ \left(\in\mathbb{R}^{1\times n_s}\right)=\begin{cases}1 & k^{th}\text{ source}\\0 & \text{others}\end{cases}$

$$\boldsymbol{\alpha}_{\ell s(i,j)}=\begin{cases}0.5s_{i,j}\left[\boldsymbol{\Lambda}_d\bullet\left(\mathbf{C}_{\ell j}+\mathbf{C}_{\ell i}\right)\bullet\mathbf{n}_{i,j}\left(\mathbf{C}_{\ell j}-\mathbf{C}_{\ell i}\right)+\mathbf{C}_{\alpha i}^{\mathrm{T}}\bullet\mathbf{n}_{i,j}\left(\mathbf{C}_{\ell j}+\mathbf{C}_{\ell i}\right)\right], \text{ Inner surface}\\-s_{i,j}\boldsymbol{\Lambda}_b\bullet\mathbf{C}_{\ell i}\bullet\mathbf{n}_{i,j}\boldsymbol{\lambda}_{vi}, \text{Dirichlet boundary surface}\\-s_{i,j}F_{n1}\boldsymbol{\lambda}_{vi}, \text{Neumann boundary surface}\end{cases} \tag{3.5f}$$

where $\boldsymbol{\Lambda}_d=\left[\left(x_j-x_i\right)^{-1} \quad \left(y_j-y_i\right)^{-1} \quad \left(z_j-z_i\right)^{-1}\right]$

$\boldsymbol{\Lambda}_b=\left[\left(x_b-x_i\right)^{-1} \quad \left(y_b-y_i\right)^{-1} \quad \left(z_b-z_i\right)^{-1}\right]$

$$\boldsymbol{\beta}_{\ell s(i,j)}=\begin{cases}0, \text{ Inner surface}\\ s_{i,j}\left(\boldsymbol{\Lambda}_b \bullet \mathbf{C}_{\ell i} \bullet \mathbf{n}_{i,j}+\mathbf{C}_{\alpha i}^{\mathrm{T}} \bullet \mathbf{n}_{i,j}\right)\boldsymbol{\lambda}_{vk}, \text{ Dirichlet boundary surface}\\ s_{i,j}\boldsymbol{\lambda}_{vk}\ , \text{ Neumann boundary surface}\end{cases} \quad (3.5g)$$

Table 3-3 Definitions and unit of variables

Variable	Definitions	Unit
v_{di}	3D: the volume of i^{th} element	m^3
	2D: the area of i^{th} element	m^2
$s_{i,j}$	3D: the area of i^{th} element, j^{th} surface	m^2
	2D: the length of i^{th} element, j^{th} line	m
(x_i, y_i, z_i)	the position of i^{th} element	m
ϕ_b	Variable of Dirichlet BC	1
F_{n0}, F_{n1}	Variables of Neumann BC	m^{-1}

3.1.2 Geometry Properties

Nodes and elements are basic components to express the geometry of the fields. Figure 3-2 demonstrates that the global fields are composed of many nodes and elements in two and three dimension. Each node is a 2×1 or 3×1 column vectors in 2D and 3D Cartesian coordinate. Each local quadrilateral/hexagonal element consists of four/eight nodes. The nodes can be arranged in the counterclockwise directions from the node in the most *x*-, *y*- directions for two dimension, and most *x*-, *y*-, *z*- directions of the bottom layer and then most *x*-, *y*-, *z*+ for 3D as shown in Fig. 3-2. After arranging the nodes, the line/surface can be labeled. For example, p_1p_2 is the s_{y-} line and $p_1p_2p_3p_4$ is the s_{y-} surface. Then, the relative position of each element can be determined.

In two dimension, the side lengths (s_ℓ, ℓ=$x\pm$, $y\pm$) and normal vector ($\mathbf{n}_\ell$, ℓ=$x\pm$, $y\pm$) can be determined by Eq. (3.6a), Eq. (3.6b). The area of quadrilateral element (v_i) can be determined by summation of the areas of two triangles Eq. (3.6c).

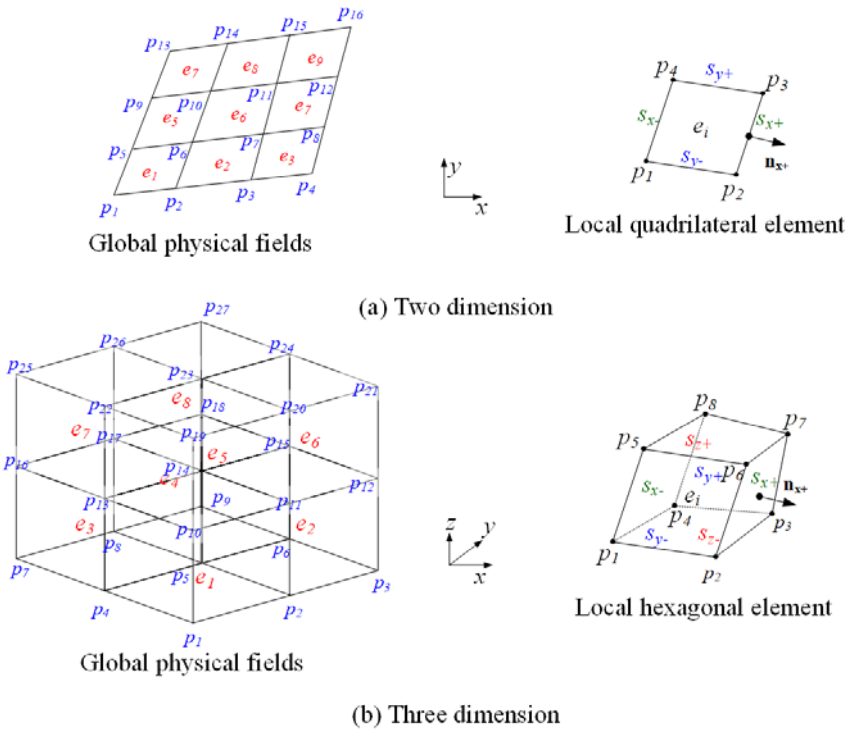

Figure 3-2 Geometry nodes and elements

$$s_{x+} = |\mathbf{p}_3 - \mathbf{p}_2|, s_{x-} = |\mathbf{p}_1 - \mathbf{p}_4|, s_{y+} = |\mathbf{p}_4 - \mathbf{p}_3|, s_{y-} = |\mathbf{p}_2 - \mathbf{p}_1| \tag{3.6a}$$

$$\mathbf{n}_{x+} = \begin{bmatrix} p_{3y} - p_{2y} & p_{3x} - p_{2x} \end{bmatrix}^T, \mathbf{n}_{y+} = \begin{bmatrix} p_{4y} - p_{3y} & p_{4x} - p_{3x} \end{bmatrix}^T \tag{3.6b}$$

$$\mathbf{n}_{x-} = \begin{bmatrix} p_{1y} - p_{4y} & p_{1x} - p_{4x} \end{bmatrix}^T, \mathbf{n}_{y-} = \begin{bmatrix} p_{2y} - p_{1y} & p_{2x} - p_{1x} \end{bmatrix}^T$$

$$v_i = 0.5\left(|\mathbf{p}_2 - \mathbf{p}_1| \times |\mathbf{p}_4 - \mathbf{p}_1| + |\mathbf{p}_2 - \mathbf{p}_3| \times |\mathbf{p}_4 - \mathbf{p}_3|\right) \tag{3.6c}$$

In three dimension, in Eq. (3.7a, b), the vertexes $\mathbf{p}_{\ell i}$ (where i=1, 2, 3 and 4) for the ℓ quadrilateral surface (made of two triangles) are tabulated on the left side of Table 3.4. Equation (3.7c) sums the six tetrahedron volumes (denoted as t_i =1 to 6) that make up the hexahedron, where $\mathbf{p}_{ti,i}$ are listed on the right side of Table 3-4.

$$s_\ell = 0.5\left(\left|\mathbf{p}_{\ell 2}-\mathbf{p}_{\ell 1}\right|\times\left|\mathbf{p}_{\ell 4}-\mathbf{p}_{\ell 1}\right|+\left|\mathbf{p}_{\ell 2}-\mathbf{p}_{\ell 3}\right|\times\left|\mathbf{p}_{\ell 4}-\mathbf{p}_{\ell 3}\right|\right) \tag{3.7a}$$

$$\mathbf{n}_\ell = \frac{\left(\mathbf{p}_{\ell 2}-\mathbf{p}_{\ell 1}\right)\times\left(\mathbf{p}_{\ell 3}-\mathbf{p}_{\ell 1}\right)}{\left|\left(\mathbf{p}_{\ell 2}-\mathbf{p}_{\ell 1}\right)\times\left(\mathbf{p}_{\ell 3}-\mathbf{p}_{\ell 1}\right)\right|}, \text{ where } \ell = x_\pm, y_\pm, z_\pm \tag{3.7b}$$

$$v = \frac{1}{2}\sum_{ti=1}^{6}\left\{\left(\mathbf{p}_{ti,4}-\mathbf{p}_{ti,1}\right)\bullet\left[\left(\mathbf{p}_{ti,2}-\mathbf{p}_{ti,1}\right)\times\left(\mathbf{p}_{ti,3}-\mathbf{p}_{ti,1}\right)\right]\right\} \tag{3.7c}$$

Table 3-4 Vertexes of Tetrahedrons and Surfaces

ℓ	$\mathbf{p}_{\ell 1}$	$\mathbf{p}_{\ell 2}$	$\mathbf{p}_{\ell 3}$	$\mathbf{p}_{\ell 4}$		$\mathbf{p}_{ti,1}$	$\mathbf{p}_{ti,2}$	$\mathbf{p}_{ti,3}$	$\mathbf{p}_{ti,4}$
$x+$	$\mathbf{p}_2$	$\mathbf{p}_3$	$\mathbf{p}_7$	$\mathbf{p}_6$	t_1	$\mathbf{p}_1$	$\mathbf{p}_2$	$\mathbf{p}_4$	$\mathbf{p}_5$
$x-$	$\mathbf{p}_1$	$\mathbf{p}_5$	$\mathbf{p}_8$	$\mathbf{p}_4$	t_2	$\mathbf{p}_5$	$\mathbf{p}_4$	$\mathbf{p}_8$	$\mathbf{p}_6$
$y+$	$\mathbf{p}_3$	$\mathbf{p}_4$	$\mathbf{p}_8$	$\mathbf{p}_7$	t_3	$\mathbf{p}_5$	$\mathbf{p}_6$	$\mathbf{p}_2$	$\mathbf{p}_4$
$y-$	$\mathbf{p}_1$	$\mathbf{p}_2$	$\mathbf{p}_6$	$\mathbf{p}_5$	t_4	$\mathbf{p}_3$	$\mathbf{p}_7$	$\mathbf{p}_8$	$\mathbf{p}_6$
$z+$	$\mathbf{p}_5$	$\mathbf{p}_6$	$\mathbf{p}_7$	$\mathbf{p}_8$	t_5	$\mathbf{p}_2$	$\mathbf{p}_3$	$\mathbf{p}_4$	$\mathbf{p}_6$
$z-$	$\mathbf{p}_1$	$\mathbf{p}_4$	$\mathbf{p}_3$	$\mathbf{p}_2$	t_6	$\mathbf{p}_4$	$\mathbf{p}_3$	$\mathbf{p}_8$	$\mathbf{p}_6$

The governing equation of electric field is expressed in the left column of Table 3-1, where V is the electric potential (Voltage), σ is the electrical conductivity (Sm^{-1}), ε is the electric permittivity(Fm^{-1}), Q_r is the resistive loss. The electric field ($\mathbf{E}$) is negative of the gradient of the electric potential (V). The time dependent response of the electric field Eq. (3.9) can be determined by applying implicit Euler method Eq. (3.8) on Eq. (3.5a).

$$\left[\boldsymbol{\alpha}_\sigma\right]\mathbf{x(k+1)}+\left[\boldsymbol{\alpha}_\varepsilon\right]\left[\frac{\mathbf{x(k+1)}-\mathbf{x(k)}}{\Delta t}\right]+\left[\boldsymbol{\beta}_\sigma\right]\mathbf{u(k)}+\left[\boldsymbol{\beta}_\varepsilon\right]\left[\frac{\mathbf{u(k+1)}-\mathbf{u(k)}}{\Delta t}\right]=0 \tag{3.8}$$

$$\mathbf{x(k+1)}=\left[\left[\boldsymbol{\alpha}_\varepsilon\right]+\Delta t\left[\boldsymbol{\alpha}_\sigma\right]\right]^{-1}\left[\boldsymbol{\alpha}_\varepsilon\right]\mathbf{x(k)}-\Delta t\left[\left[\boldsymbol{\alpha}_\varepsilon\right]+\Delta t\left[\boldsymbol{\alpha}_\sigma\right]\right]^{-1}\left[\left[\boldsymbol{\beta}_\varepsilon\right]\Delta t^{-1}\mathbf{u(k+1)}+\left[\left[\boldsymbol{\beta}_\sigma\right]-\left[\boldsymbol{\beta}_\varepsilon\right]\Delta t^{-1}\right]\mathbf{u(k)}\right] \tag{3.9}$$

3.1.3 Numerical Verification

To verify the DPE method, both 2D and 3D, stationary (C_t=0) and time domain ($C_t \neq 0$) are compared with the FEA software (Comsol). Figure 3-3 shows the 2D and 3D simulation objects. The objects are square and cube with side lengths 10m consisting of 64 square and 512 cube elements with side length 1.25m. The boundary conditions (BC_1~BC_4)

of the square object are x-, y_+, x+, y- boundary surfaces, and the boundary conditions (BC_1~BC_6) of the cubic object are z+, z-, x-, y+, x+, y- boundary surfaces.

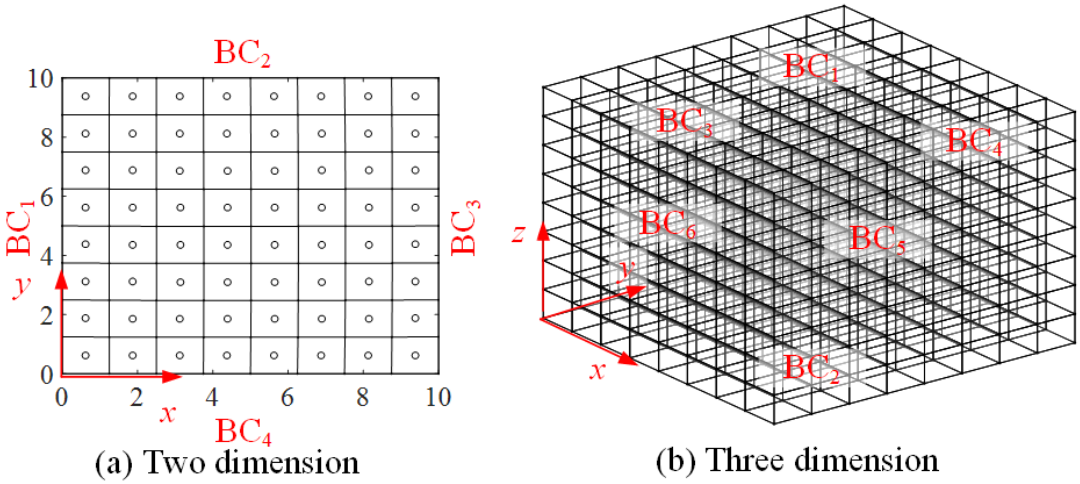

Figure 3-3 Simulation configuration

3.1.4 2D Simulation

Two cases of different PDE coefficients and boundary conditions are utilized to verify the DPE model as shown in Table 3-5 and 3-6. Case A only has Dirichlet boundary and $\mathbf{C}_\alpha=\mathbf{C}_\beta=\mathbf{0}$. Case B only has both Dirichlet and Neumann boundaries and $\mathbf{C}_\alpha$, $\mathbf{C}_\beta$ are not zero vector. Figure 3-4(a) and (b) compares the stationary simulation results with FEA. To provide the quantitative comparisons, the relative differences between the DPE model and FEA are expressed in percentage as follows: where ϕ_{FEA_Max} is the maximum ϕ value, which is equal to 100 in these two cases.

$$\frac{\phi_{\mathrm{DPE}}-\phi_{\mathrm{FEA}}}{\phi_{\mathrm{FEA\_Max}}}\times 100\%$$

The average percentage errors are 0.455% and 1.932% for case A and B respectively. Figure 3-4(c), (d) are the simulation results of the time responses for three points (P_1: x=3.125m, y=6.875m, P_2: x=5.625m, y=5.625m, P_3: x=8.125m, y=8.125m) with the parameters of case A, B. The time interval is 1 ms and C_t is 1.

Table 3-5 Coefficients of PDE values

Case	C_a	C_f	$\mathbf{C_d}$	$\mathbf{C_e}$	$\mathbf{C_\alpha}$	$\mathbf{C_\beta}$
A	2	3	Isotropic, 3	**0**	$[0\ 0]^T$	$[0\ 0]^T$
B	3	1	Isotropic, 1	**0**	$[1\ 0]^T$	$[2\ 1]^T$

Table 3-6 Boundary conditions

Case	BC_1	BC_2	BC_3	BC_4
A	ϕ_b =0	ϕ_b =100	ϕ_b =0	ϕ_b =50
B	ϕ_b =0	ϕ_b =100	F_{n0}=0, F_{n1}=0	F_{n0}=100, F_{n1}=50

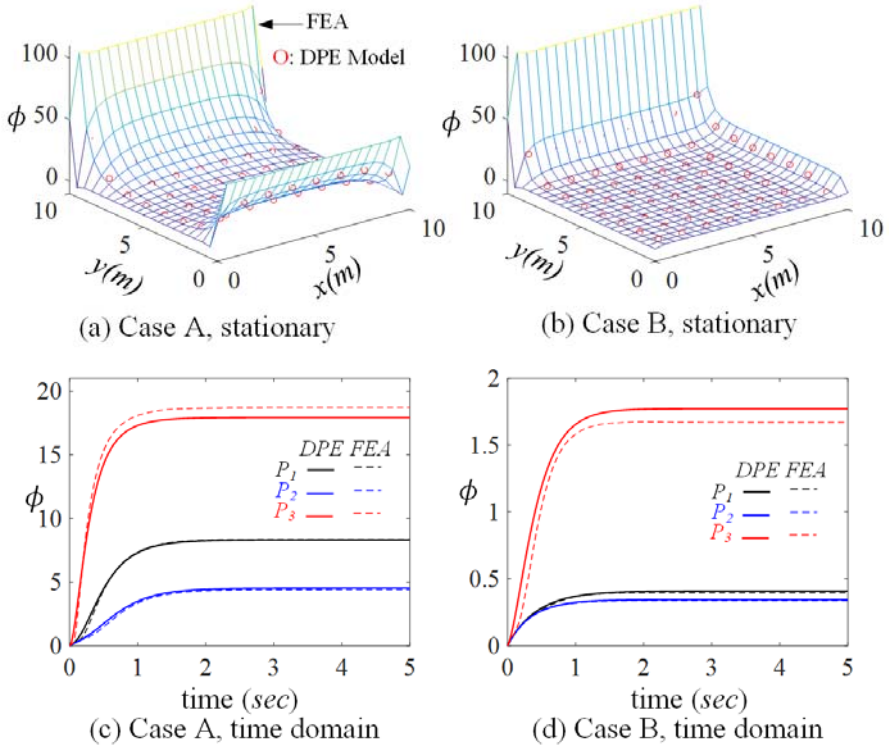

Figure 3-4 Two-dimension simulation results

3.1.5 3D Simulation

Similar to two-dimension case, two cases of different PDE coefficients and boundary conditions are utilized to verify the DPE model in three dimension as shown in Table 3-7 and 3-8. Fig. 3-5(a), (b) compares the stationary simulation results with FEA in y=5.625m plane. The average percentage errors are 2.021% and 0.343% for case C and D respectively. Fig. 3-5(c), (d) are the simulation results of the time responses for three points (P_4: x=0.625m, y=0.625m, z=0.625m, P_5: x=3.125m, y=6.875m, z=4.375m P_6: x=5.625m, y=5.625m, y=5.625m) with the parameters of case C, D. The time interval is 1 ms and C_t is 1. As a rule of thumb, the calculations with a PC (Intel Core i7-3630QM, 2.40GHz CPU, 16GB RAM, 64 bits OS) take about 2.62 seconds for a 10×10×10-element and 96.43 seconds for a 15×15×15-element for the 3D DPE model.

Table 3-7 Coefficients of PDE values

Case	C_a	C_f	$\mathbf{C_d}$	$\mathbf{C_e}$	$\mathbf{C_\alpha}$	$\mathbf{C_\beta}$
C	2	3	Isotropic, 10	**0**	$[0\ 0\ 0]^T$	$[0\ 0\ 0]^T$
D	3	1	Isotropic, 20	**0**	$[1\ 0\ 1]^T$	$[2\ 1\ 3]^T$

Table 3-8 Boundary conditions

Case	BC_1	BC_2	BC_3	BC_4	BC_5	BC_6
C	ϕ_b=100	ϕ_b=50	ϕ_b=0	ϕ_b=50	ϕ_b=0	ϕ_b=100
D	ϕ_b=100	ϕ_b=50	ϕ_b=0	F_{n0}=50, F_{n1}=0	F_{n0}=0, F_{n1}=0	F_{n0}=100, F_{n1}=0

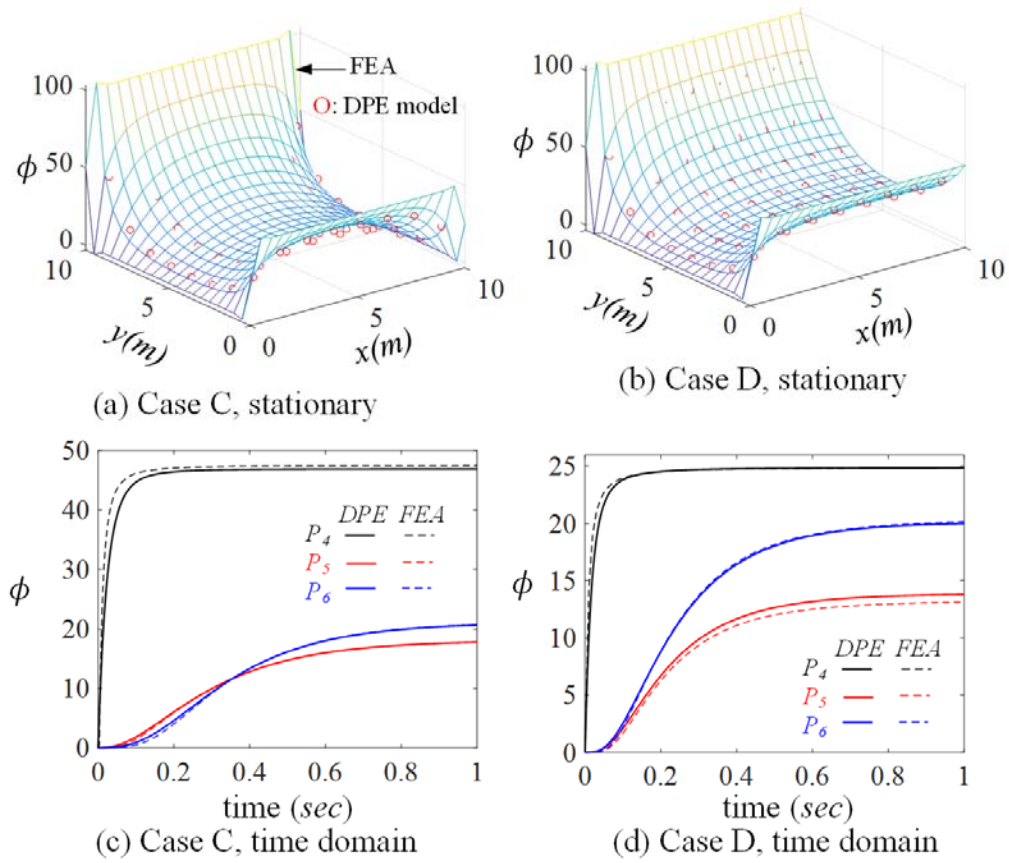

Figure 3-5 Three-dimension simulation results

3.1.6 Quadrilateral Shape

Figure 3-6(a), (b) are the geometries of the models for non-rectangle (quadrilateral) objects with right sides shift 2m and 4m in *y* direction. To validate the model for non-rectangle geometry objects, Fig. 3-6(c) is the simulation result of Fig. 3-6(a) geometry with parameters of Case A, and Fig. 3-6(d) is the simulation result of Fig. 3-6(b) geometry with parameters of Case B. The percentage errors are 0.555% and 0.854% respectively.

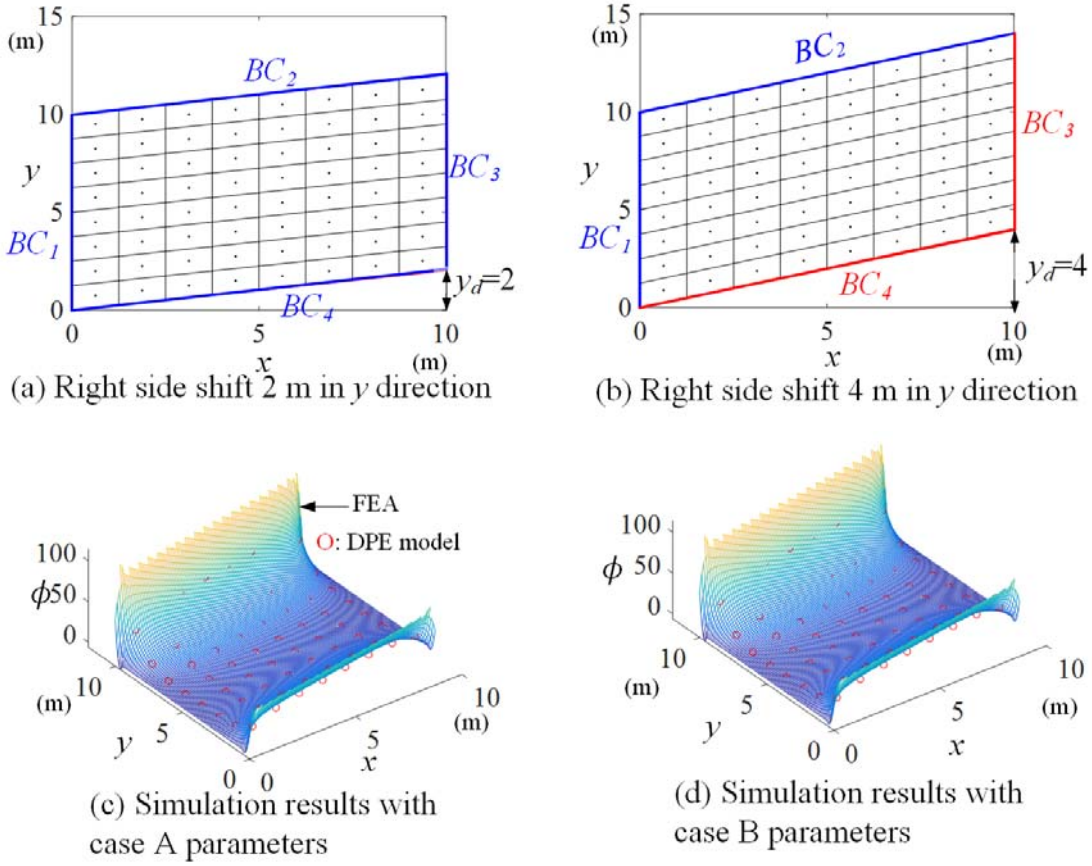

Figure 3-6 Three-dimension simulation results

3.1.7 Time-Dependent Electric Field

The stationary electric field is a kind of the scalar linear PDE, which is verified in the last sub-section. There is an additional term in the equation of time-dependent electric field. To verify it, the same geometry, mesh, and test points of last subsection are used. But, the unit of the geometry converts from m to mm. For the 2D electric field, figure 3-7(a) compares the simulation results of the DPE method of time domain electric field Eq. (3.10b) with the FEA software with the boundary conditions of Case B and σ=1(S/m), ε_r=10^6, ε_r=10^7. Figure 3-7(b) compares the simulation results with the boundary conditions of Case C and σ=1(S/m), ε_r=10^6, ε_r=10^7. The time interval of the simulation is 0.01 ms.

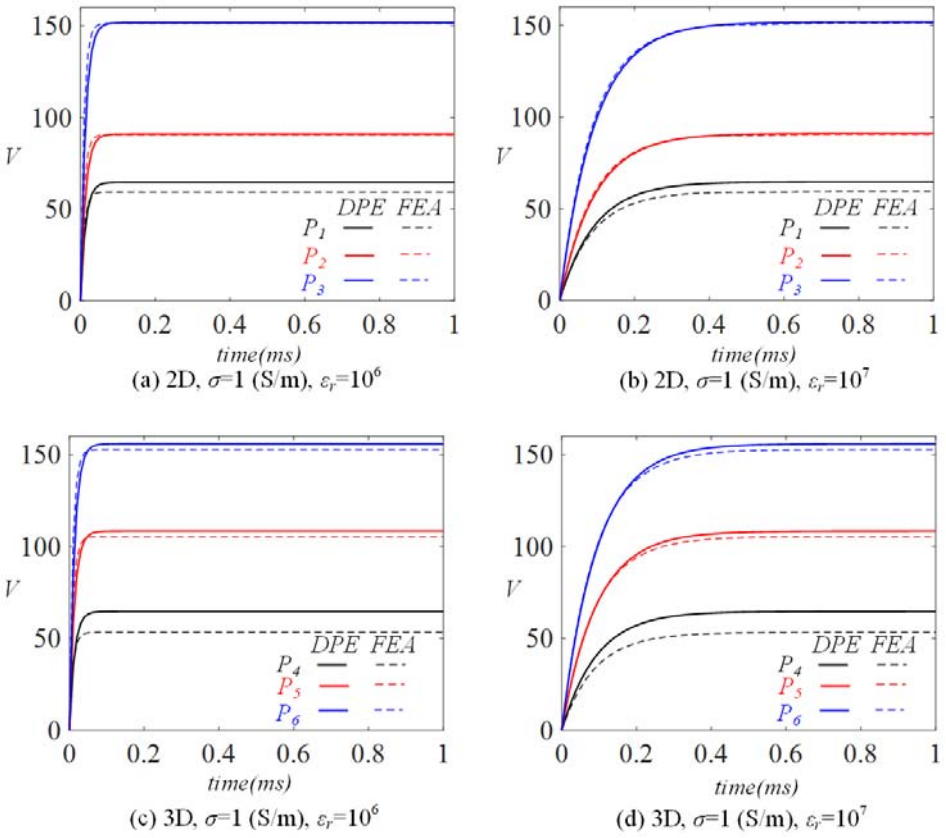

Figure 3-7 Time domain simulation results

3.2 Vector Potential Magnetic/Eddy-Current Field in Non-Ferrous Metal

The basic concept of DPE method for modeling a magnetic field is to divide the object of interest into many elements. Each conductor is a current source for mutual inductance and model the magnetic/eddy-current (M/EC) field of the exciting objects or space in state-space representation. The order of the magnetic field dependents on the material property. In the case of non-ferrous metal, the permittivity is very small and can be neglected. The formulation of the M/EC field is the first order system. In the case of the biological tissue, the permittivity is large and needs to be considered. The formulation of the M/EC field is second order system.

Figure 3-8 illustrates a typical eddy-current-density (ECD) sensor for geometrical measurements, and the parameters involved in its modeling. The conductor (and hence $\mathbf{r}_i$) is fixed relative to the EM; hence, the eddy-current (EC) is induced solely by a time-varying current flowing through the EM winding. In Fig. 3-8(a), the *xyz* coordinate frame is at the geometrical center of the EM with its Z-axis pointing away from the conductor along the axis. In the following discussion, the EM coil is assumed to consist of N_w turns wire (diameter d_w) through which an input current $I(t)$ flows with density $J(t)$ given in Eq. (3.10) where C_E accounts for the fact that the current only passes through the circular wires:

$$J_0(t) = \frac{C_E}{a_o a} I(t) \quad \text{where } C_E = \frac{\pi}{\rho_a}\left[\frac{N_w D_w}{4(1-\rho_i)}\right]^2 \text{ and } D_w = \frac{d_w}{a_o} \tag{3.10a}$$

$$\rho_i = \frac{a_i}{a_o};\ \rho_a = \frac{a}{a_o};\ H = \frac{h}{a};\ Z = \frac{z}{a} \text{ and } R = \frac{r}{a_o} \tag{3.10b~f}$$

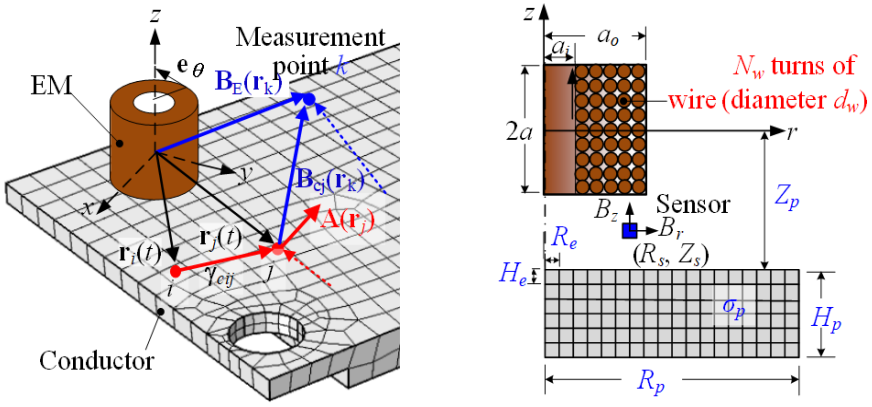

(a) Conductor and EM in *xyz* coordinates (b) 2D cylindrical coordinates

Figure 3-8 Schematics showing variables/parameters used in modeling

The induced ECD (denoted as $\mathbf{J}(\in \mathbb{R}^{3\times 1}) = \mathbf{J}_E + \mathbf{J}_C$) is contributed by the time-varying magnetic fields of the EM and by the Conductor elements respectively, and can be

explicitly expressed in terms of a geometry-dependent magnetic vector potential using Eq. (B.3b) in Appendix. For the EM through which a uniform current density $J_E(t)$ flows,

$$\mathbf{J}_{\mathbf{E}}(\mathbf{r}',t) = J_E(t)\mathbf{e}_\theta \text{ where } \mathbf{e}_\theta = -\sin\theta\mathbf{e}_x + \cos\theta\mathbf{e}_y \tag{3.11}$$

Using (B.2b) with $\frac{\mathbf{r}_j}{a_o} = \begin{bmatrix} R_j\cos\theta_j & R_j\sin\theta_j & \rho_a Z_j \end{bmatrix}^{\mathrm{T}}$

$$a_o^2\boldsymbol{\varphi}_E(\mathbf{r}_j,t) = \mu_o\boldsymbol{\gamma}_{\mathbf{E}}(\mathbf{r}_j)J_E(t) \tag{3.12}$$

Where $\boldsymbol{\varphi}_{\mathbf{E}}(\mathbf{r}_j, t)$ is the magnetic vector potential generated by the EM at $\mathbf{r}_j$ position and time t. In Eq. (3.12), $\boldsymbol{\gamma}_{\mathbf{E}}(\mathbf{r}_j)$ depends on the winding geometry for a stationary EM (Fig. 3-8b):

$$\boldsymbol{\gamma}_{\mathbf{E}}(\mathbf{r}_j) = aa_o\left(\frac{1}{4\pi}\int_{\theta=0}^{2\pi}\int_{Z=-1}^{1}\int_{R=\rho_i}^{1}\frac{\mathbf{e}_\theta}{|\mathbf{r}_j-\mathbf{r}'|/a_o}R\,dR\,dZ\,d\theta\right) \tag{3.13}$$

where $\frac{\mathbf{r}'}{a_o} = \begin{bmatrix} R\cos\theta & R\sin\theta & \rho_a Z \end{bmatrix}^{\mathrm{T}}$

For deriving practical ECD solutions, the conductor is decomposed into n_v hexahedron elements with their locations denoted by a displacement vector $\mathbf{r}_i(t)$ where i=1, 2, …, n_v. Each of the i^{th} element (volume v_i) is treated as an EC source with uniform density $\mathbf{J}_i$, electrical conductivity σ_i, and volume v_i. Using the distributed current source (DCS) method [16], the magnetic vector potential $\boldsymbol{\varphi}_C(\mathbf{r}_j)$ at location j can be similarly computed from the sum of the individual magnetic potential vectors contributed by the n_v elemental ECD sources $\mathbf{j}_i$ of the i^{th} conductor element:

$$a_o^2\boldsymbol{\varphi}_c(r_j) = \mu_o\sum_{i=1}^{nv}\left(\gamma_{cji}v_i\right)\mathbf{j}_i \tag{3.14}$$

The modified kernel function γ_{cij} in Eq. (3.14), which accounts for the errors of the magnetic field computed around the current source with boundary r_{bi} [16] is given by Eq. (3.15):

$$\gamma_{cij} \approx \frac{1}{4\pi}\begin{cases} 1/r_{ij} & i \neq j \\ \left(3r_{bi}^2 - r_{ij}^2\right)/\left(2r_{bi}^3\right) & i = j \end{cases} \quad \text{where } r_{ij} = \left|\mathbf{r}_j - \mathbf{r}_i\right|. \tag{3.15}$$

Using Eq. (3.13) and Eq. (3.15), which solve for the ECD induced by the EM and mutual inductances of the conductor, along Eq. (B.3b), the ECD source $\mathbf{j}_j$ in the j^{th} conductor element can be expressed in terms of the input current density J_E:

$$-\mathbf{j}_j = \mu_o \sigma_j \sum_{i=1}^{nv}\left(\gamma_{cji} v_i \frac{d\mathbf{j}_i}{dt}\right) + \mu_o \sigma_j \boldsymbol{\gamma}_{\mathbf{E}j} \frac{dJ_E}{dt} \tag{3.16}$$

With $\mathbf{J}_\ell = \left[j_{\ell 1} \quad \cdots \quad j_{\ell i} \quad \cdots \quad j_{\ell n}\right]^{\mathrm{T}}, \ell = x, y, z$ is defined as the state vector of the ℓ component ECD. $j_{\ell i}$ is the ℓ component ECD of the i^{th} element and $\dot{J}_E$ as an input. Eq. (3.17) can be rewritten in state-space representation:

$$\dot{\mathbf{J}}_\ell = \left[\boldsymbol{\alpha}_f\right]\mathbf{J}_\ell + \left[\boldsymbol{\beta}_f\right]\dot{J}_E \tag{3.17}$$

where $\left[\boldsymbol{\alpha}_f\right] = -\left[\mathbf{A}_\mathbf{C}\right]^{-1}\left[\mathbf{S}\right]^{-1}; \left[\boldsymbol{\beta}_f\right] = -\left[\mathbf{A}_\mathbf{C}\right]^{-1}\left[\mathbf{A}_\mathbf{E}\right];$

$\left[\mathbf{A}_\mathbf{C}(i,j)\right] = v_j \gamma_{cij}(t) = v_j \gamma_{cji}(t); \left[\mathbf{A}_\mathbf{E}(t)\right] = \left[\boldsymbol{\gamma}_{\mathbf{E}1} \quad \cdots \quad \boldsymbol{\gamma}_{\mathbf{E}j} \quad \cdots \quad \boldsymbol{\gamma}_{\mathbf{E}n}\right]^{\mathrm{T}};$

and $\mathrm{a}_o^{-2}\left[\mathbf{S}\right] = diag\left(\mu_o\sigma_1 \cdots \quad \mu_o\sigma_j \cdots \quad \mu_o\sigma_n\right)$

The MFD at any point k in the neighborhood of the conductor, which is denoted as $\mathbf{B}(\mathbf{r}_k, t)$, is a combination of the MFDs contributed by the EM and the EC, $\mathbf{B}=\mathbf{B}_\mathrm{E}+\mathbf{B}_\mathrm{C}$ where $\mathbf{B}$ is directly measured, and $\mathbf{B}_\mathrm{E}$ is real and can be pre-calibrated. $\mathbf{B}(\mathbf{r}_k,t)$ can be expressed as the output equation Eq. (3.18) where the 1st and 2nd terms are the MFD at the k^{th} point

contributed by the current flowing through the stationary (and rigid) EM (Fig. 3-8b) and the conductor respectively:

$$\mathbf{B}(\mathbf{r}_k, t) - \mathbf{B}_\mathbf{E} = \frac{\mu_0}{4\pi}\left[\mathbf{J}_s(t)\right]\left[\mathbf{V}_s\right]\mathbf{R}_k\left(\mathbf{r}_k\right) \tag{3.18}$$

In Eq. (3.18), $\mathbf{B_E}$ is contributed by the current flowing through the EM (Fig. 3-8b):

$$\mathbf{B}_\mathbf{E} = \boldsymbol{\eta}_\mathbf{E}\left(\mathbf{r}_k\right) J_E(t) \tag{3.19}$$

where $\boldsymbol{\eta}_\mathrm{E}(\mathbf{r}_k)$ depends on the winding geometry

$$\boldsymbol{\eta}_\mathbf{E}(\mathbf{r}_k) = a\left(\frac{\mu_o}{4\pi}\int_{\theta=0}^{2\pi}\int_{Z=-1}^{1}\int_{R=\rho_i}^{1}\frac{\mathbf{e_\theta}\times(\mathbf{r}_k - \mathbf{r'})}{\left|\mathbf{r}_k - \mathbf{r'}\right|^3} R\,dR\,dZ\,d\theta\right) \tag{3.20}$$

The term on the right side of Eq. (3.18) accounts for the mutual inductance of among the conductor elements, where

$$\left[\mathbf{J_S}(t)\right] = \left[skew\left(\mathbf{J_1}(t)\right)\cdots \quad skew\left(\mathbf{J}_i(t)\right)\cdots \quad skew\left(\mathbf{J}_{nv}(t)\right)\right]; \tag{3.21a}$$

$$\left[\mathbf{V_S}\right] = diag\left(v_1\mathbf{I} \quad \cdots \quad v_i\mathbf{I} \quad \cdots \quad v_{nv}\mathbf{I}\right); \tag{3.21b}$$

$$\mathbf{R}_k = \left[\mathbf{r}_{1k}^\mathrm{T}/r_{1k}^3 \quad \cdots \quad \mathbf{r}_{ik}^\mathrm{T}/r_{ik}^3 \quad \cdots \quad \mathbf{r}_{nk}^\mathrm{T}/r_{nk}^3\right]^\mathrm{T}. \tag{3.21c}$$

$$\text{and } skew(\mathbf{J_i}) = \begin{bmatrix} 0 & -J_{iz} & J_{iy} \\ J_{iz} & 0 & -J_{ix} \\ -J_{iy} & J_{ix} & 0 \end{bmatrix} \tag{3.21d}$$

In state-space representation, Eq. (3.17) and Eq. (3.18) are the state and output equations of the EM/Conductor system (Fig. 3-8) respectively. Equations (3.17) and (3.18) are presented in full forms for establishing a relatively complete state-space formulation with accurate solutions for future benchmark comparison. Once understood, approximated closed-form solutions could be used for real-time computing.

3.2.1 *Constraint Imposed on the Governing Equations of ECD*

To obtain solutions that uniquely describe the system (Fig. 3-8), Eq. (3.17) must satisfy the principle of conservation of charge, and account for the physically meaningful boundary conditions. For simplicity in illustration, Fig. 3-9(a) shows a hexahedron element is characterized by three orthogonal vectors $\mathbf{u}_\ell$ and six surfaces $s_{\ell\pm}$ and their normal $\mathbf{n}_{\ell\pm}$ where the subscript "±"indicates the "+" or "–" side along the ℓ=*x*, *y*, or *z* axis. The surface areas and surface-normal vectors of the i^{th} element can be mathematically written as Eq. (3.22a~f):

$$s_{ix\pm}=\left|\mathbf{u}_{iy+}\times\mathbf{u}_{iz\pm}\right|;\ s_{iy\pm}=\left|\mathbf{u}_{iz+}\times\mathbf{u}_{ix\pm}\right|;s_{iz\pm}=\left|\mathbf{u}_{ix+}\times\mathbf{u}_{iy\pm}\right| \qquad (3.22a\sim c)$$

$$\mathbf{n}_{ix\pm}=\frac{\mathbf{u}_{iy+}\times\mathbf{u}_{iz\pm}}{s_{ix\pm}};\ \mathbf{n}_{iy\pm}=\frac{\mathbf{u}_{iz+}\times\mathbf{u}_{ix\pm}}{s_{iy\pm}};\ \mathbf{n}_{iz\pm}=\frac{\mathbf{u}_{ix+}\times\mathbf{u}_{iy\pm}}{s_{iz\pm}}. \qquad (3.22d\sim f)$$

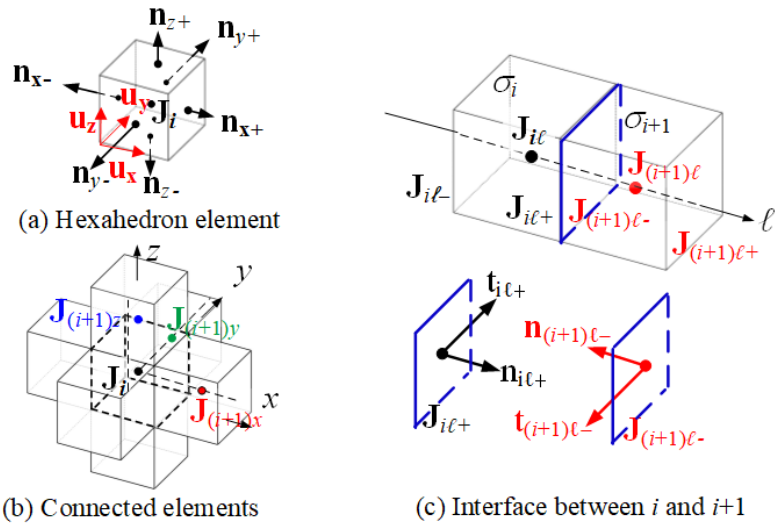

Figure 3-9 Schematics illustrating the symbols for describing constraints

Conservation law

The steady ECD must satisfy the continuity equation, $\nabla \cdot \mathbf{J} = 0$ can be written in integral form using the divergence theorem to satisfy the conservation law for a hexahedron element. Numerically, the algebraic sum of the outward-flowing eddy-current of the i^{th} element is zero:

$$\sum_{k=1}^{6} s_k \left(\mathbf{J}_{ik} \bullet \mathbf{n}_k \right) = 0 \tag{3.23}$$

In Eq. (3.24), the subscript k (=1, …6) corresponds to the surfaces ($x+$, $x-$, $y+$, $y-$, $z+$, $z-$); s_k and $\mathbf{n}_k$ are defined in Eq. (3.22a-f). For computing Eq. (3.23), the ECD $\mathbf{J}_{ik}$ at the six surfaces (Fig. 3-9(b)) can be computed using the forward finite-difference:

$$\mathbf{J}_{i\ell-} = \mathbf{J}_i \text{ and } \mathbf{J}_{i\ell+} = \mathbf{J}_{(i+1)\ell} \tag{3.24a,b}$$

Boundary conditions

When the ECD obliquely crosses an interface between two media with different conductivities, the ECD vector changes both in direction and in magnitude. The steady ECD is divergence-less and curl-free and thus satisfies two conditions; 1) the normal component **n** of a divergenceless vector field is continuous; and 2) the tangential component **t** of a curl-free vector field is continuous across an interface. With the aid of Fig. 3-9(c), they are given in (3.25a) and (3.25b) respectively:

$$\mathbf{J}_{i\ell+} \bullet \mathbf{n}_{i\ell+} = \mathbf{J}_{(i+1)\ell-} \bullet \mathbf{n}_{(i+1)\ell-} \tag{3.25a}$$

$$\sigma_{i\ell+} \left(\mathbf{J}_{(i+1)\ell-} \bullet \mathbf{t}_{(i+1)\ell-} \right) = \sigma_{(i+1)\ell-} \left(\mathbf{J}_{i\ell+} \bullet \mathbf{t}_{i\ell+} \right) \tag{3.25b}$$

where $\mathbf{n}_\ell + \mathbf{t}_\ell = \mathbf{1}$.

Thus, the constraint matrix [**Q**] consists of [$\mathbf{Q_C}$] accounting for the conservation law and ([$\mathbf{Q_{B}}_n$], [$\mathbf{Q_{B}}_t$]) for the constraints imposed on the boundary surfaces in the (normal, tangential) directions respectively. For n_v elements with a total of n_b boundary surfaces,

$$[\mathbf{Q}]\left(\in \mathbb{R}^{(nv+2nb)\times 3nb}\right)=\left[\left[\mathbf{Q_C}\right]^{\mathrm{T}} \quad \left[\mathbf{Q_{B}}_n\right]^{T} \quad \left[\mathbf{Q_{B}}_t\right]^{\mathrm{T}}\right]^{\mathrm{T}} \tag{3.26}$$

$$\text{where } \left[\mathbf{Q_C}\right]\in \mathbb{R}^{nv\times 3nv},\ \left[\mathbf{Q_{B}}_n\right]\in \mathbb{R}^{nb\times 3nv} \text{ and } \left[\mathbf{Q_{B}}_t\right]\in \mathbb{R}^{nb\times 3nv}$$

To facilitate implementation, the elements in the i^{th} row of the constraint matrices ([$\mathbf{Q_C}$], [$\mathbf{Q_{B}}_n$], [$\mathbf{Q_{B}}_t$]) are given in Eq. (3.27a~c) using the selection vector $\mathbf{b}_{ik\ell}$ define in Eq. (3.27d) where the subscripts k and ℓ refer to the six surfaces and three axes of the i^{th} element:

$$\mathbf{Q}_{Ci}(\in \mathbb{R}^{1\times 3nv})=\sum_{k=1}^{6} s_{ik} \sum_{\ell=x,y,z} n_{ik\ell}\mathbf{b}_{ik\ell} \tag{3.27a}$$

$$\mathbf{Q}_{Bni}=\sum_{\ell=x,y,z}\left[n_{i\ell+}\mathbf{b}_{i\ell+}-n_{(i+1)\ell-}\mathbf{b}_{(i+1)\ell-}\right] \tag{3.27b}$$

$$\mathbf{Q}_{Bti}=\sum_{\ell=x,y,z}\left[2\Delta_{i\ell+}^{-2}t_{(i+1)\ell-}\mathbf{b}_{(i+1)\ell-}-\Delta_{(i+1)\ell-}^{-2}t_{i\ell+}\mathbf{b}_{i\ell+}\right] \tag{3.27c}$$

$$\mathbf{b}_{ik\ell}\left(\in \mathbb{R}^{1\times 3nv}\right)=\begin{cases}1 & \text{at } k \text{ surface along } \ell \text{ axis}\\ 0 & \text{else}\end{cases} \tag{3.27d}$$

A surface is defined as a boundary surface if it belongs only to a hexahedron element or an inner surface if it belongs to two hexahedron elements. Each element takes a row of [$\mathbf{Q_C}$] and each boundary surface takes one row of [$\mathbf{Q_{B}}_n$] and [$\mathbf{Q_{B}}_t$].

3.2.2 Harmonic Solutions to the ECD and its Generated MFD

When a sinusoidal current density $J_E(t)=J_o e^{j\omega t}$ flows through an annular electromagnet (EM) which generates a magnetic flux density (MFD), the steady state ECD

$\mathbf{J}e^{j\omega t}$ (where $\mathbf{J}=\mathbf{J}_{\mathrm{Re}}+j\mathbf{J}_{\mathrm{Im}}$ with the subscripts "Re" and "Im" denoting the real and imaginary parts respectively) is induced in the non-ferrous electric conductive plate placed below the EM. J_0 is the current density of the EM, which can be determined by Eq. (3.10a). For a harmonic input $I_o e^{j\omega t}$, the time derivatives of the input current density and induced ECD are $\left(\dot{J}_E,\dot{\mathbf{J}}\right)=j\omega\left(J_E,\mathbf{J}\right)$ and ω is the angular frequency. The (Re, Im) parts of the $\ell(=x, y, z)$ components, $\left(\mathbf{J}_{\ell\mathrm{Re}},\mathbf{J}_{\ell\mathrm{Im}}\in\mathbb{R}^{n_v\times 1}\right)$ can be solved from Eq. (3.17) in terms the skin-depth δ normalized to the outer radius a_o of the EM as shown in Eq. (3.28) where the subscript j is the element number to account for any material variation within the non-ferrous metal (with the relative magnetic permeability μ_r equal to 1):

$$\Delta_j=\frac{\delta_j}{a_o}\ \text{where}\ \ \delta_j=\sqrt{\frac{2}{\omega\sigma_j\mu_o\mu_r}} \tag{3.28}$$

In Eq. (3.28), σ_j is the electrical conductivity and μ_o ($=4\pi\times10^{-7}$H/m) is the magnetic permeability of free space. The steady-state harmonic solutions to Eq. (3.17) are given by Eq. (3.29a,b) in terms of a normalized skin-depth (introduced here to derive a unified solution independent of materials):

$$\mathbf{J}_{\ell\mathrm{Re}}=\left[\overline{\mathbf{S}}\right]\left[\mathbf{A}_{\mathbf{C}}\right]\mathbf{J}_{\ell\mathrm{Im}} \tag{3.29a}$$

$$\text{where}\ \left[\overline{\mathbf{S}}\right]=diag\left(2\Delta_1^{-2}\cdots\ \ 2\Delta_j^{-2}\ \ \cdots 2\Delta_n^{-2}\right)$$

$$\mathbf{J}_{\ell\mathrm{Im}}=\mathbf{E}_\ell J_E \tag{3.29b}$$

$$\text{where}\mathbf{E}_\ell=-\left[\mathbf{I}+\left(\left[\overline{\mathbf{S}}\right]\left[\mathbf{A}_C\right]\right)^2\right]^{-1}\left(\left[\overline{\mathbf{S}}\right]\left[\mathbf{A}_{E\ell}\right]\right).$$

The ECD in the conductive plate is formulated as a two-step constrained least-square (CLS) problem: The first CLS solves Eq. (3.29b) for $\mathbf{J}_{\mathrm{Im}}=\left[\mathbf{J}_{x\mathrm{Im}}^{\mathrm{T}} \quad \mathbf{J}_{y\mathrm{Im}}^{\mathrm{T}} \quad \mathbf{J}_{z\mathrm{Im}}^{\mathrm{T}}\right]^{\mathrm{T}}$ by minimizing

$$\sum_{\ell=x,y,z}\left\|\mathbf{J}_{\ell\mathrm{Im}}-\mathbf{E}_{\ell}J_{E}\right\|^{2} \qquad \text{subject to } [\mathbf{Q}]\mathbf{J}_{\mathrm{Im}}=0 \tag{3.30}$$

With $\mathbf{J_I}$, the second CLS solves Eq. (3.29a) for $\mathbf{J}_{\mathrm{Re}}=\left[\mathbf{J}_{x\mathrm{Re}}^{\mathrm{T}} \quad \mathbf{J}_{y\mathrm{Re}}^{\mathrm{T}} \quad \mathbf{J}_{z\mathrm{Re}}^{\mathrm{T}}\right]^{\mathrm{T}}$ by minimizing

$$\sum_{\ell=x,y,z}\left\|\mathbf{J}_{\ell\mathrm{Re}}-\left[\overline{\mathbf{S}}\right]\left[\mathbf{A}_{\mathbf{C}}\right]\mathbf{J}_{\ell\mathrm{Im}}\right\|^{2} \qquad \text{subject to } [\mathbf{Q}]\mathbf{J}_{\mathrm{Re}}=0 \tag{3.31}$$

In Eq. (3.30) and Eq. (3.31), $\ell=x,y,z$ and $\mathbf{J}_{\ell\mathrm{Re}},\mathbf{J}_{\ell\mathrm{Im}}\in\mathbb{R}^{nv\times 1}$.

The measured MFD at any point *k* in the neighborhood of the conductor, which is denoted as $\mathbf{B}(\mathbf{r}_k,t)=\left[\mathbf{B}_{\mathrm{Re}} \quad \mathbf{B}_{\mathrm{Im}}\right]^{\mathrm{T}}$, where $\mathbf{B}_{\mathrm{Re}},\mathbf{B}_{\mathrm{Im}}$ are combinations of MFDs. $\mathbf{B}_E$ generates from the EM, and can be pre-calibrated. The output equation Eq. (3.18) can be computed from Eq. (3.32) where $\left[\mathbf{J}_{\mathbf{S}\mathrm{Re}}\right]$ and $\left[\mathbf{J}_{\mathbf{S}\mathrm{Im}}\right]$ are the real and imaginary parts of $\mathbf{J_S}$ Eq. (3.21a):

$$\begin{bmatrix}\mathbf{B}_{\mathrm{Re}}-\mathbf{B}_{\mathbf{E}}\\ \mathbf{B}_{\mathrm{Im}}\end{bmatrix}=\frac{\mu_o}{4\pi}\begin{bmatrix}\left[\mathbf{J}_{\mathbf{S}\mathrm{Re}}\right]\left[\mathbf{V}_{\mathbf{s}}\right]\mathbf{R}_k\left(\mathbf{r}_k\right)\\ \left[\mathbf{J}_{\mathbf{S}\mathrm{Im}}\right]\left[\mathbf{V}_{\mathbf{s}}\right]\mathbf{R}_k\left(\mathbf{r}_k\right)\end{bmatrix} \tag{3.32}$$

3.2.3 2D Axial-Symmetrical Coordinate

The DCS method and its physical insights for modeling an EM-induced ECD field are best illustrated numerically and verified by comparing with published 2D analytical solutions [5] for a coil above a semi-infinite conducting slab and FEA-simulated results. For an axisymmetric configuration where the magnetic vector potential and induced ECD

only exist in the tangential direction, the conservation law Eq. (3.27a) and boundary constraints Eq. (3.27b-d) are automatically satisfied. The ECD solutions Eq. (3.17) reduce to 2D, where v_j is replaced by an elemental area c_j; and the modified kernel function γ_{cij} that accounts for the 2D simplification is given by

$$\gamma_{cij} = \frac{1}{4\pi}\int_0^{2\pi} \frac{\cos\theta}{f(\theta)} d\theta \text{ where } f(\theta) = \begin{cases} 2\left(R - \cos\theta\right) & i = j \\ \left|\mathbf{r}_j - \mathbf{r}'\right| / a_o & i \neq j \end{cases} \tag{3.33}$$

Three sets of numerical investigations were performed. The *first* set simulates the skin-depth effect on flexible grid division that refines the grid distribution based on equal current densities. The *second* set investigates the boundary effects on the computed ECD field where the analytical (2D axisymmetric) solutions [5] provide a basis for comparison. The *third* numerically evaluates the DPE method and its effectiveness (computational efficiency and accuracy) by comparing results with FEA in both 2D and 3D.

3.2.4 Flexible Grid Division based on Equal Current

Without loss of generality, an axisymmetric configuration is used as an example in Fig. 3-10 to illustrate a grid refinement method that takes into account the skin-depth effect on the ECD solutions. The method resizes the divisions such that all the elements have equalized current density as compared in Figs. 3-10(a) and 3-10(d), which show the initially uniform and refined grids respectively. The method is illustrated in Figs. 3-10(b) and 3-10(c), where the probability density function (PDF) is defined as the summation of the ECDs along the depth for a specific radius or the radius for a pre-determined depth; and the cumulative distribution function (CDF) is the accumulated PDF in corresponding

direction. Fig. 3-10(b) plots the PDF and its corresponding CDF of the ECD magnitude normalized to its maximum magnitude ($|J|/J_{Max}$) in the radial direction. Similarly, Fig. 3-10(c) plots the PDF and CDF but in the Z direction. The refined (R, Z) grid lines on the conductor (Fig. 3-10(d)) represent an even distribution of the ECD magnitudes along the (R,Z) directions, which can be obtained through the projection of the equalized divided current-densities on the CDF(R) and CDF(Z) as illustrated in Figs. 3-10(b) and 3-10(c).

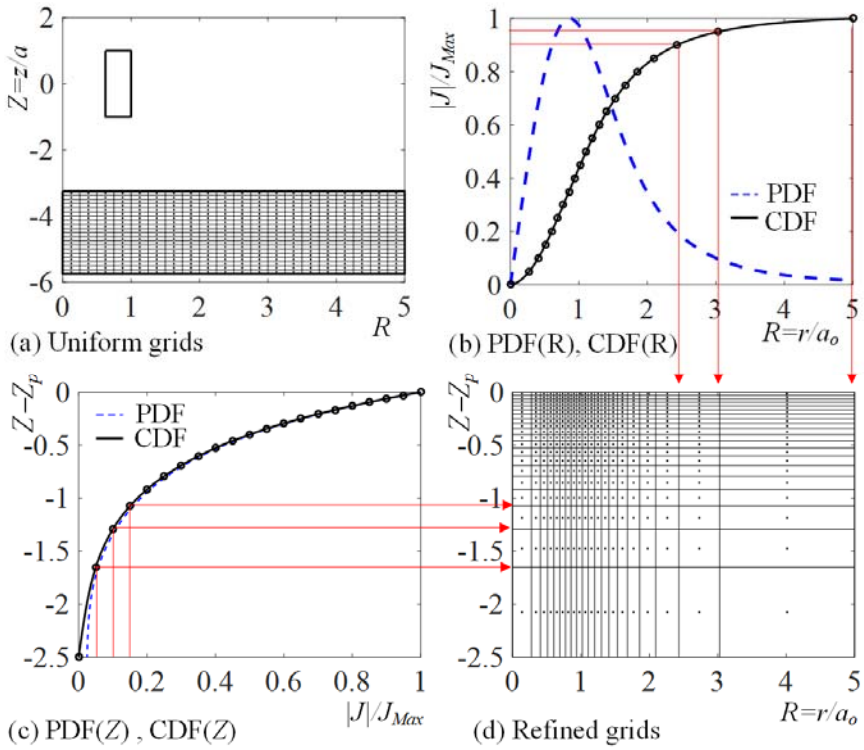

Figure 3-10 Grid refinement method

3.2.5 Real-Time Computation of Magnetic Vector Potential

The solutions to the MVP **A**, induced EC **J** and MFD measurement $\mathbf{B}(\mathbf{r}_k,t)$ require computing two volume integrals, $\boldsymbol{\gamma}_E$ and $\boldsymbol{\eta}_E$ in Eq. (3.13) and Eq. (3.20) respectively. Once the configuration is given, $\boldsymbol{\eta}_E$ (that requires a single computation for each sensor

measurement) can be pre-computed off-line but γ_E must be computed for each of the n_v conductor elements. For real-time applications, it is desired that γ_E can be solved in closed-form; and thus Eq. (3.14) is approximated by Eq. (3.34) as a product of two integrals as illustrated in Eq. (3.35a, b) where $\rho_r = (1+\rho_i)/2$:

$$\frac{\gamma_{\mathbf{E}}\left(R_j, \mathrm{Z}_j, \theta\right)}{\gamma_o} \approx \left(\gamma_{rz}\big|_{\theta=0}\right)\left(\gamma_{\theta}\big|_{R_j}\right) \tag{3.34}$$

where

$$\gamma_{R,Z}\big|_{\theta=0} = \int_{Z=-1}^{1}\int_{R=\rho_i}^{1} \frac{R\,dR\,dZ}{\sqrt{\left(R-R_j\right)^2 + \rho_a^2(\mathrm{Z}-Z_j)^2}} \tag{3.35a}$$

$$\gamma_{\theta}\big|_{R_j,\mathrm{Z}_j} = \int_{0}^{2\pi} \frac{\sqrt{\left(\rho_r - R_j\right)^2 + Z_j^2}\cos\theta d\theta}{\sqrt{\left(\rho_r\cos\theta - R_j\right)^2 + \rho_r^2\sin^2\theta + Z_j^2}} \tag{3.35b}$$

The physical intuition of Eq. (3.35) as follows: The 1st part is essentially Eq. (3.14) with $\theta = 0^\circ$, which evaluates an integral over an EM cross-section in the *r-z* plane. The 2nd part integrates over θ as the cross-section (at $\theta = 0^\circ$) rotates. As shown in (3.35b), the 2nd integral accounts for the distance between the center of the rotated cross-section and the conductor element being considered. For the geometrical configuration in Fig. 3-8(b), the closed-form solutions to the two integrals (γ_{rz} and γ_θ) are derived in (3.36) and (3.37) respectively where K_- and K_+ are the elliptic equations of 1st and 2nd kinds respectively:

$$\gamma_{rz}\big|_{\theta=0}=\frac{1}{2}\begin{bmatrix}\left(1-Z_j\right)\left(F_{o-}-F_{i-}\right)+\left(1+Z_j\right)\left(F_{o+}-F_{i+}\right)+\\ \rho_a^{-1}\left(1-R_j^2\right)\log F_{zo}+\rho_a^{-1}\left(\rho_i^2-R_j^2\right)\log F_{zi}\\ +2R_j\left(1-Z_j\right)\log F_{ro-}+2R_j\left(1+Z_j\right)\log F_{ro+}\end{bmatrix};\tag{3.36}$$

where $F_{zo}=\dfrac{F_{o-}+\rho_a\left(1-Z_j\right)}{F_{o+}-\rho_a\left(1+Z_j\right)}$; $F_{o\pm}=\sqrt{\rho_a^2\left(1\pm Z_j\right)^2+\left(1-R_j\right)^2}$;

$F_{zi}=\dfrac{F_{i+}-\rho_a\left(1+Z_j\right)}{F_{i-}+\rho_a\left(1-Z_j\right)}$; $F_{i\mp}=\sqrt{\rho_a^2\left(1\mp Z_j\right)^2+\left(\rho_i-R_j\right)^2}$; and $F_{ro\pm}=\dfrac{F_{o\pm}+\left(1-R_j\right)}{F_{j\pm}+\left(\rho_i-R_j\right)}$.

$$\gamma_{\theta}\big|_{r_j,z_j}=\frac{F_{r-}}{R_j\rho_r}\left[\left(\rho_r^2+R_j^2+\rho_a^2Z_j^2\right)\left(\frac{K_-\left(m_+\right)}{F_{r+}}+\frac{K_-\left(m_-\right)}{F_{r-}}\right)-F_{r+}K_+\left(m_+\right)-F_{r-}K_+\left(m_-\right)\right]\tag{3.37}$$

where $F_{r\mp}=\sqrt{\left(\rho_r\mp R_j\right)^2+\rho_a^2Z_j^2}$; $m_\pm=\pm4R_j\rho_r/F_{r\mp}^2$ *and* $K_\mp\left(m_\pm\right)=\int_0^{\pi/2}\left(1-m_\pm\sin^2\theta\right)^{\mp\frac{1}{2}}d\theta$

3.2.6 Numerical Verification

Axis-symmetric ECD distribution and boundary effects

Figure 3-11(a) shows the real and imaginary parts of the ECD fields induced in the circular plate (characterized by thickness H_p=2.5 and located at Z_p = 2.75 below the EM), which were numerically computed using Eq. (A.1) along the *R* direction at *Z* = –5. Figs. 3-11(b, c) graph the real and imaginary parts of the tangential ECD at different *R* and *Z* locations. The parametric values that characterize the EM and the normalized skin-depth Δ are given in the first row of Table 3-9.

Table 3-9 Simulation parametric values.

EM, Δ=0.7926	(a_o, a) = (6, 2) mm, ρ_i = 0.625; J_0 = 4.276 A/mm^2			
Method **Elements**	**DPE 2D** 360	**DPE 3D** 1,296	**FEA 2D** 2,630	**FEA 3D** 120,529
MFD (G) at **(**R_s=0, Z_s=4.5**)**	$\lvert B_r\rvert$=0 $\lvert B_z\rvert$=20.26	$\lvert B_x\rvert$=0.026 $\lvert B_y\rvert$=0.026 $\lvert B_z\rvert$=20.24	$B_r\rvert\approx$0.037 $\lvert B_z\rvert$=20.17	$\lvert B_x\rvert$=0.048 $\lvert B_y\rvert$=0.209 $\lvert B_z\rvert$=20.24

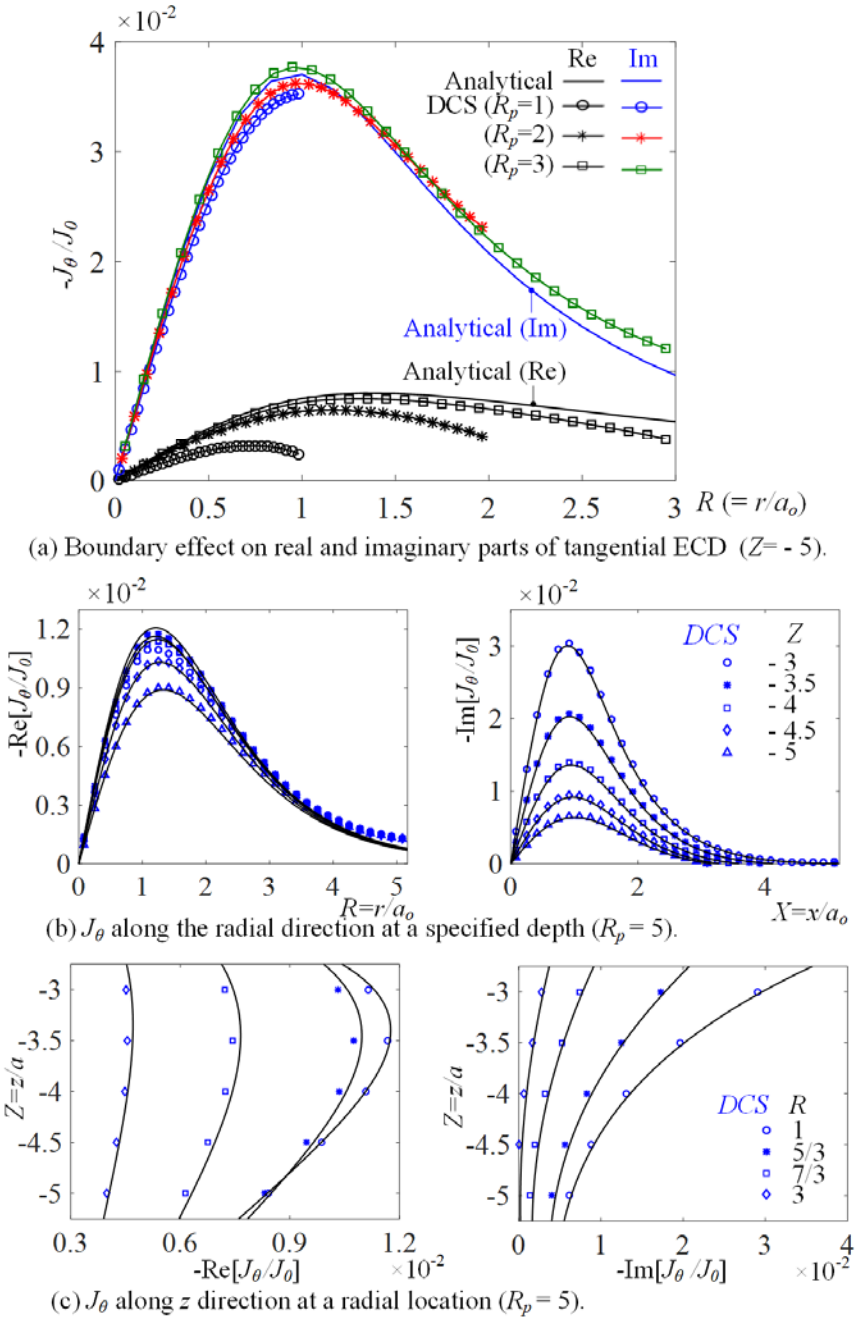

Figure 3-11 Tangential ECD fields. (H_p-2.5; Z_p = 2.75)

The boundary effects on the ECD models can be analyzed by investigating the effect of different radii on the computed tangential ECD; (R_p=r_p/a_o=1, 2 and 3) in Fig.

3-11(a) and (R_p = 5) in Fig. 3-11(b, c). In Fig. 3-11, the analytical solutions (solid-line curves) provide a basis for comparison. The model and the analytical solutions agree well for $R_p \geq 3$ but the discrepancy increases for smaller R_p as shown in Fig. 3-11(a). Unlike the 2D analytical solutions that yield a single pair of (real and imaginary) curves regardless of R_p, the model accounts for the boundary effects.

Computational effectiveness

The effectiveness (efficiency and accuracy) of the DCS model is numerically evaluated by comparing of the computed MFD of the induced ECD with results simulated by COMSOL (commercial FEA software) for a benchmark problem; both 2D and 3D FEA meshes are considered as shown in Figs. 3-12(a, b). FEA models mesh all domains assuming both the nonferrous metallic plate (σ=10^5~10^8 Sm^{-1}) and the air (σ=1 S m^{-1}) are conductive to compute the MFD due to the induced ECD. For the benchmark problem, an annular EM is perpendicular to a non-ferrous square (72×72 mm^2) plate with a MFD sensor placed along the coil axis ($x = y = 0$) but 1mm above the plate. Because of the symmetry, the MFD ($|B_x|$, $|B_y|$) components of the induced circular eddy-currents are theoretically equal to zero; this observation provides a rational means to verify the solutions and a means to determine an appropriate number of elements needed in the modeling method and FEA models. With the parametric values listed in Table 3-9, Figs. 3-12(c, d) plot the ECD-induced MFD at the sensor location (R_s=0, Z_s=-2.25) computed using different number of elements. Table 3-9 and Fig. 3-12 offer some intuitive insights into the modeling of the MFD generated by the induced ECD:

– Table 3-9 shows that all the model and FEA (2D or 3D) converge to a nearly identical $|B_z|$ value but the 2D $|B_r|$ or the 3D ($|B_x|$, $|B_y|$) components vary somewhat. As expected theoretically, the results show that $|B_r|$ of the 2D model is zero and that the ($|B_x|$, $|B_y|$) computed from the 3D model approaches zero as the number of elements increases (Fig. 3-12d). This validates both the 2D and 3D models.

– The large area or volume of air space in the FEA models results in significant "quantitation noise" observed simulated MFD; as a result, both the 2D and 3D FEA yield non-zero $|B_r|$ or ($|B_x|$, $|B_y|$). This theoretically explains why FEA needs more elements to converge, and exhibits larger fluctuations with the number of elements for all cases in Figs. 3-12(c, d). Unlike FEA models, the method (that uses point sources in direct modeling without the need to include the air space) results in more accurate but less variations in the MFD computation.

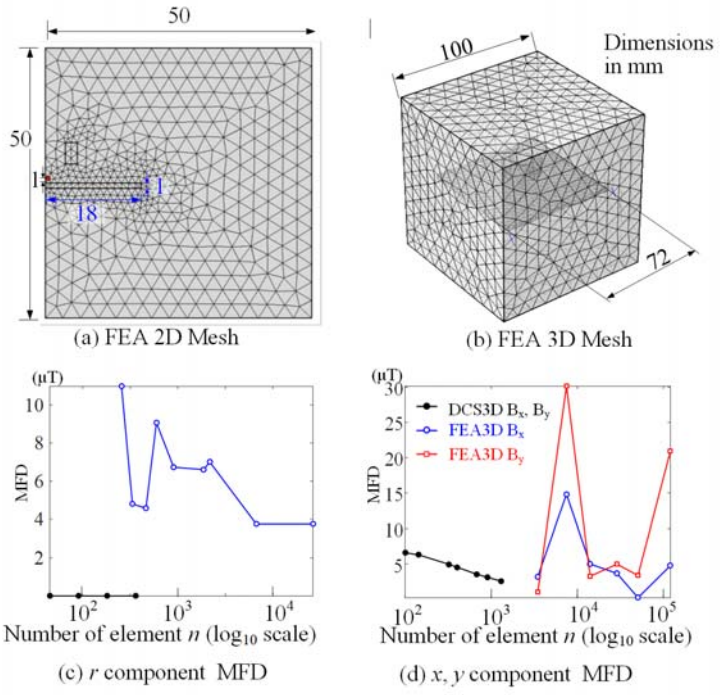

Figure 3-12 Performance evaluation.

– The modeling method solves a pair of CLS problems, where the number of elements (and hence the matrix sizes) represent a trade-off between its computational time and accuracy. Based on several n_v (= 2×2, 5×5, 10×10, 20×20, 30×30, and 40×40) elements, the computational time of the DCS modeling method is proportional to $(n_v)^{2.53}$. As a rule of thumb, the calculations with a PC (Intel Core *i*7-3630QM, 2.40GHz CPU, 16GB RAM, 64 bits OS) take about 14.1 seconds for a 20×20-element DPE model and 1 minutes for a 30×30-element model.

Flexible grid division based on equal current

To help visualize the effect of flexible grid division, Figs. 3-13(a~c) show the effects of the normalized skin-depth Δ and the plate-to-coil width aspect ratio $R_p(=r_p/a_o)$ on CDF(Z) and CDF(R). As shown in Figs. 3-13(a) where R_p=2, the ECD concentrates more on the surface with smaller Δ, and is relatively insensitive to Δ in the R direction. On the other hand, R_p has a significant influence on the CDF(R) but negligible effects on CDF(Z) as compared in Fig. 3-13(b) for a given =1; thus, the ECD distributes more uniformly with a smaller R_p but abruptly changes near the EM when R_p >5. The above parametric effects on the grid divisions can be visually seen in Fig. 3-13(c):

– The case (Δ=0.2, R_p=2) requires finer grids near the surface while uniform grids are sufficient for (Δ=1, R_p=2).
– *Similarly*, the case (Δ=1, R_p=20) requires finer grids below the EM but uniform along Z direction, whereas the case (Δ=0.2, R_p=20) requires both a much denser grids directly below the EM and near the surface.

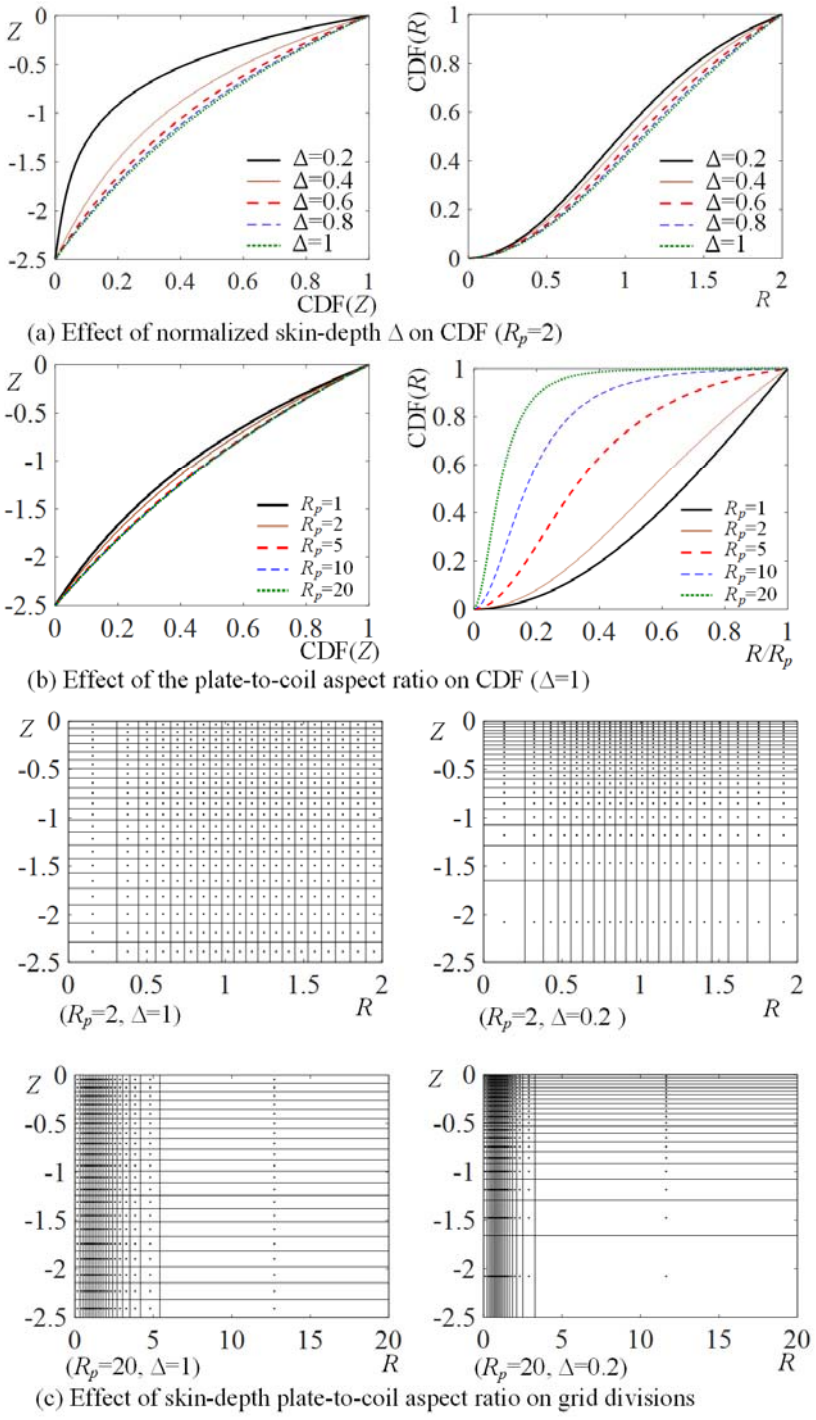

Figure 3-13 Parametric effects of grid divisions (H_p=2.5, Z_p=3.25)

Effects of approximate closed-form solutions for magnetic vector potential

Figure 3-14(a) compares the closed-form solution given by Eq. (3.35) for approximating φ_E (Eq. (3.12)) against the exact solution computed numerically based on the volume integral Eq. (3.13).

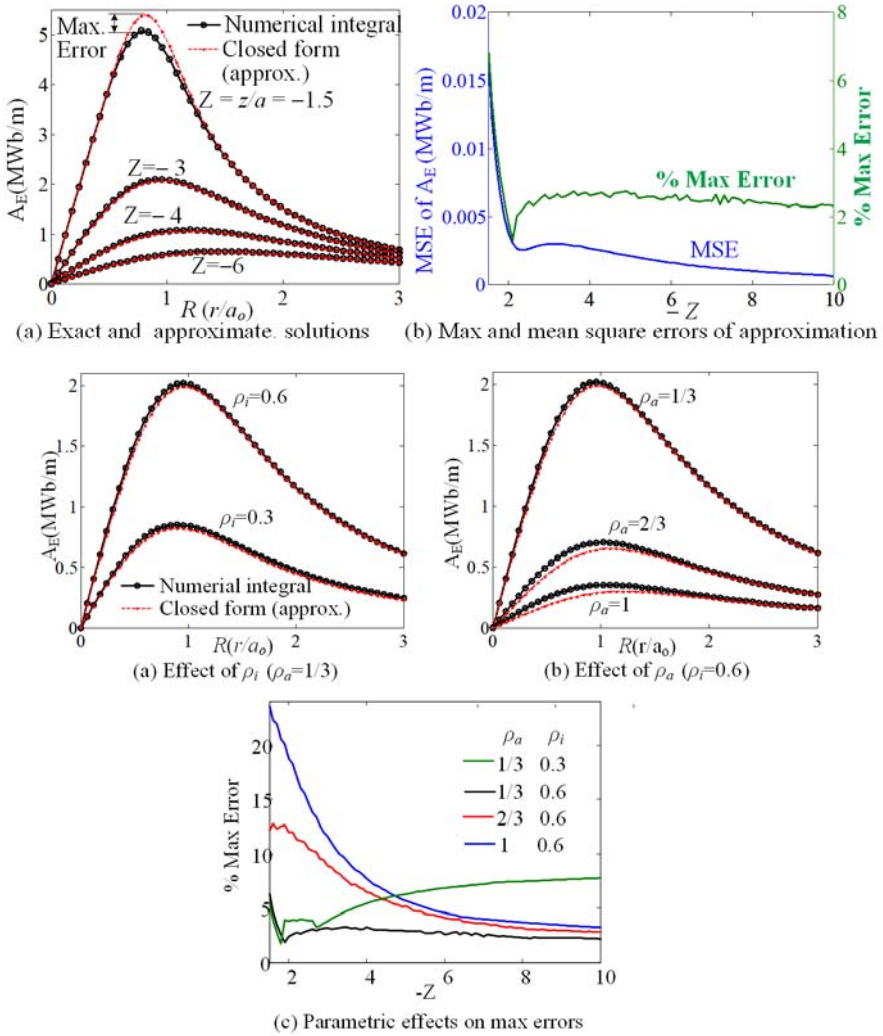

Figure 3-14 Parametric effects of grid divisions (H_p=2.5, Z_p=3.25)

When computing (3.36), the elliptic equations of 1st and 2nd kinds (K_- and K_+) were interpolated with table-lookup. The mean-square-error (MSE) and percentage (%) maximum error (that occurs at the peak) are plotted along the radial direction in Fig. 3-14(b). Fig. 3-14(c-e) shows the EM geometric effects on the approximate closed-form solutions.

3.3 Biological Tissue Eddy-Current Field

In the magnetic and eddy-current field formulation of the biological tissue, the displacement current needs to be considered. Eq. (B1.d), (B3.b) become Eq. (3.38a, b). ε is the permittivity, which equals to $\varepsilon_0\varepsilon_r$. ε_0 is the permittivity of vacuum, and ε_r is the relative permittivity. The Eddy-current $\mathbf{j}_j$ in the j^{th} conductor element can be expressed as a function of the current density J_E in Eq. (3.39).

$$\mathbf{J} = \sigma\mathbf{E} + \frac{\partial(\varepsilon\mathbf{E})}{\partial t}, \varepsilon = \varepsilon_0\varepsilon_r \quad (3.38a), \qquad \mathbf{J} = -(\sigma + \dot{\varepsilon})\frac{\partial \mathbf{A}}{\partial t} - \varepsilon\frac{\partial^2 \mathbf{A}}{\partial t^2} \tag{3.38b}$$

$$-\mathbf{j}_j = \left(\sigma_j + \dot{\varepsilon}_j + \varepsilon_j \frac{d}{dt}\right)\sum_i \left(\gamma_{cji} v_i \frac{d\mathbf{j}_i}{dt} + \boldsymbol{\gamma}_{\mathbf{E}j}\frac{dJ_E}{dt}\right) \tag{3.39}$$

The above (3.39) can be rewritten in matrix form reduces to (3.40):

$$-\mathbf{j}_j = \begin{bmatrix} v_1\gamma_{c1j} \cdots & v_i\gamma_{cij} \cdots & v_n\gamma_{cnj} \end{bmatrix}\left[\left(\sigma_j + \dot{\varepsilon}_j\right)\dot{\mathbf{J}} + \varepsilon_j\dot{\mathbf{K}}\right] + \begin{bmatrix}\left(\sigma_j + \dot{\varepsilon}_j\right) & \varepsilon_j\end{bmatrix}\boldsymbol{\gamma}_{\mathbf{E}j}\mathbf{u} \tag{3.40}$$

where $\mathbf{u} = \begin{bmatrix} \dot{J}_E & \ddot{J}_E \end{bmatrix}^{\mathrm{T}}$; $\mathbf{J} = \begin{bmatrix}\mathbf{j}_1 & \cdots & \mathbf{j}_i & \cdots & \mathbf{j}_{nv}\end{bmatrix}^{\mathrm{T}}$

$\mathbf{K} = \begin{bmatrix}\mathbf{k}_1 \cdots & \mathbf{k}_i \cdots & \mathbf{k}_{nv}\end{bmatrix}^{\mathrm{T}}$ and $\mathbf{k} = d\mathbf{j}/dt$.

Equation (3.40) can be written in state-space representation, where $\mathbf{Z}_\ell \left(\in \mathbb{R}^{2n_v \times 1}\right)$ is the ℓ component state vector, $\mathbf{U}\left(\in \mathbb{R}^{2n_v \times 1}\right)$ is the input vector, $[\boldsymbol{\alpha}_s]\left(\in \mathbb{R}^{2n_v \times 2n_v}\right)$ is the state matrix, $[\boldsymbol{\beta}_{s\ell}]\left(\in \mathbb{R}^{2n_v \times 2}\right)$ is the ℓ component input matrix.

$$\dot{\mathbf{Z}}_\ell = [\boldsymbol{\alpha}_s]\mathbf{Z}_\ell + [\boldsymbol{\beta}_{s\ell}]\mathbf{U},\ \ell = x, y, z \tag{3.41}$$

$$\mathbf{Z}_\ell = \begin{bmatrix} \mathbf{J} \\ \mathbf{K} \end{bmatrix}, [\boldsymbol{\alpha}_s] = \begin{bmatrix} [\mathbf{0}_{n_v \times n_v}] & [\mathbf{1}_{n_v \times n_v}] \\ [\boldsymbol{\alpha}_{e1}] & [\boldsymbol{\alpha}_{e2}] \end{bmatrix}, [\boldsymbol{\beta}_{s\ell}] = \begin{bmatrix} [\mathbf{0}_{n_v \times 1}] & [\mathbf{0}_{n_v \times 1}] \\ [\boldsymbol{\beta}_{e\ell 1}] & [\boldsymbol{\beta}_{e\ell 2}] \end{bmatrix}, \mathbf{U} = \begin{bmatrix} \dot{J}_E \\ \ddot{J}_E \end{bmatrix}$$

where $[\boldsymbol{\alpha}_{e1}] = -\left([\mathbf{S}] + [\dot{\mathbf{E}}_p]\right)[\mathbf{E}_\mathrm{p}]^{-1}[\mathbf{A}_C]$; $[\boldsymbol{\alpha}_{e2}] = -[\mathbf{E}_\mathrm{p}]^{-1}[\mathbf{V}_S]^{-1}[\mathbf{A}_\mathbf{C}]^{-1}$;

$[\boldsymbol{\beta}_{e\ell 1}] = -\left([\mathbf{S}] + [\dot{\mathbf{E}}_p]\right)[\mathbf{E}_\mathrm{p}]^{-1}[\mathbf{V}_S]^{-1}[\mathbf{A}_C]^{-1}[\mathbf{A}_{E\ell}]$; $[\boldsymbol{\beta}_{e\ell 2}] = -[\mathbf{V}_S]^{-1}[\mathbf{A}_\mathbf{C}]^{-1}[\mathbf{A}_{E\ell}]$;

and $[\mathbf{S}] = diag\left(\sigma_1 \cdots \ \sigma_j \cdots \ \sigma_{n_v}\right), [\mathbf{V}_S] = diag\left(v_1 \cdots \ v_j \cdots \ v_{n_v}\right)$

$[\mathbf{E}_\mathrm{p}] = diag\left(\varepsilon_1 \cdots \ \varepsilon_j \cdots \ \varepsilon_{n_v}\right)$

3.3.1 Harmonic Solutions to the ECD

The steady-state harmonic solutions to Eq. (3.41) are given by Eq. (3.42a), Eq. (3.42b), where ε_{r_R}, ε_{r_I}, σ_j, v_j are the real, imagine part relative permittivity, electric conductivity, and volume of the j^{th} element.

$$\mathbf{J}_{\ell\mathrm{Re}} = \left([\mathbf{C}_s] + [\mathbf{D}_s][\mathbf{C}_s]^{-1}[\mathbf{D}_s]\right)^{-1}\left([\mathbf{G}_{s\ell}] - [\mathbf{D}_s][\mathbf{C}_s]^{-1}[\mathbf{H}_{s\ell}]\right), \ell = x, y, z \tag{3.42a}$$

where $[\mathbf{C}_s] = \mathbf{I} - \omega^2[\mathbf{E_{PR}}][\mathbf{V}_s][\mathbf{A}_C], [\mathbf{D}_s] = \omega\left(\omega[\mathbf{E_{PI}}] - [\mathbf{S}]\right)[\mathbf{V}_s][\mathbf{A}_C],$

$[\mathbf{G}_{s\ell}] = \omega^2[\mathbf{E_{PR}}][\mathbf{A}_{\mathbf{E}\ell}]J_E, [\mathbf{H}_\ell] = \omega\left(\omega[\mathbf{E_{PI}}] - [\mathbf{S}]\right)[\mathbf{A}_{\mathbf{E}\ell}]J_E$

$$\mathbf{J}_{\ell\mathrm{Im}} = -[\mathbf{C}_s]^{-1}\left([\mathbf{D}_s]\mathbf{J}_{\ell\mathrm{Re}} - [\mathbf{H}_\ell]\right) \tag{3.42b}$$

where $[\mathbf{E_{PR}}] = \varepsilon_0 diag\left(\varepsilon_{r\_R1} \cdots \ \varepsilon_{r\_Rj} \cdots \ \varepsilon_{r\_Rn}\right)$

$[\mathbf{E_{PI}}] = \varepsilon_0 diag\left(\varepsilon_{r\_I1} \cdots \ \varepsilon_{r\_Ij} \cdots \ \varepsilon_{r\_In}\right)$

The ECD in the biological tissues can be formulated as a two-step constrained least-square (CLS) problem: The first CLS solves Eq. (3.42a) for $\mathbf{J}_{\mathrm{Re}}=\left[\mathbf{J}_{\mathrm{xRe}}^{\mathrm{T}}\quad\mathbf{J}_{\mathrm{yRe}}^{\mathrm{T}}\quad\mathbf{J}_{\mathrm{zRe}}^{\mathrm{T}}\right]^{\mathrm{T}}$ by minimizing

$$\sum_{\ell=x,y,z}\left\|\mathbf{J}_{\ell\mathrm{Re}}-\left(\left[\mathbf{C}_s\right]+\left[\mathbf{D}_s\right]\left[\mathbf{C}_s\right]^{-1}\left[\mathbf{D}_s\right]\right)^{-1}\left(\left[\mathbf{G}_{s\ell}\right]-\left[\mathbf{D}_s\right]\left[\mathbf{C}_s\right]^{-1}\left[\mathbf{H}_{s\ell}\right]\right)\right\|^2 \tag{3.43}$$
$$\text{subject to } \left[\mathbf{Q}\right]\mathbf{J}_{\ell\mathrm{Re}}=\mathbf{0}$$

With $\mathbf{J}_{\mathrm{Re}}$, $\mathbf{J}_{\mathrm{Im}}=\left[\mathbf{J}_{x\mathrm{Im}}^{\mathrm{T}}\quad\mathbf{J}_{y\mathrm{Im}}^{\mathrm{T}}\quad\mathbf{J}_{z\mathrm{Im}}^{\mathrm{T}}\right]^{\mathrm{T}}$ in (3.43) by minimizing

$$\sum_{\ell=x,y,z}\left\|\mathbf{J}_{\ell\mathrm{Im}}+\left[\mathbf{C}_s\right]^{-1}\left(\left[\mathbf{D}_s\right]\mathbf{J}_{\ell\mathrm{Re}}-\left[\mathbf{H}_{s\ell}\right]\right)\right\|^2 \text{ subject to } \left[\mathbf{Q}\right]\mathbf{J}_{\ell\mathrm{Im}}=\mathbf{0} \tag{3.44}$$

The eddy-current can be converted to electric fields by the Ohm's law. The real and imagine parts of $\mathbf{E}_\ell$ can be derived by comparing the real and imagine parts of $\mathbf{E}_\ell$ and $\mathbf{J}_\ell$.

$$\mathbf{E}_\ell=\left(\sigma+j\omega\left(\varepsilon_r+j\varepsilon_i\right)\right)^{-1}\mathbf{J}_\ell \tag{3.45a}$$
$$\mathbf{E}_{\ell\mathrm{Re}}=\left(\left(\sigma-\omega\varepsilon_i\right)^2+\omega^2\varepsilon_r^2\right)^{-1}\left(\left(\sigma-\omega\varepsilon_i\right)\mathbf{J}_{\ell\mathrm{Re}}+\omega\varepsilon_r\mathbf{J}_{\ell\mathrm{Im}}\right) \tag{3.45b}$$
$$\mathbf{E}_{\ell\mathrm{Im}}=\left(\left(\sigma-\omega\varepsilon_i\right)^2+\omega^2\varepsilon_r^2\right)^{-1}\left(\left(\sigma-\omega\varepsilon_i\right)\mathbf{J}_{\ell\mathrm{Im}}-\omega\varepsilon_r\mathbf{J}_{\ell\mathrm{Re}}\right) \tag{3.45c}$$
$$\left|\mathbf{E}_{\ell\mathrm{Im}}\right|=\sqrt{\mathbf{E}_{\ell\mathrm{Re}}^2+\mathbf{E}_{\ell\mathrm{Im}}^2} \tag{3.45d}$$

3.3.2 Time Dependent to the ECD

In Eq. (3.41), $\boldsymbol{\alpha}_{e1}$, $\boldsymbol{\beta}_{e1\ell}$ change rapidly compared with $\boldsymbol{\alpha}_{e2}$, $\boldsymbol{\beta}_{e2\ell}$. It means that it is a stiff system. The time dependent response can be obtained by applying the implicit Euler method:

$$\mathbf{Z}_{\ell}(k+1)=\Delta t\left[\mathbf{I}-\Delta t[\boldsymbol{\alpha}_{s}]\right]^{-1}\left[\mathbf{Z}_{\ell}(k)+[\boldsymbol{\beta}_{s\ell}]\mathbf{U}(k+1)\right],\ell=x,y,z \quad (3.46)$$

subject to $\mathbf{QJ}_{\ell}(\mathrm{k})=\mathbf{0}$

3.3.3 Electromagnet Array

The magnetic vector potential generated by the EM array can be determined by the summation of the magnetic vector potential generated by each EM multiplying its current amplitude. $\mathbf{A}_{\mathrm{E}\ell}$, J_E in $\mathbf{G}_{\ell}$, $\mathbf{H}_{\ell}$ can be replaced by $\mathbf{A}_{\mathrm{EM}\ell}$, $\mathbf{J}_{EM}$ (3.47a, b). $\mathbf{A}_{\mathrm{EM}\ell}$, $\mathbf{J}_{EM}$ are the concatenate matrices of $\mathbf{A}_{\mathrm{E1}\ell}$, $\mathbf{A}_{\mathrm{E2}\ell}$, … $\mathbf{A}_{\mathrm{EM}\ell}$ and J_{E1}, J_{E2}, … J_{EM}. $\mathbf{A}_{\mathrm{Ej}\ell}$, J_{Ej} are the magnetic vector potential generated by the j^{th} EM and current density of the j^{th} EM.

$$[\mathbf{G}_{s\ell}]=\omega^{2}[\mathbf{E}_{\mathbf{PR}}][\mathbf{A}_{EM\ell}]\mathbf{J}_{EM} \quad (3.47a)$$

$$[\mathbf{H}_{\ell}]=\omega\left(\omega[\mathbf{E}_{\mathbf{PI}}]-[\mathbf{S}]\right)[\mathbf{A}_{EM\ell}]\mathbf{J}_{EM},\ell=x,y,z \quad (3.47b)$$

$$[\mathbf{A}_{EM\ell}]=\begin{bmatrix}\mathbf{A}_{E1\ell} & \mathbf{A}_{E2\ell} & \cdots & \mathbf{A}_{Em\ell}\end{bmatrix}$$

$$\mathbf{J}_{EM}=\begin{bmatrix}J_{E1} & J_{E2} & \cdots & J_{Em}\end{bmatrix}^{T}$$

3.3.4 Numerical Verification

The modeling ECD fields of the biological tissues can be numerically verified by the FEA software. Table 3-10 shows the simulation parameters. The exciting frequency is 1MHz, which is under the magneto quasi-static (MQS) approximation [76]. The material properties of the retina use the same parameters simulated in [3], which applies the electrical conductivity and permittivity of the physiological solution on the retina, and the thickness of the Retina is 217 μm [74]. Compared with micro coils, the retina is large enough and can be considered as an infinite plate, which the boundary conditions can be ignored. The constraint matrix (**Q**) does not need to be applied.

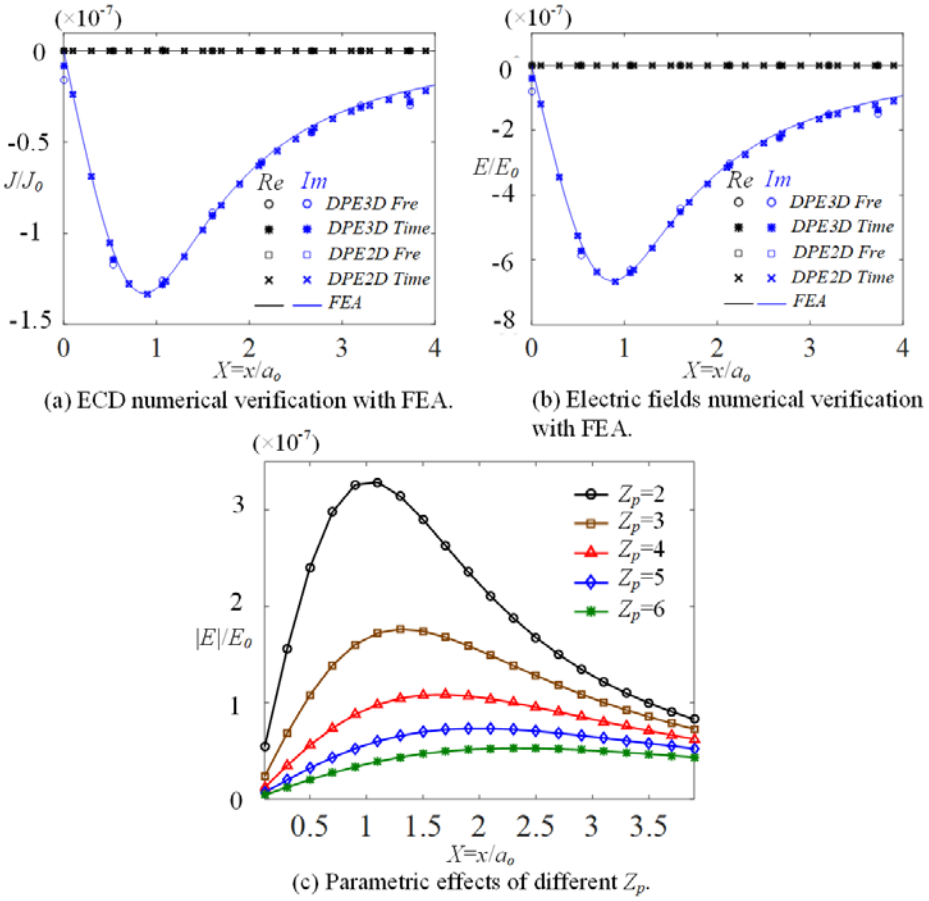

Figure 3-15 Numerical verifications and parametric effects

Fig. 3-15(a), (b) are 2D, 3D models both for the frequency (harmonic response) and time dependent ECD and electric fields simulation results which are coincided with the FEA 2D results. For the time dependent analysis, a cosine wave $J_0 \cdot cos(2\pi fk)$ with f=1 MHz, k=0, Δt, $2\Delta t$, … (time interval Δt=0.5 ns) is utilized as the input current density. J_0 is the current density which passes through the EM. E_0 is the electric field which can be converted from J_0 by Eq. 3.45. The imagine and real parts are the values at k=1500, 2000. Fig. 3-15(c) are the simulation results of different lift-off distance (Z_p). Larger Z_p values have smaller electric fields and the peak positions are far from the center.

Table 3-10 Simulation parameters.

EM			**(μ =4π×10^{-7}H/m, ε_0=8.85×10^{-12} (F/m))**		
Geometry (μm)	a_i	250	**Material**	σ (S/m)	2
	a_o	500		E_{PR} (F/m)	30
	a	250		E_{PI} (F/m)	0
Current	f	1 MHz	**Geometry**	H_p	0.289
				X_p	8
				H_e	0.289
				X_e (3D)	0.444
				R_e (2D)	0.1

Figure 3-16 verifies the magnetic vector potential contributed from a rotated EM with J_0=1 by applying the transformation matrix in Appendix C.

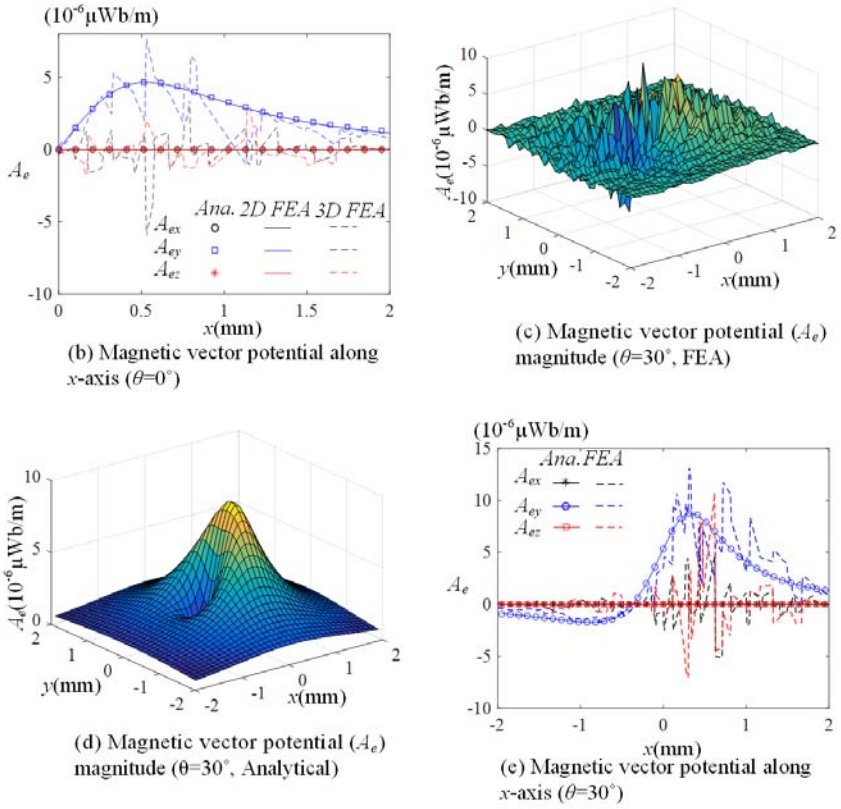

Figure 3-16 Rotated coordinate verification

Fig. 3-16(a) demonstrates the EM rotation configuration which rotates clockwise θ around the y-axis ($\mathbf{n}=[0\ 1\ 0]^T$) with the EM center (x_e, y_e, z_e) at (0, 0, 650)μm. Fig. 3-16(b) are the simulation results of A_{ex}, A_{ey}, A_{ez} for analytical solutions, 2D FEA, 3D FEA. The simulation result of the analytical solution is close to 2D FEA. But, 3D FEA has a lot of noise. It is the reason that causes the fluctuations of real part electric fields of 3D FEA. Fig. 3-16(c), (d) are the simulation results of magnitude of magnetic vector potential at z=0 μm plane of analytical solution and FEA software respectively. The simulations show FEA have fluctuations. Fig. 3-16(e) compares x, y, z directional magnetic vector potential of analytical solutions and FEA along the x-axis. The result shows the results of analytical solution and FEA software have same trend but more noise of FEA software.

3.4 Summary

The distributed parameter element (DPE) method for modeling the irregular shape physical fields with different boundary conditions is presented: 1) The stationary/time dependent, 2D/3D electric field. 2) The harmonic/time dependent, 2D axisymmetric/3D magnetic and eddy-current fields are formulated. Different materials are considered, such as non-ferrous metal and biological tissues. In addition, some details of the formulations are added to improve the calculation efficiency. A flexible grid division method based on equal current is introduced to improve the calculation efficiency of the 2D axisymmetric eddy-current field to deal with the skin effect of eddy-current induced in the non-ferrous metal. A closed form solution for real-time calculations of the magnetic vector potential is also proposed to replace with time consuming calculations of volume integral.

CHAPTER 4. NUMERICAL ILLUSTRATIVE APPLICATIONS

This chapter numerically illustrates the applications of artificial perceptions based on the DPE-based magnetic/electric scanning method. The first application utilizes a set of μ-EMs to transduce a pattern on the retina in the method of magnetic stimulation and compared with the traditional μ-electrodes electrical stimulation. To provide a basis for simulation, a multiple layer structure of the rabbit retina is utilized to demonstrate the feasibility of using DPE method for modelling multiple material properties. In addition, a numerical illustration of the non-mechanical ECD scanning method along with the artificial neural network (ANN) for edge and hole detections is presented; the results are compared with the traditional mechanical ECD scanning.

4.1 Parametric Effects of Artificial Perception

Figure 4-1 illustrates a non-contact artificial perception method magnetically stimulates ECD patterns using a 6×6 μ-EM array. This method consists of two parts. The first part is the algorithm for converting an optical image to M/EC patterns presented in chapter 2 as shown in Fig. 4-1(a) to (d). The feature image can be extracted from the image segmentation and the μ-EM currents are manipulated to scan the ECD patterns. The second part is the calculation of the magnetic, eddy-current, and electric field on the retina by the DPE model. Fig. 4-1(e) illustrates the application of the artificial perception. The μ-EM array is designed to be placed above the macular of the retina for transducing the eddy-current patterns. Fig. 4-1(f) is the eye geometry. The radius, thickness of the eyeball used in simulation are 23mm and 217 μm. Fig. 4-1(g) is the multiple-layers of retinal model.

The thickness and electrical conductivity of the seven layers are listed in Table 4-1. These simulation parameters are based on the published findings ([73]-[75]).

Table 4-1 Thickness and electric conductivity of each layer

Layer name	Thickness (μm)	Electrical Conductivity (S/m)
Ganglion cell layer (GCL)	22	0.0226
Inner plexiform layer (IPL)	23	0.0372
Inner nuclear layer (INL)	27	0.0128
Outer plexiform layer (OPL)	16	0.0187
Outer nuclear layer (ONL)	31	0.0124
Sub-retinal space	40	0.0483
Retinal pigment epithelial (RPE)	20	4.167×10^{-4}

The merits of the DPE method compared with the existing methods will be illustrated. First, the DPE method can be utilized to model the magnetic or electric fields of the curved surface. Fig. 4-2 demonstrates the feasibility of using the DPE method to model the eddy-current fields of the three layers curved surface of the eyeball induced by a μ-EM with a tilt angle (θ=30˚). As shown in Fig. 4-2, the induced eddy-currents are tangential to the surface, which satisfy the boundary conditions. Second, the DPE method formulates the magnetic and eddy-current field in state-space representation and considers the electrical permittivity which the analytical solutions neglects. In this subsection, three examples (μ-EM array magnetic stimulation, μ-electrode array electrical stimulation, a multiple layer retinal structure electrical stimulation) are illustrated for design analysis of the artificial perception.

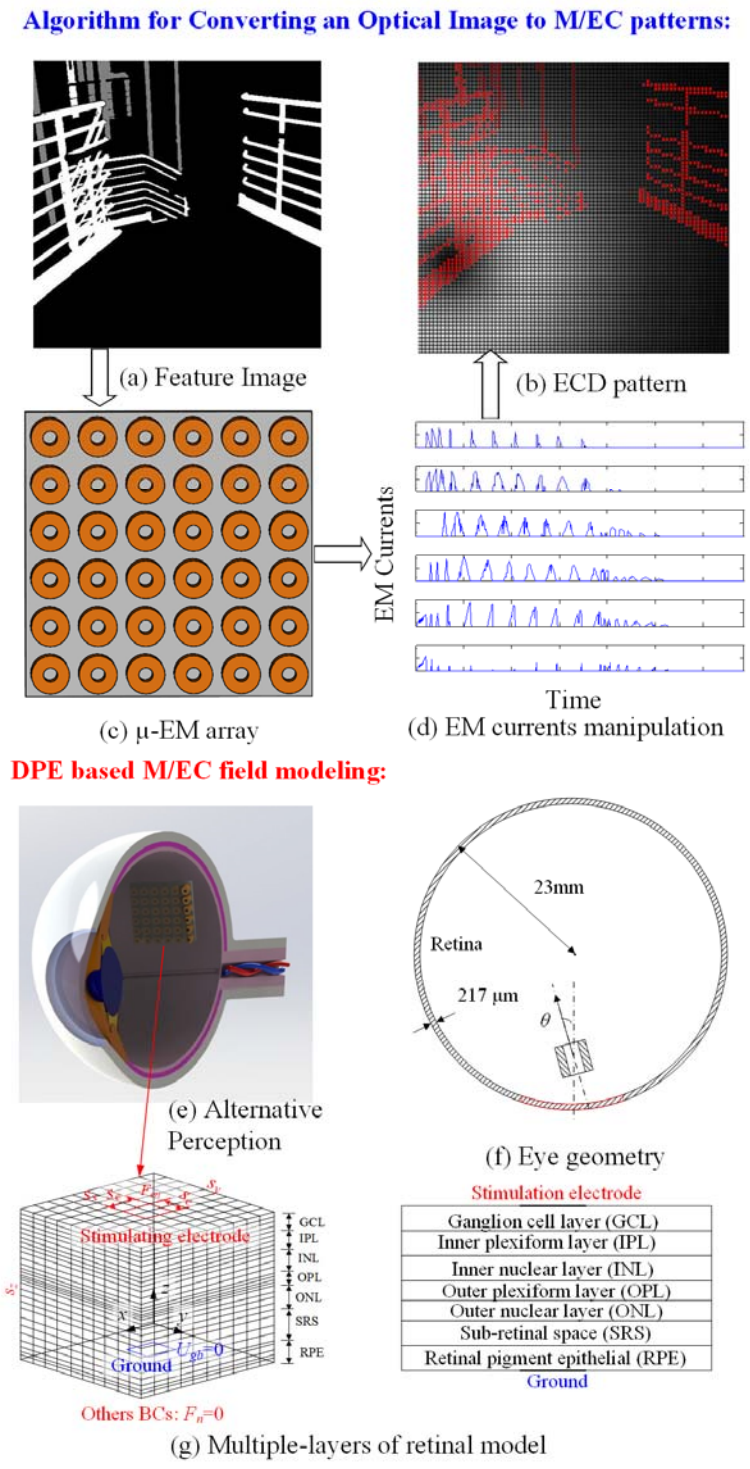

Figure 4-1 Artificial perception methods of μ-EM and retina structure

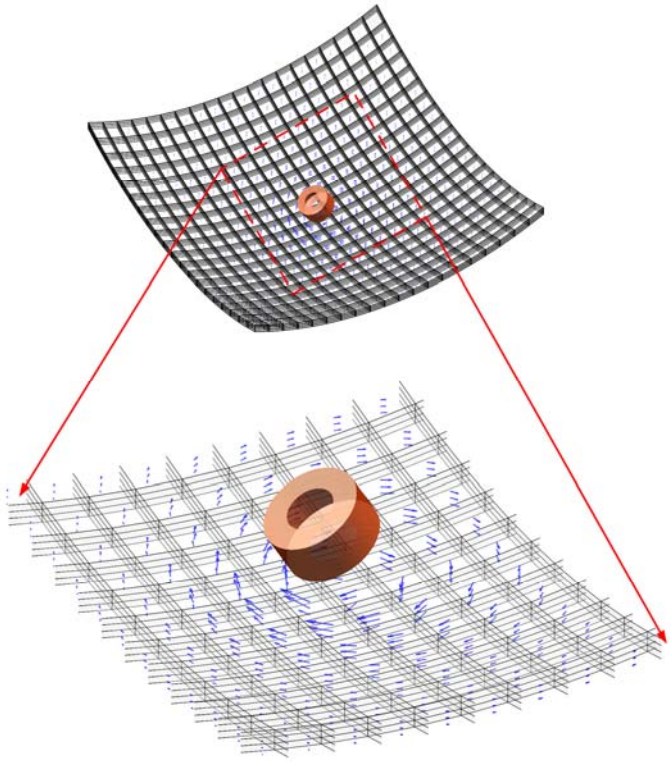

Figure 4-2 ECD distribution of the curved surface

4.1.1 μ-EM Array Magnetic Stimulation

An EM can induce a circular ECD fields in the biological tissues for a single point stimulation. The single point can be expanded to a plane ECD pattern by an EM array. However, the lift-off distances between EM array and biological tissues affect the uniformity of the ECD pattern. Figure 4-3 illustrates the use of a $M \times N$ EM array consisting of a basic 2×2 EM array to control the ECD center on the stimulating point of the biological tissue. The geometry parameters of the EM is shown in Table 3-10. A variable J_0 can be applied to control the maximum ECD point to the desired value by dividing the desired ECD value to the maximum ECD point value with unit current densities by using the DCS modeling method. The desired value is set as $10 \mathrm{Vm}^{-1}$ which is the threshold for neuronal

activation measured by Chan and Nicholson [72]. The transformation from the $M\times N$ EM array to the basic 2×2 EM array can be determined by Eq. (2.3). The input current densities of the 2×2 EM array can be calculated by Eq. (4.1).

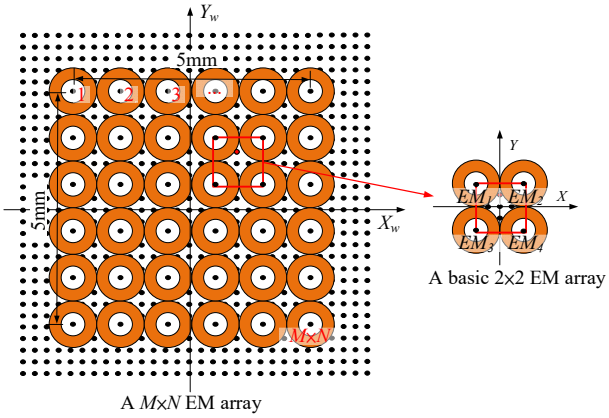

Figure 4-3 The global $M\times N$ EM array and an unit 2×2 EM array

$$J_{EMi} = J_0\left(1-X_i\right)\left(1-Y_i\right) \tag{4.1}$$

$$\text{where } \left(X_i \quad Y_i\right)=\begin{cases}\left(X \quad -Y\right) & i \text{ is an odd number}\\ \left(-X \quad Y\right) & i \text{ is an even number}\end{cases}$$

$$X=x/a_o, Y=y/a_o, J_0 = E_{desired} / E_{\max}$$

Larger lift-off distances lead more uniform ECD movement. Fig. 4-4 shows the ECD center path planning of the cross-road sign along the paths (from L_1 to L_2, to L_3, to L_4, to L_5, to L_6). Fig. 4-5 shows the manipulated EM current densities manipulations result. The geometry of the EM, input current frequency, and the material properties of the biological tissue are the same as Table 4-2. The parameters of the biological tissue geometry are listed in the top row of Table 4-2. The design goal is to transduce the synthetic circular ECD fields at $(X_c, Y_c)=(x_c/a_o, y_c/a_o)$ and have the maximum electric field magnitude

of 10 V/m. Three points in the path are utilized to verify the scan method with the modeling method. Table 4-2 and Fig. 4-6 are the simulation parameters and results.

Table 4-2 Simulation parameters

Plate Geometry: H_p=H_e=0.868, Z_p=Z_e=4, X_p=Y_p=16, X_e=Y_e=0.4103			
	Center Position		Current densities
Z_p	Desired	Simulated	(J_{E1}, J_{E2}, J_{E3}, J_{E4}) ×J_0
4	(-1.231, 3.282)	(-1.231, 3.282)	(EM_2EM_3 EM_8 EM_9) (0.166, 1.272, 1.011, 7.75)
4	(0, 0)	(0, 0)	(EM_{15}, EM_{16}, EM_{21}, EM_{22}) (3.23, 3.23, 3.23, 3.23)
4	(4.103, 0.41)	(4.103, 0.41)	(EM_{17} $EM_{18}EM_{23}$ EM_{24} (3.807, 4.677, 1.592, 1.956)
1.4	(-1.231, 3.282)	(-2.872, 4.923)	(EM_2 EM_3 EM_8 EM_9 (0.037, 0.285, 0.226, 1.736)× J_0

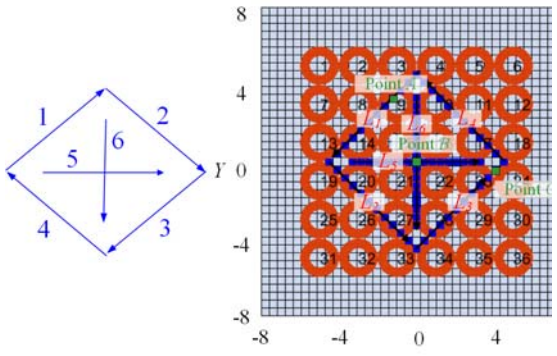

Figure 4-4 Electric scanning path

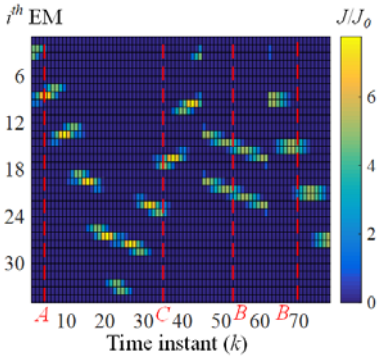

Figure 4-5 Current densities manipulation

When Z_p is equal to 1.4, the synthetized ECD does not have a circular shape and the center positions is not at the desired position. When Z_p is equal to 4, the desired and simulated center (point A, B, C) are at the same positions and the maximum electric field magnitude can achieve the threshold for neuronal activation 10 Vm^{-1}. In [3], a micro-coil is utilized for magnetic stimulation of the rabbit retina ganglion cell.

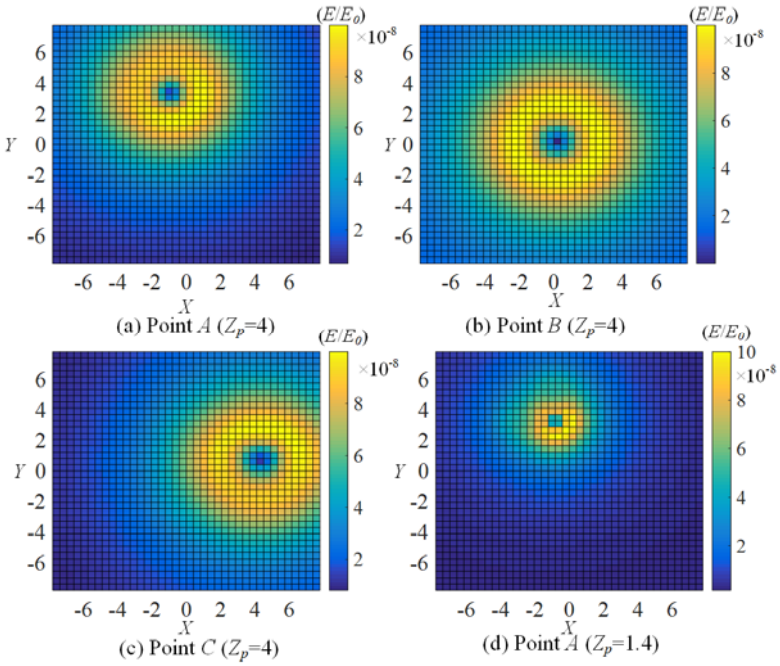

Figure 4-6 Simulations of Eddy-Current Scan

4.1.2 μ-Electrode Array Electrical Stimulation

The traditional method for retinal prosthesis is to place the electrode on the retina. The DPE method is utilized to investigate the effects of electric field stimulated by the μ-electrode array. The electrical property of physiological solution (σ=2 S/m) is used in the simulation. The simulation geometry is shown in Fig. 4-7. As shown in Fig. 4-7(a), the width, depth, and height are 425 μm, 425 μm, and 217 μm respectively. The element number is 17 in width, depth, and 10 in height. First, two stimulating methods (monopolar, bipolar) of a single electrode are illustrated in Figs. 4-7(b) and (c). The configuration of monopolar method is the electrode on the top boundary surface and ground on the bottom boundary surface. The bipolar method is the ground surrounded around the electrode on the top boundary surface.

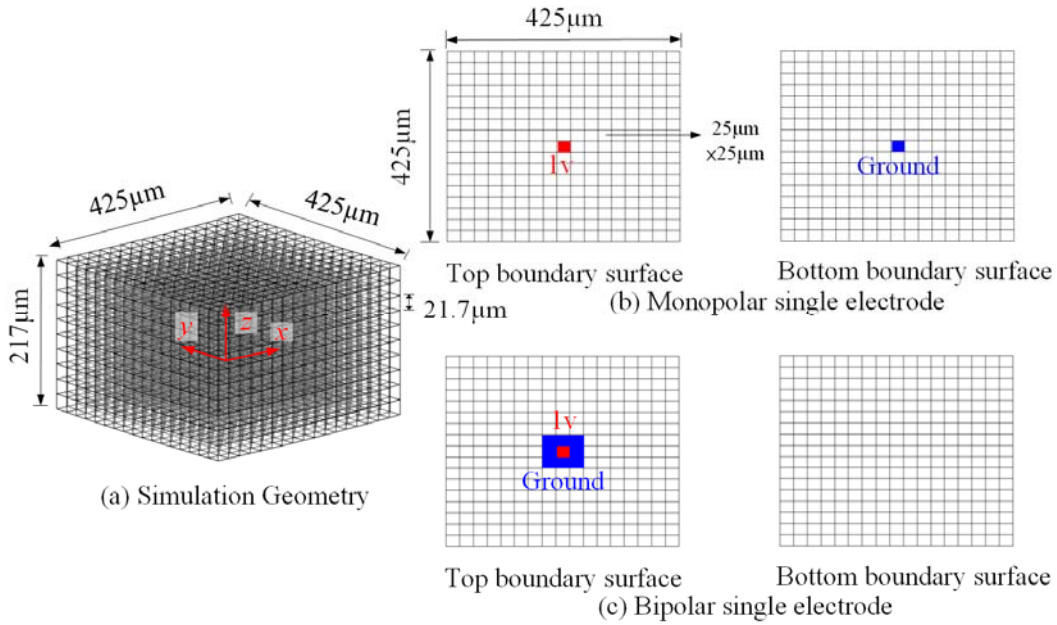

Figure 4-7 Simulation geometry of electrode stimulation

The electric field is determined by Eq. 3-5(a) with $\mathbf{C}_d=\sigma\mathbf{I}$, $\mathbf{C}_e=\mathbf{C}_\alpha=\mathbf{C}_\beta=\mathbf{0}$, $C_a=C_b=0$. Figs. 4-8 and 9 are the simulation results of the monopolar and bipolar single electrode stimulation respectively. Figs. 4-8 (a) and (b), and 4-9 (a) and (b) are the electrical potential and electrical field magnitude distributions in $y=0$ plane. Figs. 4-8 (c) and (d), and 4-9 (c) and (d) are the electrical potential and electrical field magnitude distributions in $z=-94.33$ μm plane, which are the elements of the 5th layer from up to bottom. As shown in Figs. 4-8 (a) and (b), and 4-9 (a) and (b), the peak of the electric field of the monopolar single electrode stimulation is larger and concentrated on the top boundary surface. On the contrary, the peaks of the electric field of the bipolar electrode stimulation are both at top and bottom boundary surfaces.

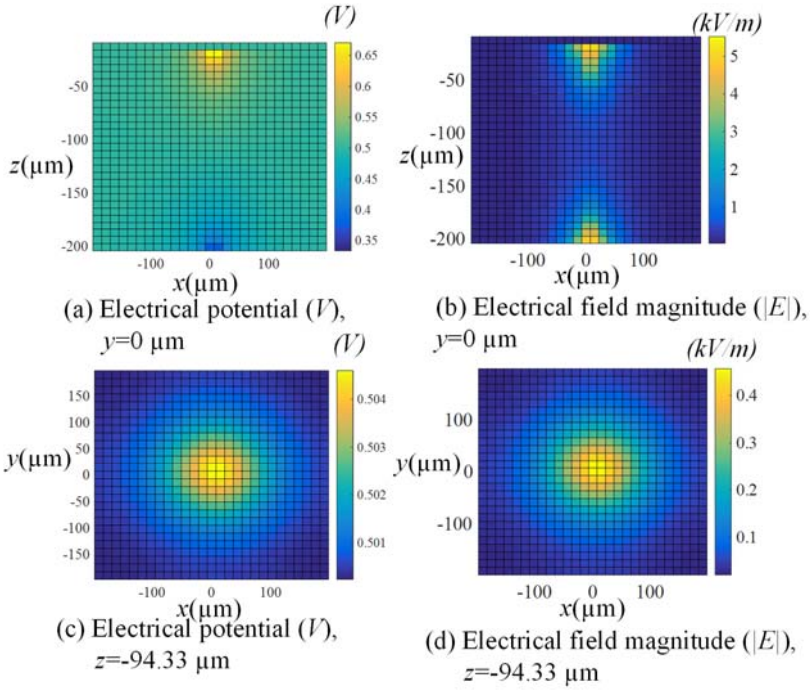

Figure 4-8 Simulation results of monopolar single electrode stimulation

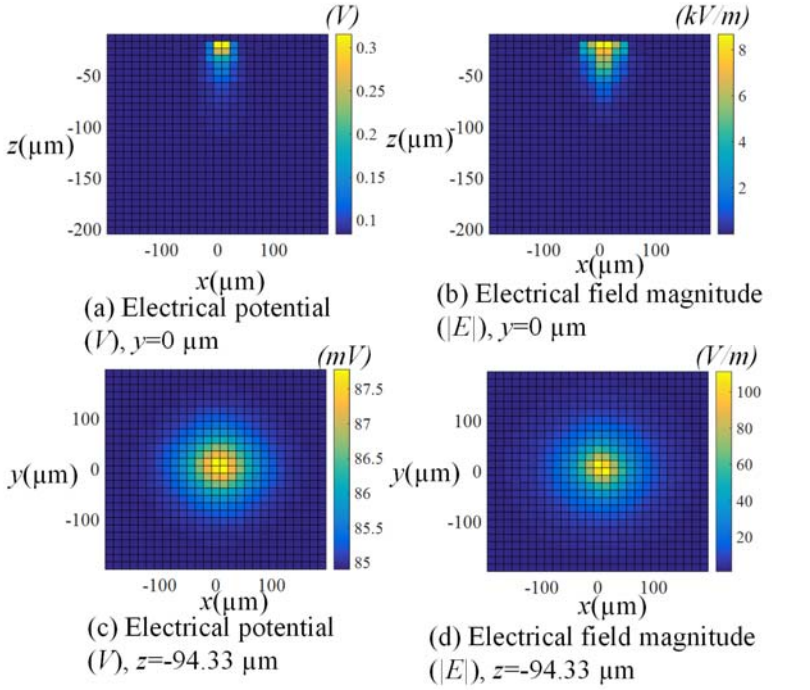

Figure 4-9 Simulation results of bipolar single electrode stimulation

As shown in Figs. 4-8(c), (d) and 4-9(c), (d), the maximum point positions and electric field values in z=-94.33 μm plane of the monopolar and bipolar electrode stimulations are $[x, y, |E|]^T=[0, 0, 490.5]^T$, $[0, 0, 9.95]^T$ (μm, μm, V/m). The electric field peak value of the monopolar electrode stimulation is larger in z=-94.33 μm plane.Figure 4-10 shows the configuration of the monopolar and bipolar electrode array stimulation. The electrodes and ground of the monopolar electrode array stimulation are on the top and bottom boundary surface respectively. The bipolar electrode array stimulation method is the ground surrounded around the electrode array on the top boundary surface. Figures 4-11, 12 are the simulation results of the monopolar and bipolar electrode array stimulation respectively. An example is utilized to validate the electric scanning method. The parameters of desired, simulated position, voltage, and the input voltages of electrodes are listed in Table 4-3. The simulation results of monopolar, bipolar electrode array are shown in Fig. 4-11, 12. Fig. 4-11, 12(a), (b) are the electrical potential and electrical field magnitude distributions in y=0 plane. Fig. 4-11, 12(c), (d) are the electrical potential and electrical field magnitude distributions in z=-94.33 μm plane, which are the elements of the 5th layer from up to bottom. As shown in Table 4-3, the peak of the electric field can be stimulated in the desired position by using the monopolar method. However, there is an element difference (25μm) in x, y direction by using the bipolar method.

Table 4-3 Electric scanning desired/simulated parameters

	Peak position (x, y) (μm)		**Peak value** (V)		**Input voltage** (V)
	Desired	Simulated	Desired	Simulated	$V_{1,2,4,5}$
Monopolar	(-25, -25)	(-25, -25)	10	10.04	0.0077
Bipolar	(-25, -25)	(0, 0)	10	9.948	0.0239

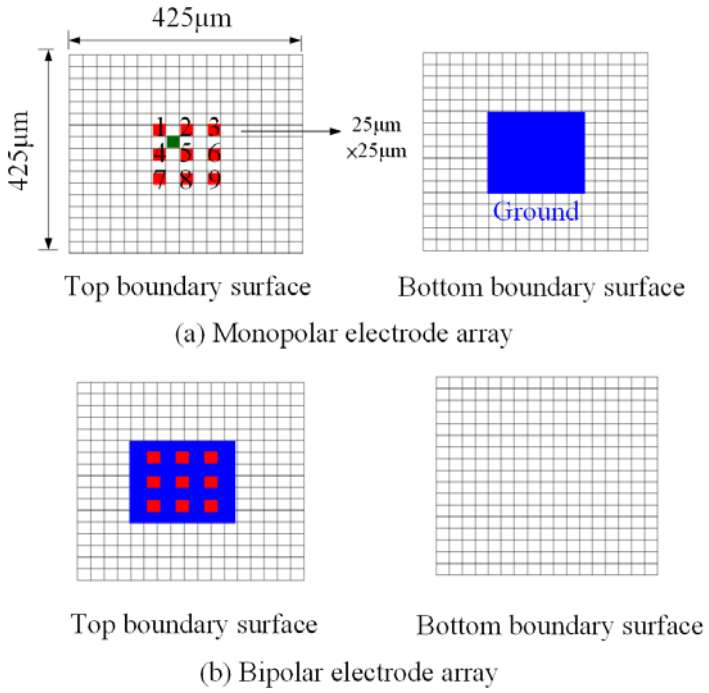

Figure 4-10 Simulation results of bipolar single electrode stimulation

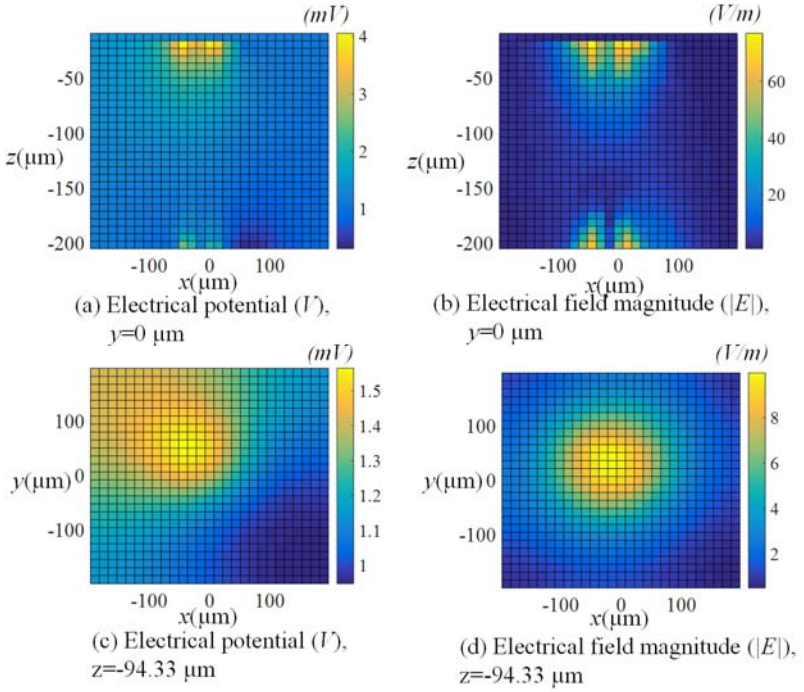

Figure 4-11 Simulation results of monopolar single electrode stimulation

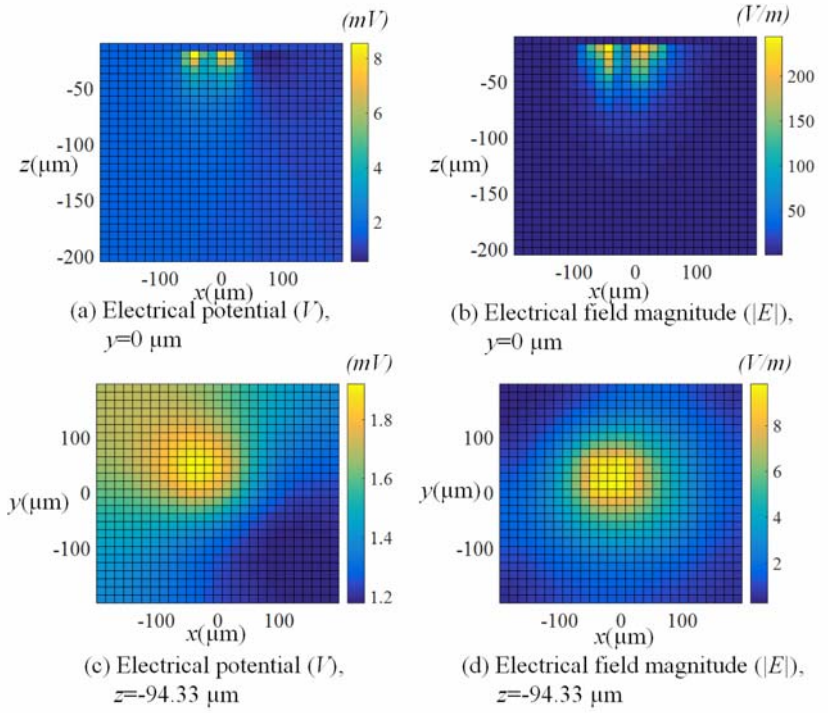

Figure 4-12 Simulation results of bipolar electrode array stimulation

4.1.3 μ-Electrode of a Multiple Layer Retinal Structure

The previous two sub-sections focus on the magnetic/electric scanning method of the μEM/μ-electrode array. The electrical conductivity of the retina is assumed to be the same and uniform. In this subsection, the DPE method is utilized to design analysis of the electrical stimulation on the multiple layer structure of the retina for different electrical conductivity. Figure 4-1(g) shows the cross section of a multiple-layers retinal simulation model including seven layers of a rabbit retina. The values are extrapolated from rabbit retina [75]. Although the rabbit eyes exhibit difference in thickness of retinal layer from humans, utilization of these parameters for modeling is still reasonable due to the resemblance between the human's retinal and rabbit's structure. The thickness and electric conductivity are shown in Table 4-1. The desired value can be set as $10Vm^{-1}$ which is the

threshold for neuronal activation measured by Chan and Nicholson [72]. The inner and boundary surface electric field can be determined by Eq. (4.2a), Eq. (4.2b) with the difference method.

Inner surface:

$$E_x = \frac{V_{i,j,k} - V_{i+1,j,k}}{x_{i+1,j,k} - x_{i,j,k}}, E_y = \frac{V_{i,j,k} - V_{i,j+1,k}}{y_{i,j+1,k} - y_{i,j,k}}, E_z = \frac{V_{i,j,k} - V_{i,j,k+1}}{z_{i,j,k+1} - z_{i,j,k}} \tag{4.2a}$$

Boundary surface with constant voltage:

$$E_x = \frac{V_{i,j,k} - V_b}{x_{i+1,j,k} - x_{i,j,k}}, E_y = \frac{V_{i,j,k} - V_b}{y_{i,j+1,k} - y_{i,j,k}}, E_z = \frac{V_{i,j,k} - V_b}{z_{i,j,k+1} - z_{i,j,k}} \tag{4.2b}$$

Figure 4-1 (g) shows the simulation geometry and boundary conditions for the epi-retinal prosthesis. The square shape electrode is on the top of the multiple-layers of epi-retinal model. A cuboid of side lengths s_x, s_y, s_z is utilized for the epi-retinal model. The height (s_z) is the summation of seven layers. The boundary condition of the surface contacted with the stimulating electrode set as the normal current density with the value F_{en}, which is equal to the Neumann boundary condition in Eq. (3.2b) with F_{n0}=0, F_{n1}=F_{en}. The ground has the same size on the center of the bottom. Other boundary surfaces set as the floating flux (F_{n0}=F_{n1}=0).

The parameters of the simulation model are s_x=s_y=250 μm, s_z=179 μm, and ε_{th}=0.1 μm. Each layer in *z*-direction is divided to four equal layers, and 10 elements are uniformly distributed in x, y directions. Totally, there are 2800 elements. The electric fields (|E|) of the bottom layer elements (z=-19.25 μm) of the Ganglion cell are utilized to verify the DPE method by FEA software (Comsol) as shown in Fig. 4-13. To provide the quantitative comparisons, the relative percentage maximum error is defined as the differences between

the distributed model and FEA relative to the maximum FEA values as follows: $\frac{|\mathbf{E}|_{DPE}-|\mathbf{E}|_{FEA}}{|\mathbf{E}|_{FEA\_Max}}\times 100\%$. The average relative percentage maximum error of the electric field magnitude is 1.368%. An example is utilized to demonstrate the DPE method for investigation of the parametric effects on the side length of the electrode and current density for the elements of the bottom layers of GCL. In Fig. 4-14, *x*-axis is the normal current density values applied on the electrode and y-axis is the maximum magnitude of electric fields of the elements. The threshold of the current density values of side-length 100, 200 μm electrodes for triggering an action potential are 0.36, 0.3 A/m^2.

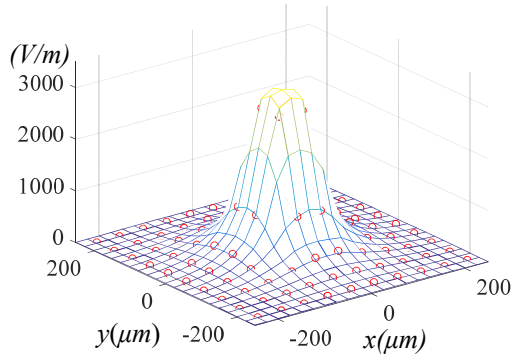

Figure 4-13 Simulation results

(z=-19.25μm)

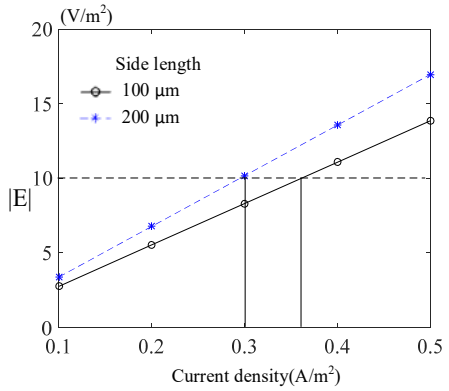

Figure 4-14 Parametric effects of the epi-retinal stimulation

4.2 Eddy-current Sensing in Manufacturing Applications

Figure 4-15 illustrates an application of non-mechanical Eddy-current scan for nondestructive detection applications. Fig. 4-15(a) demonstrates the traditional Eddy-current scan for edge and hole detections by moving a single eddy-current sensor. Fig. 4-15(b) illustrates the non-mechanical eddy-current scan (EC-scan) which utilizes the EM-

sensor array for edge and hole detections non-mechanically. Without moving the Eddy-current sensor, the properties of the workpiece, such as the position of the edge or the center of the hole, can be estimated by the sensor data sequences when adjusting the current amplitudes.

Table 4-4 shows the input current series of 1D and 2D non-mechanical scan. The left column are the input currents of 1D non-mechanical scan. $A_{+}(k)$ and $A_{-}(k)$ are input currents of EM±. The intensity of EM- varies from 1 to 0 and EM+ from 0 to 1 during ECD scan. The elements of the right column are the input currents of 2D non-mechanical scan. The ECD center moves from X- to X+ and Y+ to Y- as shown in Fig. 4-15(b). An artificial neural network (ANN) can be utilized for geometrical parameter estimations as shown in Fig. 4-16. The architecture of the ANN consists of $n_a \times m_a$ nodes for the input layer and k_a nodes for the output layer, where n_a is the number of sensor, m_a is the number of time instance, and k_a is the number of feature to estimate. The input matrix ($\mathbf{I_a}$) and output matrix ($\mathbf{O_a}$) can be expressed in Eq. (4.3). $\mathbf{I_a}$ is a $n_a m_a \times 1$ column vector, which consists of n_a $m_a \times 1$ column vector ($\mathbf{S_i}$). $\mathbf{S_i}$ is the i^{th} sensor data sequences during scanning. The elements of $\mathbf{O_a}$ are the feature values.

Table 4-4 Algorithm to generate scanning currents

1D non-mechanical ECD scan	2D non-mechanical ECD scan
for a_x=-1:Δa:1 $A_{-}(k)$=0.5(1-a_x) $A_{+}(k)$=0.5(1+a_x) k=k+1 end	for a_x=-1:Δa:1 for a_y=1:-Δa:-1 $A_1(k)$=0.25(1-a_x)(1+a_y) $A_2(k)$=0.25(1+a_x)(1+a_y) $A_3(k)$=0.25(1-a_x)(1-a_y) $A_4(k)$=0.25(1-a_x)(1-a_y) end end

$$\mathbf{I_a}=\begin{bmatrix}\mathbf{S}_1 & \mathbf{S}_2 & \cdots & \mathbf{S}_n\end{bmatrix}^{\mathrm{T}},\ \mathbf{S_i}=\begin{bmatrix}s_i(1) & s_i(2) & \cdots & s_i(m)\end{bmatrix}^{\mathrm{T}},$$
$$\mathbf{O_a}=\begin{bmatrix}f_1 & f_2 & \cdots & f_n\end{bmatrix}^{\mathrm{T}} \tag{4.3}$$

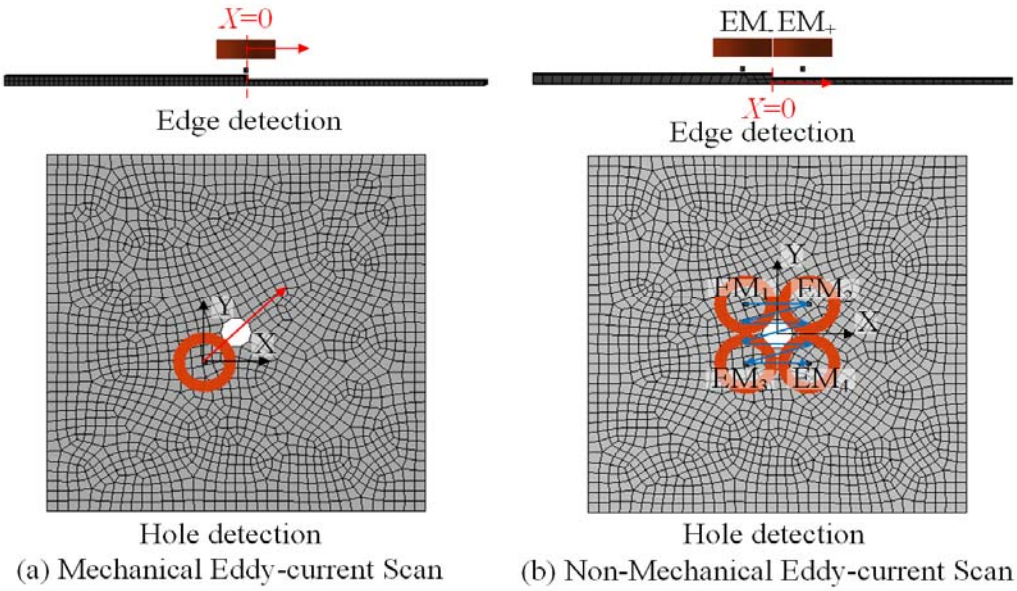

Figure 4-15 Mechanical and non-mechanical Eddy-current scan

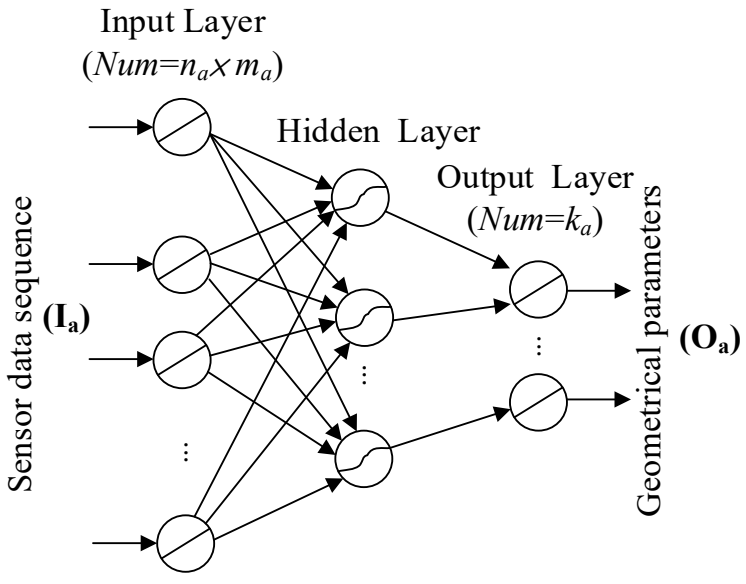

Figure 4-16 Neural network for geometrical parameter estimation

4.2.1 Mechanical ECD Scanning

The commercial FEA software (Comsol) is utilized to verify the DPE modeling method for the edge and hole detections. Table 4-5 are the simulation parameters. The MFD of the EC-sensor is determined by Eq.(3.18). Fig. 4-17 (a) is the edge detection geometry and Fig. 4-17(b) is the hole detection geometry which the radius of the hole is 3mm. The mesh is generated from the mesh generator software with the mesh size 1mm. A computing radius 18mm is used to improve the computational efficiency. Only the elements in the computing radius are calculated. Figure 4-17(c)-(f) are the MFD simulation results of moving the EM along the center line for a step and a hole in Fig. 4-17(a), (b). The DPE simulation results are close to FE, but some noises exist some noises in the real part FEA. The noises may be caused by the fact that FEA numerically integrates over the continuous domain. Fig. 4-17(c) shows the shape of z-component MFD of the eddy-current sensor during the mechanical scanning is similar to the curve of the Gaussian smooth on the edge detection. It can be explained by that the MFD value of the sensor is summations of the effects of the eddy-currents on the plates, which behaves like a Gaussian filter. Moreover, the *z*-component MFD values is a one to one function to *X*, which implies that during the mechanical scan, the position in *X* direction can be found from z-component value. The thickness and displacement of two layers of the step can be determined by mapping to the MFD magnitude and phase [78]. Fig. 4-17(d), (f) show the MFD values during edge and hole detections. The results show that *x*, *y* components of MFD values are smaller than the *z*-component and have more noises. Fig. 4-17(e) shows the real and imagine part z-component MFD values during mechanical scanning. The DPE method agrees with FEA and fewer noises.

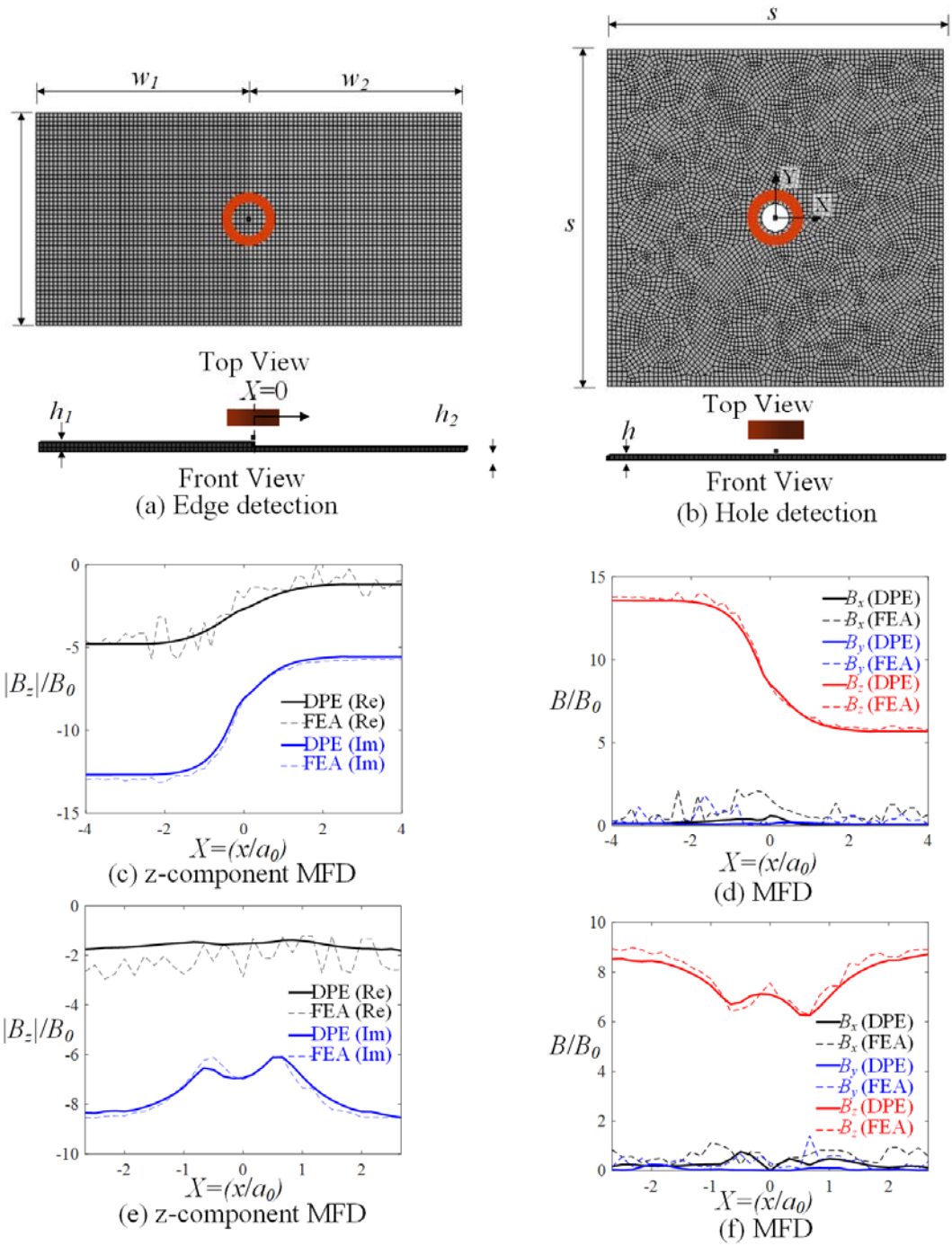

Figure 4-17 Mechanical scanning simulation results

Table 4-5 EM simulation parameters

EM			
Coil (mm)	a_i, a_o, a	3.75, 6, 2	
Wire	N_w	60	
	d_w(mm)	0.35	
Current:	I_E (A)	1	
	f (kHz)	20	
Sensor			
z_s (mm)	-4.5		
Plate (mm):			
w_1=w_2=d=s=48	h	1	
h_1 2	h_2	1	

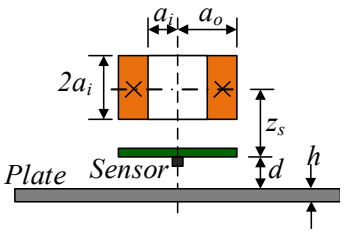

4.2.2 Non-Mechanical ECD Scanning

Unlike traditional mechanical ECD scanning, a non-mechanical ECD scanning method is proposed. The positions of EM and sensor array are fixed. By changing the input currents of EM using the push-pull principle, the ECD center can be scanned between the EMs. Fig. 4-18(a), (b) are the EM, sensor, plate configuration of the edge and hole detections. The mesh size and computing radius of Fig. 4-18(a) are 2 mm and 36mm, Fig. 4-18(b) are 3 mm and 18mm. Fig. 4-18 (c), (d) are the input currents of EMs. The sensor data sequences can be inputted to the ANN for training and testing (70% for training, 15% for test, and 15% for validation). Fig. 4-18 (a), (b) are the input matrices ($\mathbf{I_a}$) for 1D and 2D ECD scanning. x-axis is the j^{th} position, and y-axis is the i^{th} current sensor data. Fig. 4-18(c), (d) are the desired and estimated positions. The mean squared error (MSE) is 0.0067% for 1D scan and average distance error is 0.0013 for 2D scan.

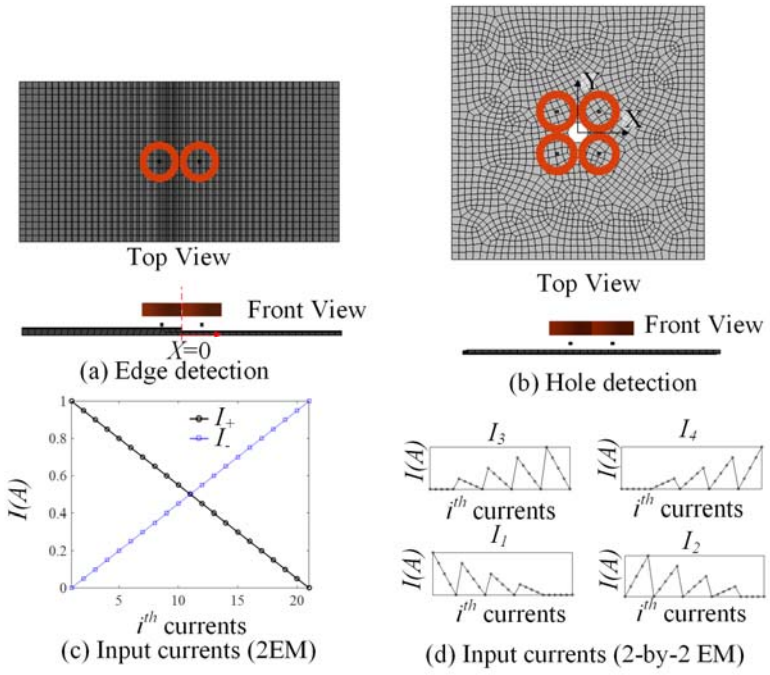

Figure 4-18 Non-mechanical scanning configurations and input currents

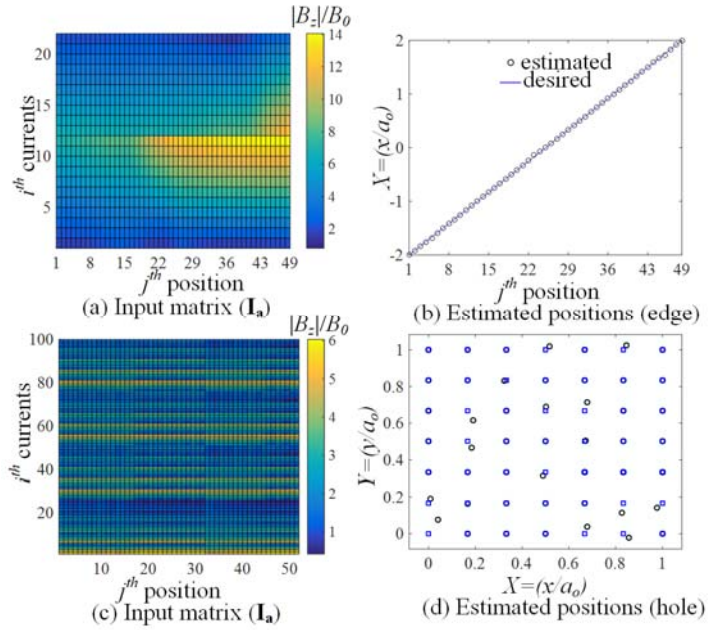

Figure 4-19 Non-mechanical scanning simulation results

4.3 Summary

This chapter numerically illustrates a new application of utilizing the μEM array for magnetic stimulation on retinal prosthesis based on the DPE method, which includes modelling of the magnetic/eddy-current fields and input currents manipulations of the μEM array. The electric field of the traditional electrical stimulation by using the μ-electrode array is also simulated. Besides the artificial perception, the non-mechanical scanning method for edge and hole detections along with ANN is also validated by the DPE method and compared with the traditional mechanical scanning method.

CHAPTER 5. EXPERIMENTAL DEMONSTRATION

In Chapter 2, an algorithm for converting an optical color image to magnetic/eddy-current patterns has been proposed, which controls the MFD peak (or ECD center) at the desired position in a plane by manipulating the input currents of the EMs. The derivation of the DPE-based models has been presented in Chapter 3, which provides a basis to numerically analyze the 2D or 3D irregular shape magnetic and electric fields involved in applications when utilizing the magnetic/eddy-current sensing method in Chapter 4. This chapter presents the experimental results evaluating the effects of the continuous magnetic field manipulation method on the applications that have motivated this thesis. Specifically, three sets of results are presented: The first mechanically evaluates the spatial accuracy of the peak-MFD and ECD-center manipulated using the method presented in Chapter 2 on a non-ferrous metallic plate; both 1D and 2D configurations are considered. With the validated continuous-scanning method, its effectiveness is demonstrated on biological tissues (in the second set of experimental results) with four electrodes using the method of electrical muscle stimulation on human arm, and on a non-ferrous plate (in the third set of the experimental results) demonstrating edge and hole detections.

5.1 Magnetic/Eddy-Current Scanning Method

The effects of magnetic/eddy-current scanning motions on the accuracy of the MFD peak and ECD center have been experimentally verified; both 1D and 2D magnetic scanning patterns are considered.

5.1.1 1D Magnetic Experimental Illustration

As shown in Fig. 5-1, the algorithm of the continuous-field scanning actuator has been designed on two bases:

1. Two Gaussian curve-fit parameters (B_o and σ_m) in Eq. (2.1), which characterize the peak value and shape of the MFD distribution of an EM coil.

2. The push-pull operational principle in Eq. (2.2) where the variation due to the spatial non-linearity of MFD is compensated so that the maximum MFD can be maintained at a constant value.

To validate the above fundamentals of the algorithm for implementing the inverse model, two experiments were performed to simulate a 1D magnetic scanning with two EMs of a 2×2 EM unit (Fig. 5-1d). The first experimentally determines the two Gaussian parameters (B_o and σ_m) for approximating the MFD of an EM. The second experimentally validates the inverse model which determines the input currents to generate a constant peak-MFD at four specified positions.

Fig. 5-1(a) shows the experimental setup for measuring the MFD field of the 1D magnetic scanning, which consists of a power amplifier, two identical air-core EMs, magnetic sensor and 1D translation stage (with a 5μm resolution). The current-controlled power amplifier is utilized to generate magnetic field in space, which was measured by a digital 3-axis AMR magnetic sensor (BMC050) that has a relatively large measurement range (±1mT) and high resolution (0.3μT). Moved by the 1D stage, the sensor measured B_z along the a_x direction as shown in Fig. 5-1(a). The specific values of the geometrical parameters used in the experiments are listed in Table 5-1.

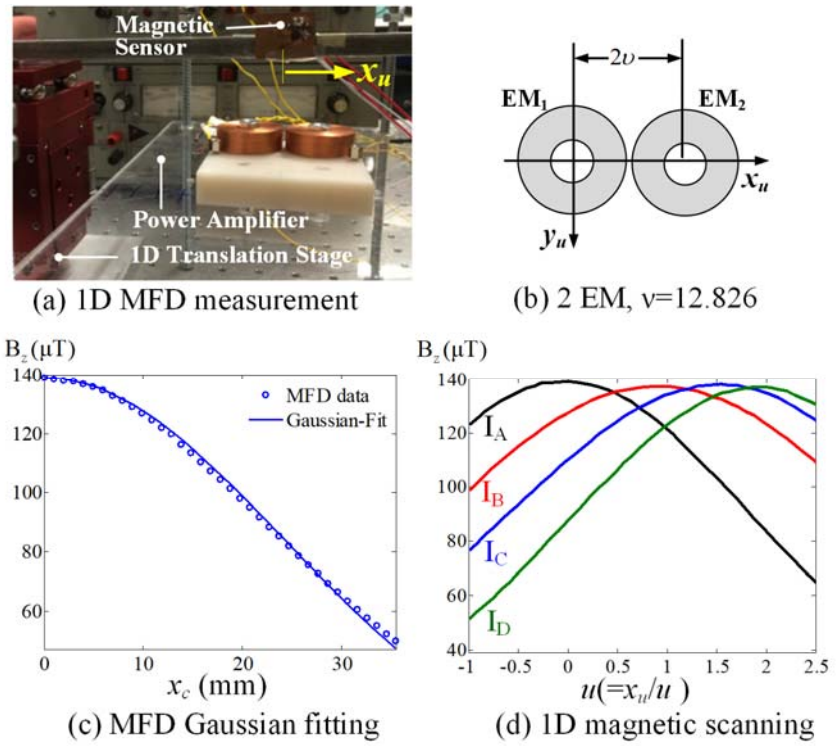

Figure 5-1 Results of 1D magnetic experiments

Table 5-1 Values of the air-core EM parameters

EM (AWG 28 wire)	**Geometry** (mm)		**Gaussian fit**	
Inside radius	a_i	4.5	B_0 (μT)	138.389
Outside radius	a_o	15.5	σ_m (mm)	24.154
Length	ℓ	9.6		
Distance from surface	h	65		

The two Gaussian parameters (B_o and σ_m) for approximating the MFD of the EM, which were determined by applying non-linear regression on the measured data, are listed in right column of Table 5-1. Other experimental results are summarized in Fig. 5-1(c, d) and Table 5-2. As shown in Fig. 5-1(c) the z-component of the MFD along the radial direction can be characterized by a two-parameter Gaussian approximation in Eq. (2.1).

Table 5-2 1D MFD measured data

Peak-MFD position (mm)		**Input currents** (A)
Specified (x_r, u)	Measured (x_r, u)	I_i (I_-, I_+)
0, 0	0, 0	I_A (1, 0)
11.58, 1	11.83, 1.02	I_B (0.561, 561)
18.73, 1.5	17.37, 1.491	I_C (0.273, 0.819)
23.66, 2	23.66, 2	I_D (0, 1)

5.1.2 2D Magnetic Experimental Validation

An experimental study was conducted to verify the spatial accuracy of 2D peak-MFD scanning for the illustrative example in Section 2.2.2. The experimental setup is shown in Fig. 5-2, which consists of a 3D translation stage (with 1μm resolution) that moves a magnetic sensor over the scanning space of a 2×2 EM unit with its magnetic field under the control of four-channel current amplifiers. For examining the concept feasibility, the 2×2 EM array used in the experimental study is similar but scaled-up version of that shown in Table 5-3 and Fig. 5-3(a). The geometry of the air-cored EMs are listed in the first row of Table 5-3. Since the 2D MFD measurements are time-consuming, the following three points are chosen for investigation, where the units of the (x, y) coordinates are in mm: A(0.5, 3.5), B(0.86, 3.32), C(0.41, 3.77). The corresponding coordinates (x_r, y_r) as shown in Fig. 5-3 are A(0, 0), B(4, 2), C(−1, −3). The measuring plane (formed by the 2×2 EM unit as illustrated in Fig. 5-3(a) is w_x=w_y=15mm and divided into N_{sx}=N_{sy}=31 (1 mm resolution) or 961 points. The results are summarized in Table 5-3 and Figs. 5-3(b) to 5-3(d).

Table 5-3 2D MFD control measurement data

EM geometry: a_i=3.75, a_o=5.5, l=3.96, h=20, σ_c=11		
Peak position (mm)		**Input currents** (A)
Desired (x_r, y_r)	Measured (x_r, y_r)	I_i (I_1, I_2, I_3, I_4)
A 0, 0	0, 0	I_A (0.321, 0.321, 0.321, 0.321)
B 4, 2	4, 2	I_B (0.109, 0.689, 0.051, 0.322)
C −1, −3	−1, −3	I_C (0.166, 0.116, 0.556, 0.387)

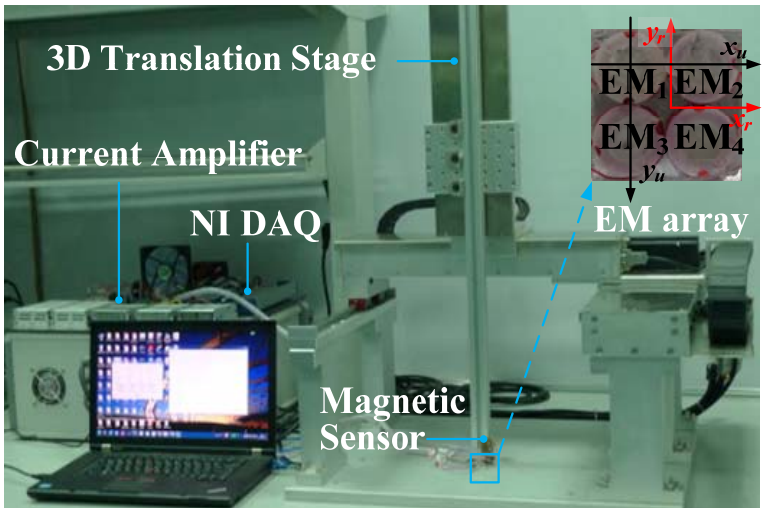

Figure 5-2 Experimental setup

Eq. (2.1) can be expressed by Eq. (5.1) where a_x and a_y are input current parameters in x, y directions. The values of a_x, a_y to control the peak of synthetic MFD to x, y position can be determined by solving the systems of equations in Eq. (5.2). Four EMs can be considered to have identical properties, a_x, a_y have analytical solutions in Eq. (5.3). Otherwise, four EMs have different properties, a_x, a_y can be numerically solved in Eq. (5.1). Table 5-4 show the geometry and Gaussian parameters of four EMs and Fig. 5-4 is the MFD measurements of four EMs and compared with analytical solutions.

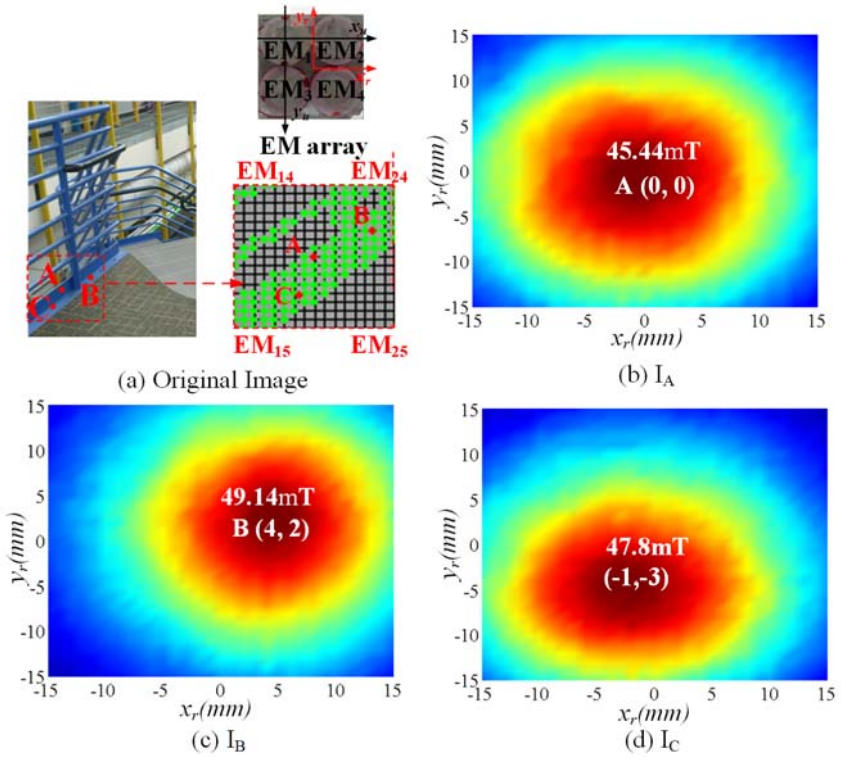

Figure 5-3 Experimental verification of 2D scanning

$$B(x,y,a_x,a_y)=\sum_{i=1}^{4}B_{0i}G_{xi}(x,a_x)G_{yi}(y,a_y) \tag{5.1a}$$

$$G_{xi}(x,a_x)=\frac{1-a_{xi}}{2}e^{-\frac{(x-\upsilon_{xi})^2}{2\sigma_i^2}};G_{yi}(x,a_y)=\frac{1-a_{yi}}{2}e^{-\frac{(y-\upsilon_{yi})^2}{2\sigma_i^2}} \tag{5.1b,c}$$

$$\text{where } \begin{pmatrix} a_{xi} & a_{yi} \end{pmatrix}=\begin{cases} \begin{pmatrix} a_x & -a_y \end{pmatrix} & i \text{ is an odd number} \\ \begin{pmatrix} -a_x & a_y \end{pmatrix} & i \text{ is an even number} \end{cases} \tag{5.1d}$$

$$\begin{cases} \dfrac{\partial B}{\partial x}=0 \\ \dfrac{\partial B}{\partial y}=0 \end{cases}, \text{ find } a_x,\ a_y \quad (5.2) \quad a_k=\frac{\upsilon\left(1-e^{\frac{2\upsilon k}{\sigma^2}}\right)+k\left(1+e^{\frac{\upsilon k}{\sigma^2}}\right)}{\upsilon\left(1+e^{\frac{2\upsilon k}{\sigma^2}}\right)+k\left(1-e^{\frac{\upsilon k}{\sigma^2}}\right)},k=x,y \quad (5.3)$$

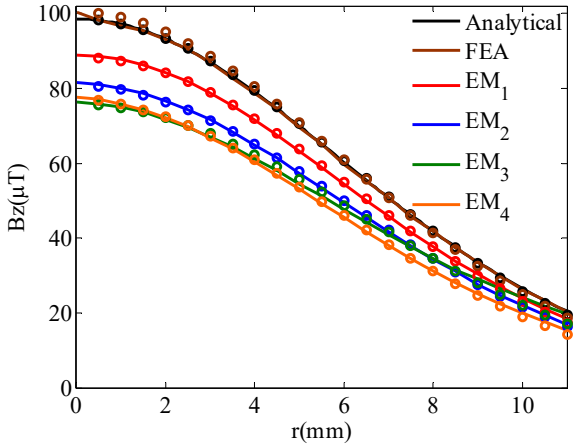

Figure 5-4 MFD and magnetic Gaussian approximation

Table 5-4 EM geometry and Gaussian parameters

N_w=40 turns, AWG 28: A_{wire}=0.081(mm^2) a_i=3.75, a_o=5.5, l=4, h=11, υ= a_o (mm)				
	B_0 (μT)	σ(mm^2)	$υ_x$ (mm)	$υ_y$ (mm)
EM_1	88.3	6.03	5.675	-5.425
EM_2	80.9	6.22	5.475	5.575
EM_3	75.7	6.36	-5.525	-5.725
EM_4	77.2	6.1	-5.625	5.575

An experimental study was conducted to verify the spatial accuracy of 2D peak-MFD scanning for the illustrative example in Fig. 5-5. The 6-by-6 EM array is utilized to transduce the N_{fx}×N_{fy} segmented image as shown in Fig. 5-5(a) (N_{fx}=N_{fy}=501 pixels). Area 16 in the range of EM_{14}, EM_{15}, EM_{24}, EM_{25} is discussed in this example. 35 points in the path of the segmented image are chosen to scan in Fig. 5-5(b). The origin of x_r-y_r coordinate is the average x_r, y_r values of four EM centers. The resolution of the 35 points is 0.25mm (N_{sx}=N_{sy}=45). Two input current manipulation methods mentioned in the inverse model are validated. The first method is assumed that all EMs have the same B_0 and σ values and use the exact analytical solution to solve a_x and a_y by Eq. (5.2). The value of B_0 in this

experiment is the average value of B_{0i}, i=1~4. The input currents of four EMs can be multiplied by the ratios of B_0/B_{0i} to compensate the MFD peak value to B_0. The value of σ is the average value of σ_i, i=1~4. The value of υ uses the ideal value (5.5 mm). The second method is to substitute the real values (B_{0i}, σ_i, υ_{xi}, υ_{yi}, i=1~4) into Eq. (5.1) and solve the

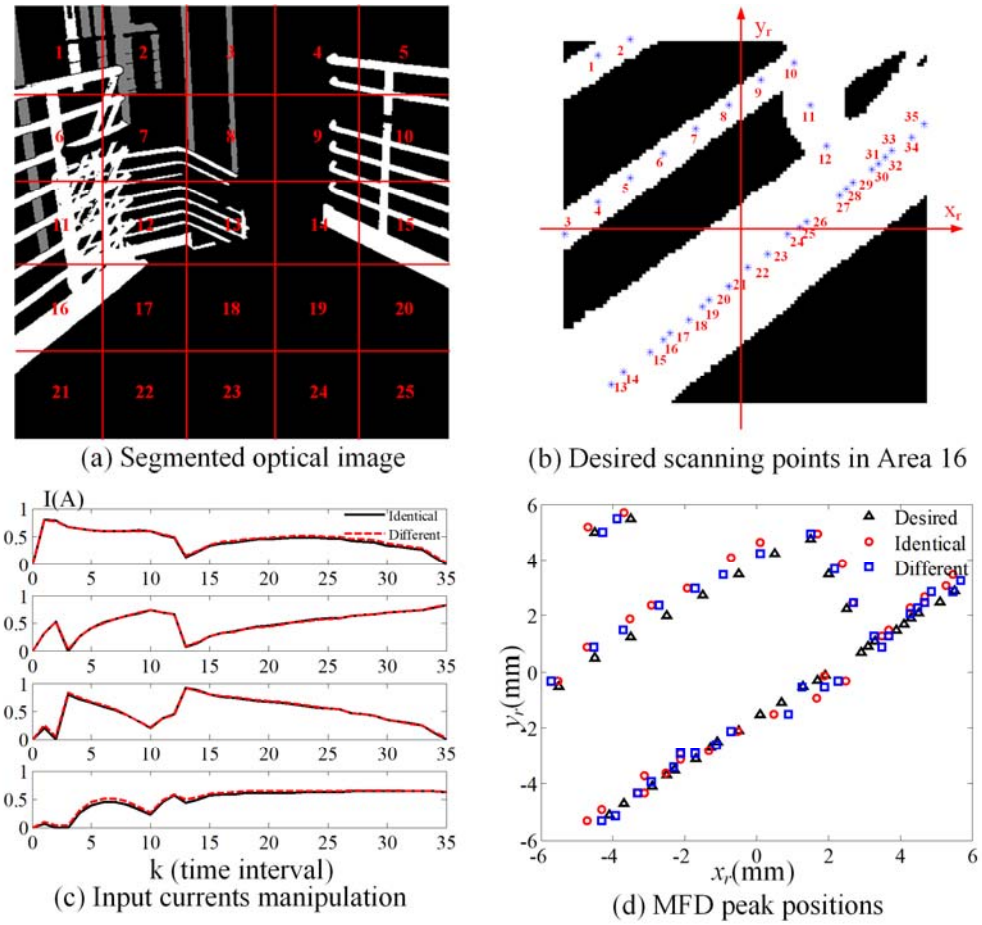

Figure 5-5 Magnetic scanning example

values of a_x, a_y numerically. The desired MFD peak value (B_d) is set as the average of B_i, i=1~4, which is equal to 80.55 μT. After a_x, a_y are obtained, the input currents of four EM can be determined by Eq. (2.2). The manipulated input currents for these 35 points of two methods is shown in Fig. 5-5(c). The experimental results of peak positions are shown in

Fig. 5-5(d). The errors of MFD peak measurements are shown in Table 5-5. The results show that the method to consider different parameters of each EM has smaller mean and variance errors than use the identical parameters. The *z*-component MFD distribution of the synthetized MFD of the 2-by-2 EM when scanning at point 14, 23, and 34 are demonstrated in Fig. 5-6. The measuring range is from -15mm to 15 mm both in x_r, and y_r directions. The measuring interval is 1 mm. Table 5-6 shows the desired/measured peak positions, values and corresponding input currents.

Table 5-5 MFD peak measurement error (mean, variance)

	MFD peak position		MFD peak value	
	mean(mm)	variance(mm^2)	mean(μT)	variance(μT^2)
Identical	0.6107	0.0543	-3.1194	1.5766
Different	0.4895	0.0509	-2.0918	0.965

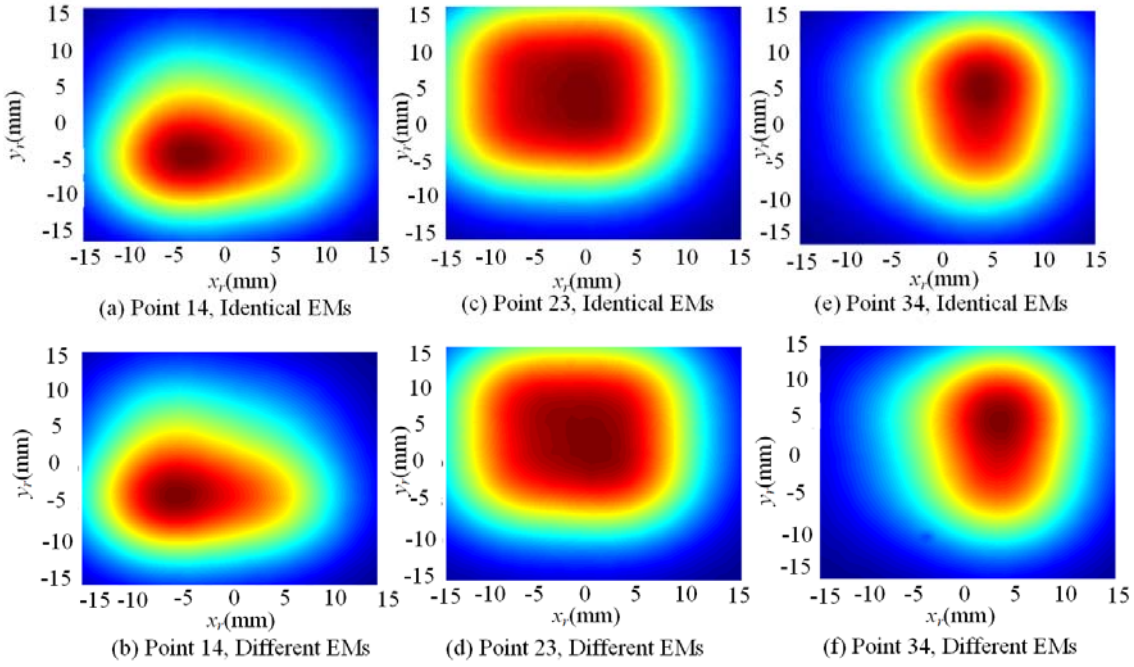

Figure 5-6 MFD distribution

Table 5-6 MFD peak measurement error

	Peak position (x, y) (mm)		**Peak value** (μT)	**Input current** (A)
	Desired	Measured	Measured	(I_1,I_2,I_3,I_4)
P14(I)	(-3.7, -4.7)	(-4.3, -4.9)	78.84	(0.231,0.145,0.868,0.492)
P14(D)		(-3.9, -5.1)	80.37	(0.248,0.155,0.867,0.54)
P23(I)	(1.9, -0.1)	(2.5, -0.3)	75.85	(0.472,0.571,0.57,0.62)
P23(D)		(2.3, -0.3)	77.35	(0.505,0.564,0.575,0.642)
P34(I)	(5.1, 2.5)	(5.3, 3.1)	78.68	(0.121,0.788,0.11,0.643)
P34(D)		(5.5, 2.9)	79.06	(0.148,0.792,0.103,0.616)

Eddy-Current Scanning Motion Experimental Validation

Figure 5-7(a) shows the configuration of MFD measurement to verify the ECD movement. The exciting frequency (f) is 2 kHz, the plate thickness (h_p) is 1mm, the measuring distance (h_m) is 14 mm, and the plane distance (h_c) is 11mm. Figure 5-7(b) demonstrates the exciting currents of PI14(I), PI23(I), PI(34) amplitudes of 2 kHz frequency.

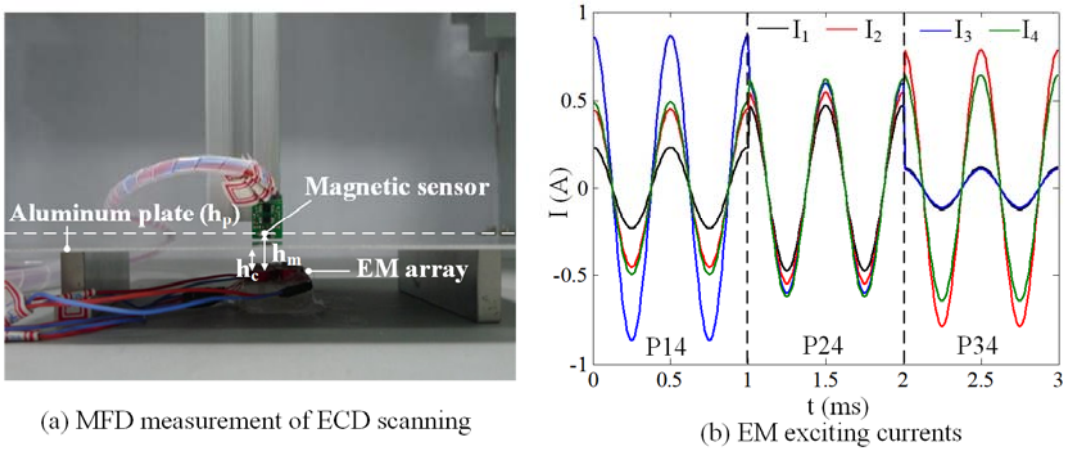

(a) MFD measurement of ECD scanning

(b) EM exciting currents

Figure 5-7 MFD measurement of EM exciting currents

The measuring normalized real part MFD for three points (P_{14}, P_{24}, P_{34}) of two methods are shown in Fig. 5-8, 9, where the MFD images generated by the eddy-currents are obtained by subtracting the MFD image with Aluminum (the left column of Fig. 5-8, Fig. 5-9) from the MFD image in free space (the middle column of Fig. 5-8, 5-9). The measuring range is -15 mm to 15 mm with the interval 1mm. The right column of Fig. 5-8, 5-9 show the MFD distribution generated by the eddy-currents of the three points.

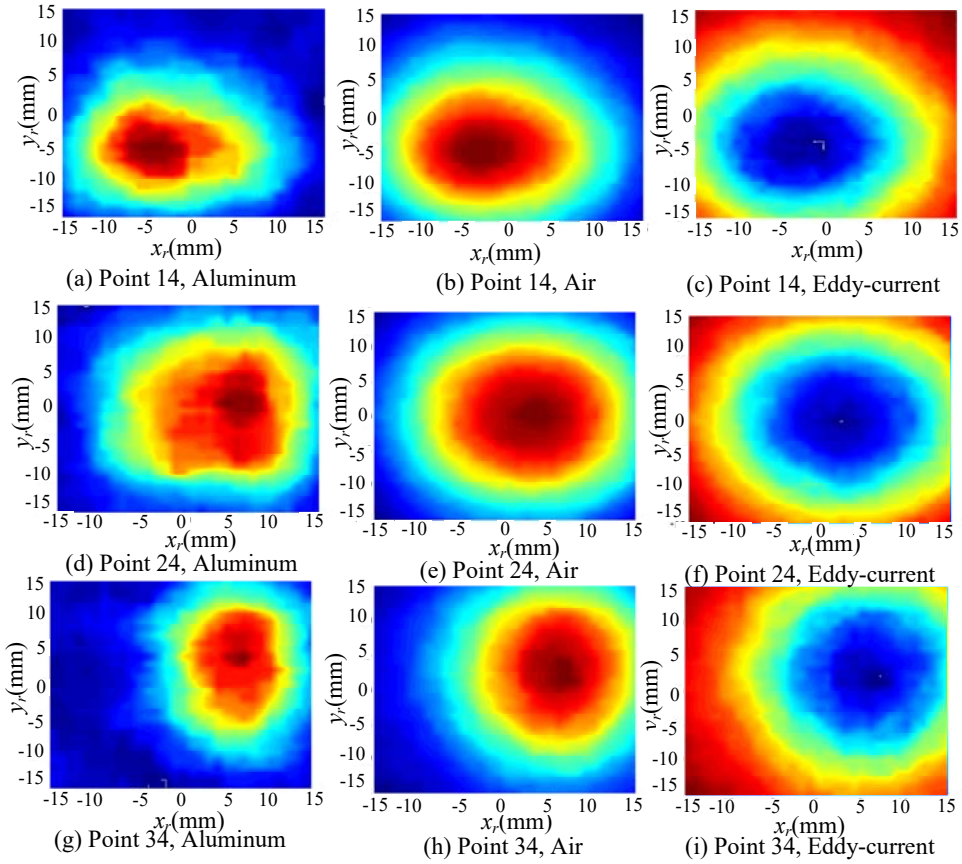

Figure 5-8 ECD scan measurement (identical)

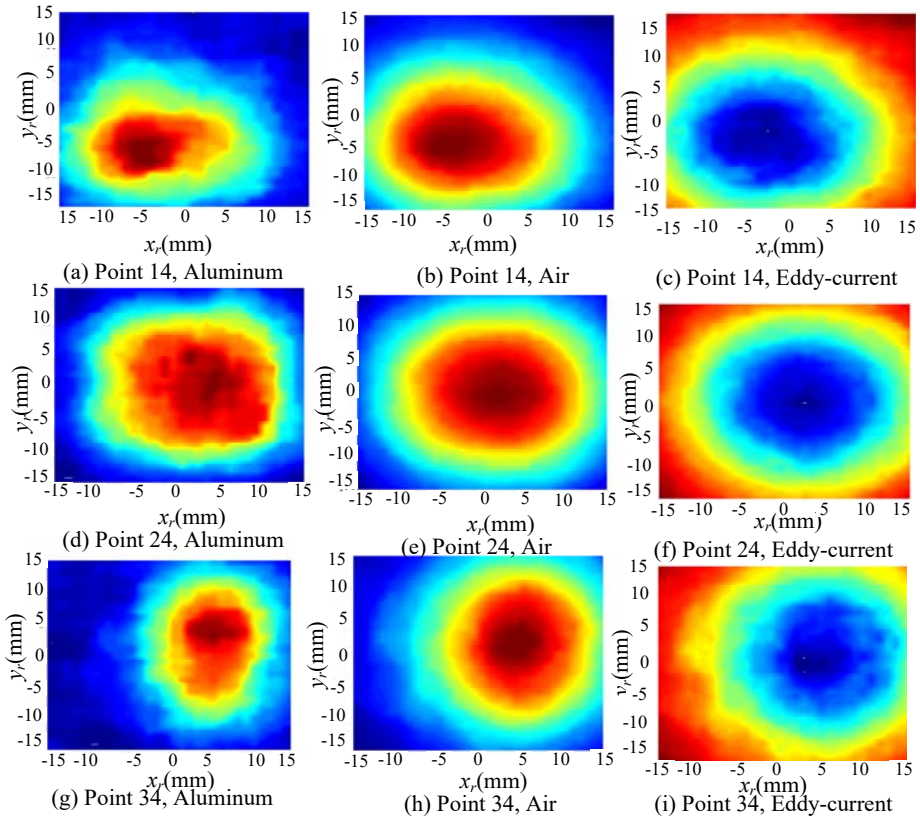

Figure 5-9 ECD scan measurement (different)

5.2 Electrical Muscle Stimulation

The effects of the field scanning method on biological tissues have been investigated experimentally using electrical muscle stimulation. The experimental parametric values are bases for the numerical models.

Conducted at the State Key Laboratory of Digital Manufacturing Equipment and Technology of Huazhong University of Science and Technology, Fig. 5-10 is the RehaStimTM Stimulation experiment setup for muscle electrical stimulation (with 1mm-diameter electrodes) using a single electrode (Fig. 5-10a) and four electrodes (Fig. 5-10b). To demonstrate the effect of muscle stimulation, green stickers are attached on the ring

finger and a color tracking algorithm is utilized for finger tracking. Fig. 5-10(c) is the waveform of the biphasic wave generated by the RehaStimTM Stimulation device. Fig. 5-10(d) are the finger tracking results.

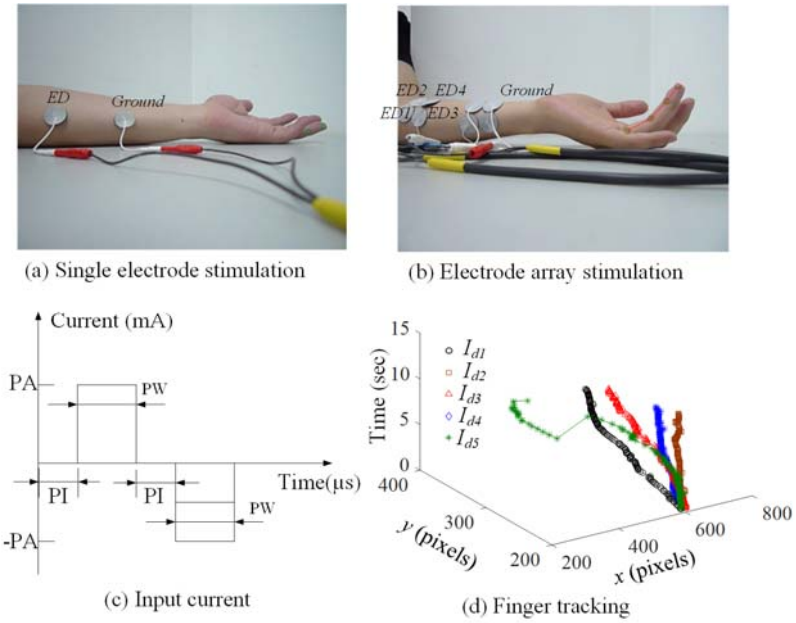

Figure 5-10 Muscle electrical stimulation experiment

The input current values of four electrodes are shown in the left column of Table 5-7.

Table 5-7 Experimental and simulation parameters

	Current amplitude (mA)				Simulation parameter	
	PA_1	PA_2	PA_3	PA_4		
I_{d1}	3	0	0	0	PW (μs)	150
I_{d2}	0	3	0	0	PI (μs)	100
I_{d3}	0	0	3	0	Period (μs)	500
I_{d4}	0	0	0	3	σ (S/m)	0.3
I_{d5}	3	3	3	3	ε_r	2×10^5

The input currents of the electrodes are 3mA for each electrode and 3mA for all electrodes. The right column of Table 5-7 are the experimental and simulation parameters. PA is the pulse current amplitude, PW is the pulse width, and PI is the pulse interval. The period is 500 μs, corresponding to 2kHz. The electrical conductivity (σ) and relative permittivity (ε_r) of the muscle are obtained by searching the values of conductivity and permittivity curve at 2kHz in [77]. Fig. 5-11(a) is the flowchart of the color-based tracking method. First, the pixels in R, G, B coordinate are converted to L, a, b coordinate.

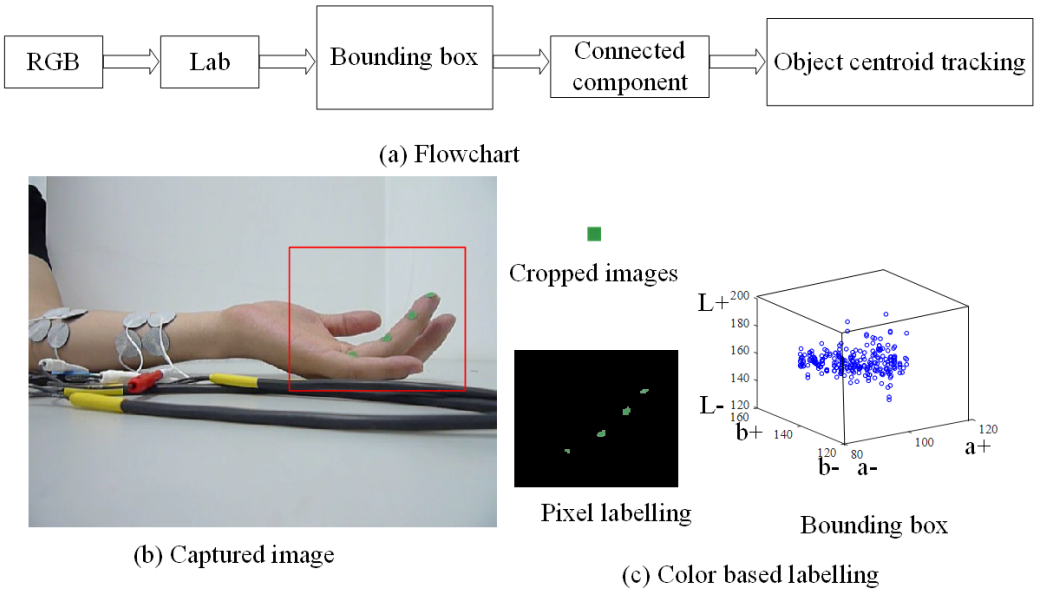

Figure 5-11 Color-based image tracking method

The range of L, a, b can be determined off-line by reading the cropped image. The boundary values can be determined by Eq. 5.4. $L_{I\pm}$, $L_{a\pm}$, $L_{b\pm}$ are the boundary values in L, a, b coordinate. L_{I_max}, L_{a_max}, L_{b_max}, L_{I_min}, L_{a_min}, L_{b_min} are the maximum and minimum values. L_{I_μ}, L_{a_μ}, L_{b_μ} are the mean values. k_L is the constant value to adjust the bounding box size. Fig. 5-11 (b) shows the captured image. The green stickers are attached on the ring finger. Fig. 5-11(c) shows the steps of this tracking algorithm. The pixels of the

cropped images of the green stickers are converted to L, a, b coordinate and the upper and lower boundary L, a, b values can be determined by Eq. (5-4). The pixels in the captured images in the range of L, a, b bounding box can be extracted and the connected component method can be applied to label the objects for tracking the centroids of the objects.

$$\begin{aligned} L_{I\pm} &= L_{I\mu} \pm k_L (L_{I\_\max} - L_{I\_\min}) \\ L_{a\pm} &= L_{a\mu} \pm k_L (L_{a\_\max} - L_{a\_\min}) \\ L_{b\pm} &= L_{b\mu} \pm k_L (L_{b\_\max} - L_{b\_\min}) \end{aligned} \tag{5.4}$$

Fig 5-11(d) is the tracking result of the stick on the ring finger, where the pixels size of the cropped image is 10×10 pixels, and K_L is 0.25. Different stimulating amplitudes lead to different trajectories. When all electrodes turn on (Id_5), the ring finger has largest movement. The DPE method is utilized to simulate the electric field distribution of the muscle. Two cases are utilized to discuss: Case A: A single electrode stimulation (I_{d1}) in Table 5-7, and case B: the electrical stimulation of all electrodes (I_{d5}). Fig. 5-12 shows the configuration of simulation model of the arm. 20×6×4 elements are used in the simulation as shown in Fig. 5-12(a). Fig. 5-12(b) is the plane view of case A.

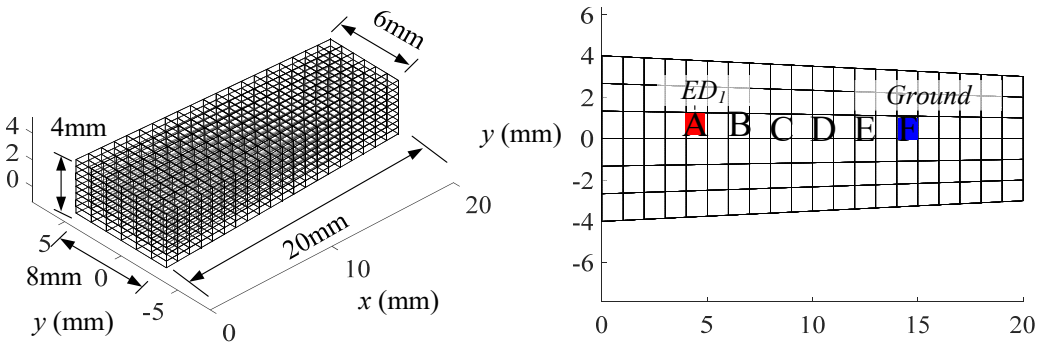

(a) Simulation configuration

(b) Plane view

Figure 5-12 Simulation parameters

The quadrilateral at point A is the electrode, and the quadrilateral at F is the ground. Fig 5-13(a), (b) are time response of element A to D of the first and second layer with time interval 1 μs by using Eq. (3.9). The elements close to the electrode and the surface has larger exciting amplitude. Fig 5-13(c), (d) are the electrical potential of first and second layer elements at t=200, 255, 400 μs. Fig. 5-13(e) is the electric field which can be determined by Eq. (4.2a), Eq. (4.2b). Fig. 5-14 shows the configuration and simulation results of case B. Comparing Fig. 5-13(c), (d) with Fig. 5-14(e), (f), the variation of maximum values of A and F of case B is larger than case A. Comparing Fig. 5-13(a), (b) with Fig. 5-14(c), (d), the range of peaks in case B is larger than A. As shown in Fig. 5-13(e) with Fig.5-14(b), the electric field is more intense in case B. As mention above, the stimulation by the electrode array causes larger electrical potential at the stimulating point.

In [29], the second derivative electrical potential (d^2V/dx^2) equaled to the first derivative electric field (dE_x/dx) is called the activating function. It responses for the excitation models for external stimulation of the nerve fiber, where x is the direction along the membrane. Fig. 5-15 (a) and (b), and 5-16 (a) and (b) are electric and the first derivative electric fields of the elements in the first layer. Fig. 5-15 (c) and (d) and 5-16 (c) and (d) are the values of elements along the red dotted line in Fig. 5-15(a). The simulation results show that the stimulation by the electrode array leads larger activating function values.

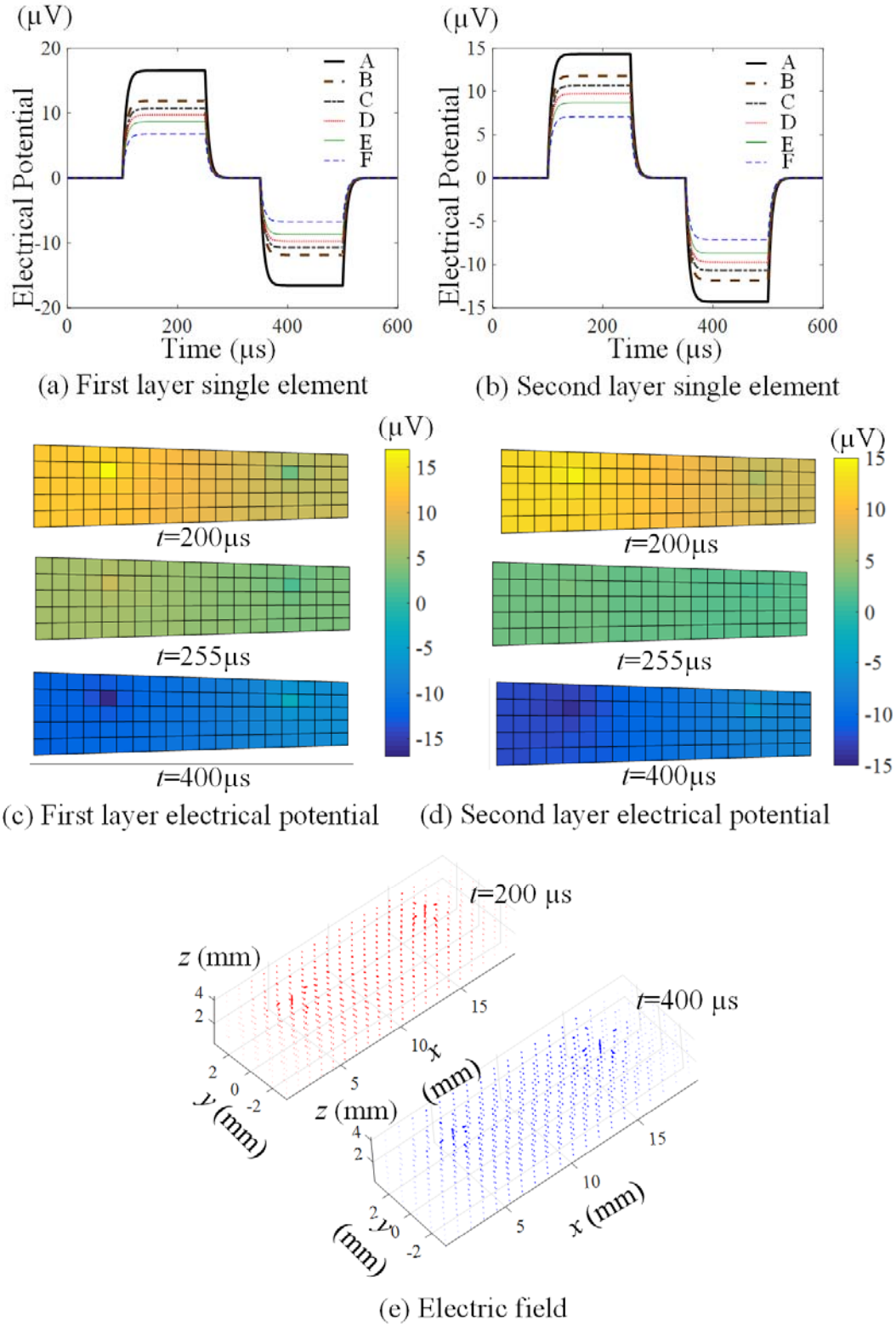

Figure 5-13 Case A: Single electrode stimulation result

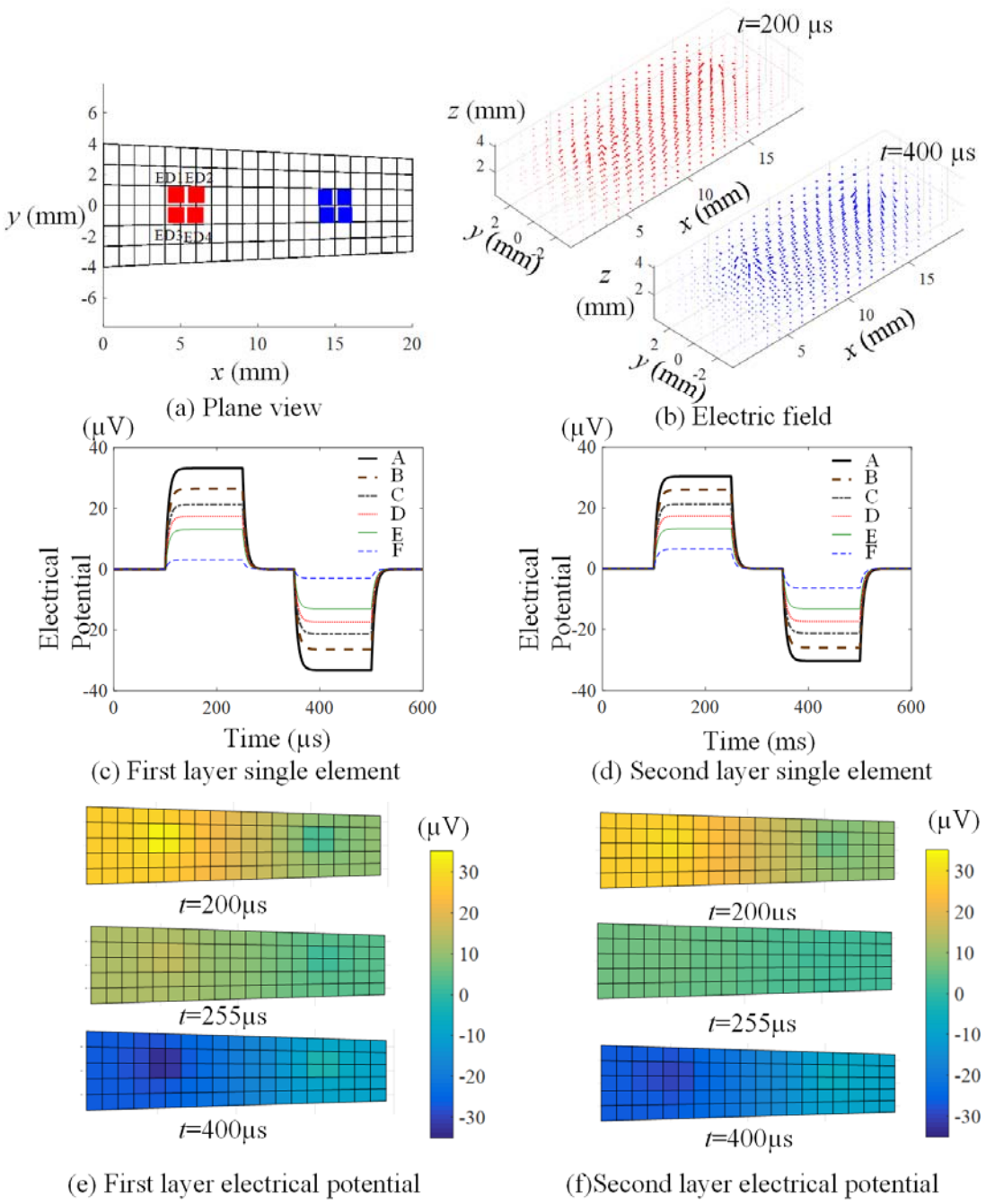

Figure 5-14 Case B: An electrode array configuration and stimulation results

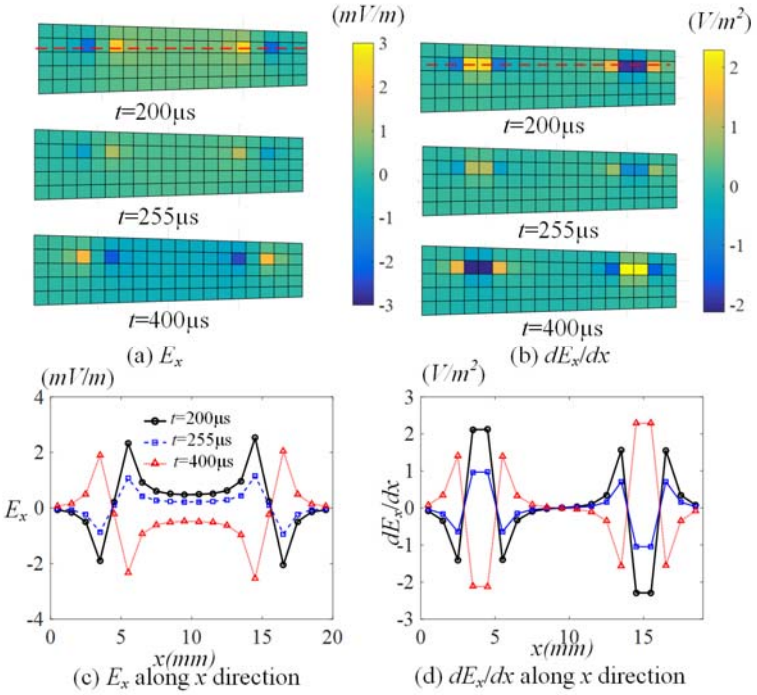

Figure 5-15 Electric and first derivative electric field of single electrode

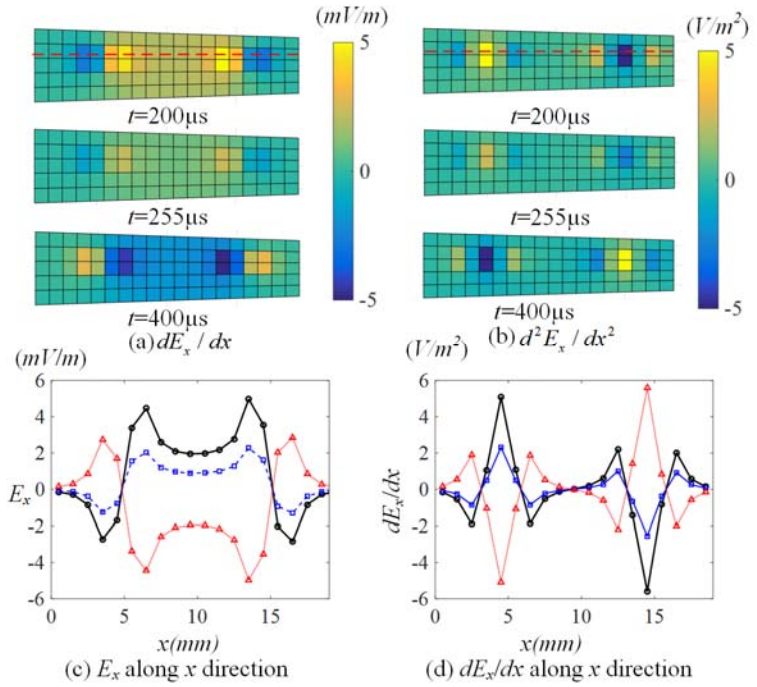

Figure 5-16 Electric and first derivative electric field of electrode array

5.3 DPE Model Validation of induced ECD and its MFD

Three experiments were conducted to validate the DPE model and evaluate the MFD-based eddy-current (EC) sensor system. The *first* experimentally validates the axisymmetric DPE model by comparing with the measured magnitude/phase of the MFD generated by the induced ECD in a 24mm-diameter 5.38mm-thick annular copper that has an electrical conductivity σ=58.4 MSiemens/m (or MS/m). The *second* investigates the boundary effects on the measured MFDs as the ECD sensor horizontally scans across an edge of an Aluminum plate. The *third* demonstrates the DCS method for modeling an ECD and measuring its MFD.

5.3.1 Experimental Setup

The experimental setup to verify the MFD measurement is shown in Fig. 5-17. The EC sensor is positioned by a three degree-of-freedom (DOF) precision translation stage with a laser-sensor above the test-sample. The test-sample relative to the magnetic sensor can be fine-tuned by three micrometers and the laser-sensor so that it is parallel to the sensor *xy*-plane. A pair of commercial (HMC1051) anisotropic magnetic resistance (AMR) sensors $S_{\pm}$ housed in the EM was used to measure the *z*-MFD from which the contribution of the pre-calibrated EM was subtracted from the measurements. As shown in Fig. 5-17(c), the AMR sensors are symmetrically placed near the outer radius of the coil where its *z*-MFD is minimum to avoid sensor saturation. Fig. 5-17(e) schematically illustrates the overall system dynamics, where the EM/conductive-plate system dynamics can be determined by the model in terms of the parameters (Δ, z_p, h_p). The sensor dynamics (contributed by the signal processing amplifiers and associated circuits) are accounted for

the transfer function $G_s(j\omega) = |G_s(j\omega)| \angle G_s(j\omega)$ in the 2nd block. The sensor system dynamics were determined to be 1.33 and –0.014° using a least-square (LS) method. The parametric values of the EM, test samples and AMR sensor specifications, along with the operating frequencies, are detailed in Table 5-8.

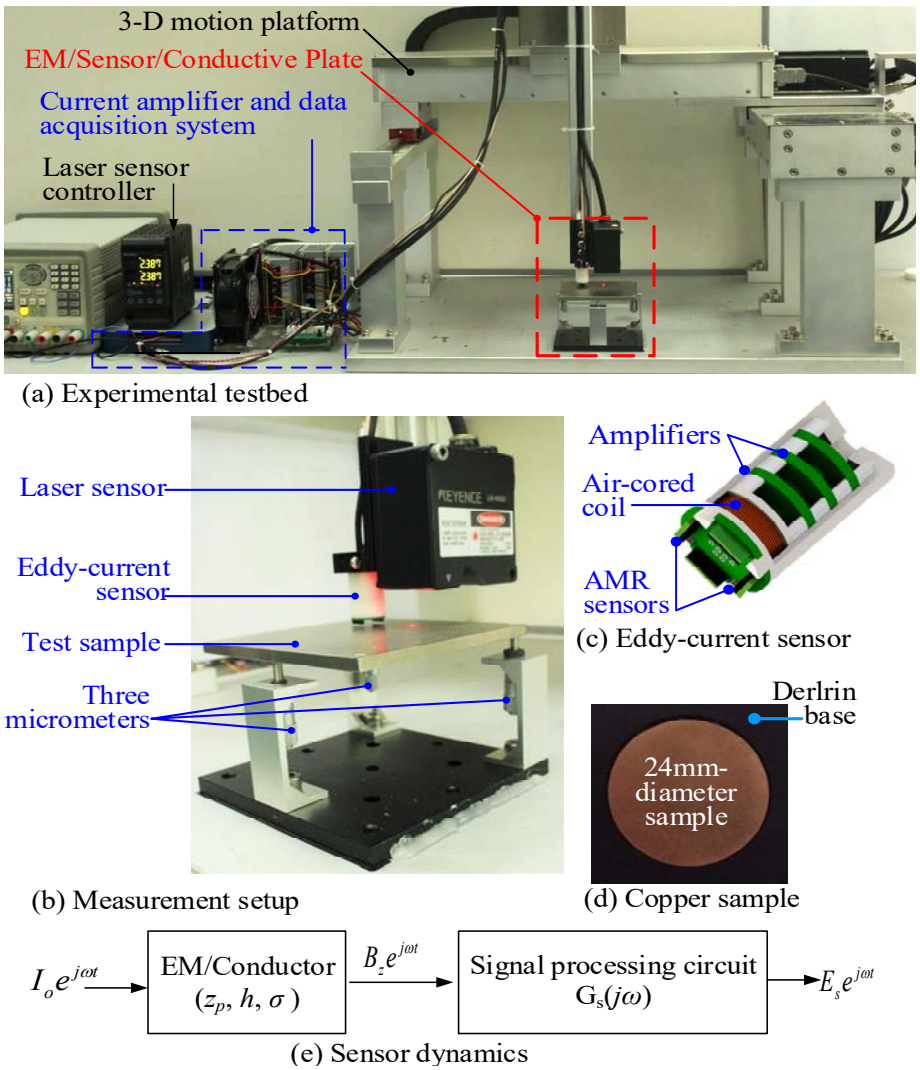

Figure 5-17 Experimental setup

Table 5-8 Parametric values of experimental setup

<table>
<tr><td colspan="2">EM Coil (N_w = 60, d_w = 0.35 mm)
(a_i, a_o, a) = (3.75, 6, 2) mm
I_o=1A, B_o= 16.67 μT</td><td>AMR Sensor (HMC1051ZL)
Size: 6.5×1.7×2.0 mm
$S_{\pm}$ (x_s, y_s, z_s): (±6, 0, –4.5) mm</td></tr>
<tr><td colspan="3">Sensor system dynamics: $|G_s(j\omega)|$ = 1.33, $\angle G_s(j\omega)$ = –0.0141°</td></tr>
<tr><td>Copper (Cu)
σ = 58.4 MS/m
h = 5.38 mm
f=100Hz – 25kHz</td><td>Titanium (Ti)
σ = 0.59 MS/m,
h=5.013 mm
f=10 – 25 kHz
z_p=6.5, 7.5, 8.5, 9.5 mm</td><td>Aluminum (Al)
σ=35.5 MS/m
h = 1 mm; d_h = 6, 12, 15 mm
f = 1 kHz
z_p=6.5 mm</td></tr>
<tr><td colspan="2">Edge scan w_p = 48 mm
Number of elements: 576</td><td>Hole scan w_p = 72 mm
Number of elements: 769, 670, 689</td></tr>
</table>

As shown in Figs. 5-17(a, b), the EC sensor is positioned by a three degree-of-freedom (DOF) precision translation stage with a laser-sensor above the test-sample. The test-sample relative to the magnetic sensor can be fine-tuned by three micrometers and the laser-sensor so that it is parallel to the sensor *xy*-plane. A pair of commercial (HMC1051) anisotropic magnetic resistance (AMR) sensors $S_{\pm}$ housed in the EM was used to measure the *z*-MFD from which the contribution of the pre-calibrated EM was subtracted from the measurements. As shown in Fig. 5-17(c), the AMR sensors are symmetrically placed near the outer radius of the coil where its *z*-MFD is minimum to avoid sensor saturation. Fig. 5-17(e) schematically illustrates the overall system dynamics, where the EM/conductive-plate system dynamics can be determined by the model in terms of the parameters (Δ, z_p, h_p). The sensor dynamics (contributed by the signal processing amplifiers and associated circuits) are accounted for the transfer function $G_s(j\omega) = |G_s(j\omega)| \angle G_s(j\omega)$ in the 2nd block. The sensor system dynamics were determined to be 1.33 and -0.014° using a least-square (LS) method. The parametric values of the EM, test samples and AMR sensor specifications, along with the operating frequencies, are detailed in Table 5-8.

5.3.2 Experimental Result

The results for the three experiments are summarized in Figs. 5-18, 5-19 and 5-20.

Harmonic Analysis of the 2D Axisymmetric Model

Figure 5-18 shows the effects of the normalized skin-depth Δ defined in Eq. (3.29) and the normalized EM-plate distance Z_p on the ECD-generated MFD computed using a 2D axis-symmetrical DPE model with two different types of grid divisions; uniform grids and refined grids based on equal current density. To provide quantitative comparisons, the computed results are compared with experimentally measured magnitudes and phases of the copper sample shown in Fig. 5-17(d). As shown in Fig. 5-18, the magnitudes (left plot) depend on both Δ and Z_p but the phases are insensitive to Z_p. The % mean-squared-errors (MSEs) of the magnitudes computed using uniform and refined grids (relative to measurements) are 1.11×10^{-4} and 1.62×10^{-7} respectively. The corresponding MSEs of the phases are 0.0012 and 4.1712×10^{-4}. The discrepancies in the uniform DPE grids primarily occur at small Δ, where the refined grid method plays an important role to improve the computational effectiveness. Validated with experiments conducted on the two materials (copper and titanium alloy), the results confirm that the EC-induced and its corresponding MFD depends only on the normalized skin-depth (regardless of materials) for the specified pair of (H, Z_p) *Boundary Effects on the Model*

Figure 5-19(a) shows the state-space solutions of the eddy current field for experimentally investigating the edge effects on the MFDs measured by the pair of AMR sensors $S_{\pm}$ as the EC sensor moves horizontally across the Al plate from $X = -4$ to $X = 4$. .

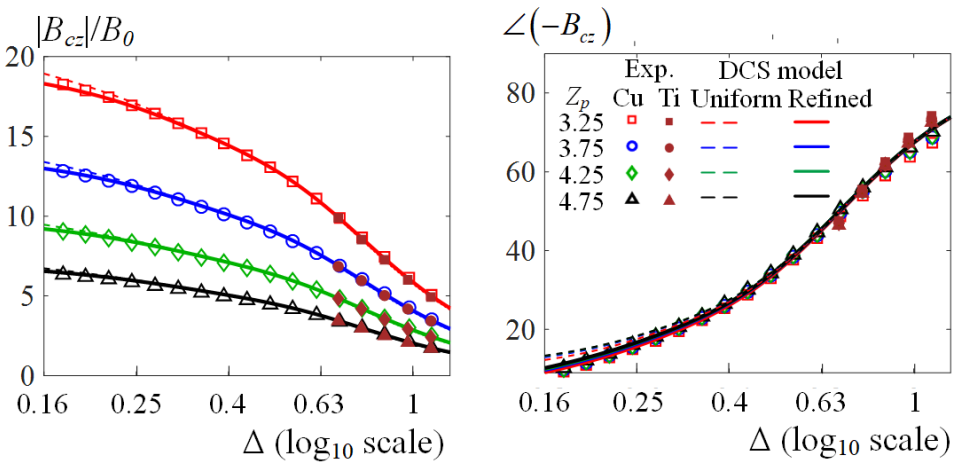

Figure 5-18 Experimental verification of the model (single AMR)

The simulated and measured real and imaginary parts are compared in Fig. 5-19(b), and replotted in magnitudes and phases in Fig. 5-19(c).

To facilitate discussions, the path is divided into four stages:

- Stage I $(X<-1)$: EM is outside the plate as S_+ approaches its left edge. No apparent edge effects are observed.
- Stage II $(-1\le X<0)$: Less than half of the EM is above the plate. S_+ is above the plate. A sharp sign change in phase can be observed in S_- as the EM center approaches the left edge of the plate.
- Stage III $(0\le X<1)$: More than half of the EM is above the plate as S_- approaches its left edge with S_+ above the plate.

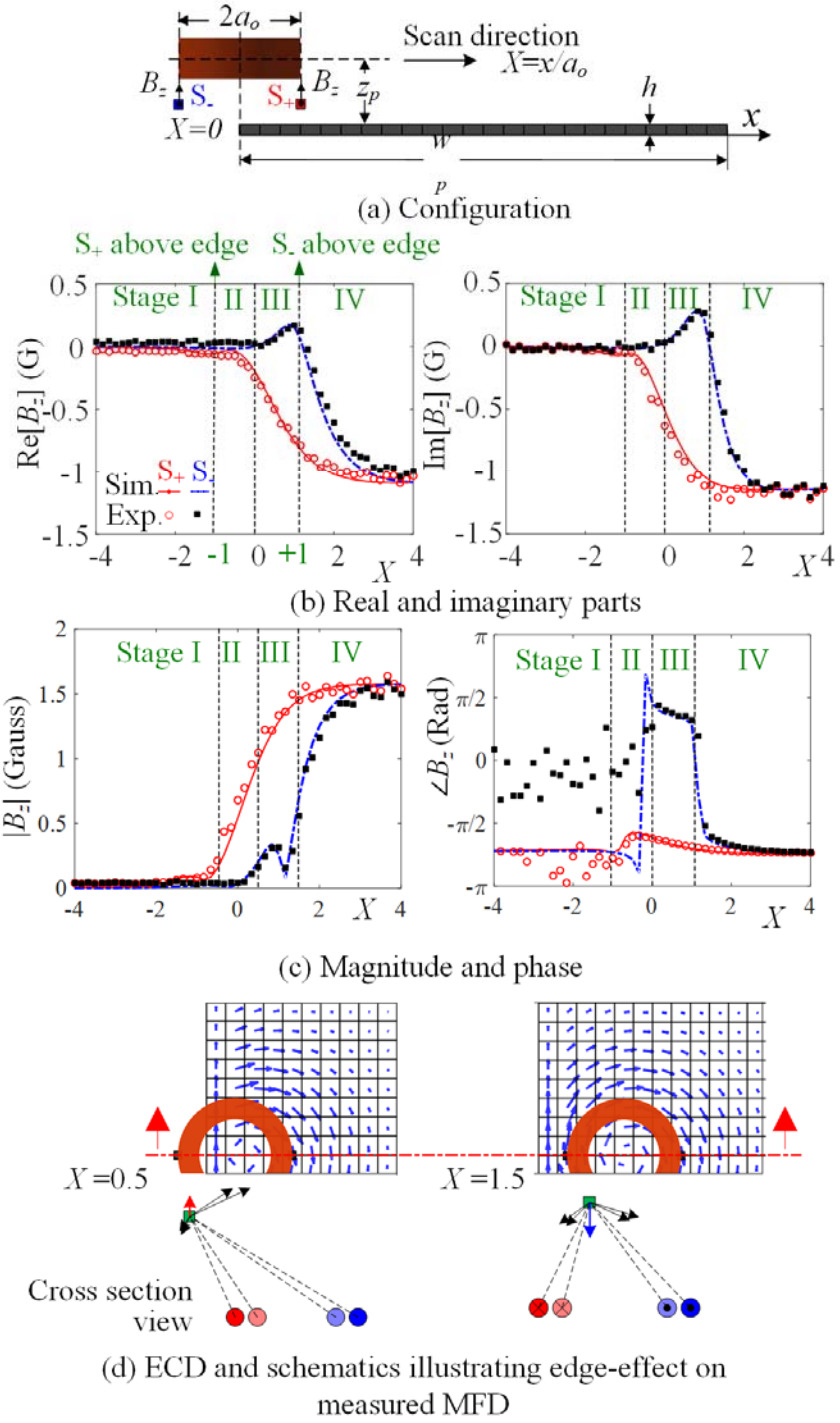

Figure 5-19 Effect of edge boundary on z-component MFD

– Stage IV $\left(0 \le X < \frac{w_p}{a_o} - 4\right)$: EM (with both $S_{\pm}$) is completely above the plate. Because the magnitudes in Stages I and II are infinitesimally small, the corresponding phases are difficult to measure accurately and the experimental phase data are ignored. Some intuitive insights can be gained from

– Apparent edge effects slowly disappear as the EM moves away from the edge.

Because the magnitudes in Stages I and II are infinitesimally small, the corresponding phases are difficult to measure accurately and thus the experimental phase data are ignored. Some intuitive insights can be gained from Fig. 5-19:

– As compared in Fig. 5-19(b) that graphs their real and imaginary parts, the measured MFDs agree well with the simulation validating the model.
– The AMR sensor S_+ registers a smooth S-shape curve. However, a peak near $X = 1$ can be observed in both the real and imaginary parts in the S_- measurements.
– The phenomena of the S_- measurements can be explained with the aid of Fig. 5-19(d): As S_- approaches the edge from the far left, the measured B_{cz} is positive primarily contributed by the positive EC (+y direction in the cross sectional view) and increases until S_- is at the edge. As S_- passes the edge, the negative EC increases its contribution to the measured B_{cz}, which cause the measured B_{cz} to change from positive to negative. This explains why the phase change happens when S_- is directly above the edge, which is a meaningful phenomenon for edge detection.
– The above findings demonstrate that the sensor placement plays an important role in the sensor design for localization or for edge detection.

Geometrical Effects on ECD and its corresponding MFD

Fig. 5-20 illustrates the solutions to the models in state-space representation for analyzing the M/EC fields of a plate that has a through hole (diameter d_h). The relatively complicated shape of the plate/hole configuration was geometrically modeled using a commercial CAD software Solidworks, and then discretized using a mesh generation software to create divisions (represented by nodes and elements) of irregular hexahedrons. Fig. 5-20(a) shows a typical hexahedron where the volume, areas and surface normal are given in Appendix B for completeness. Figures 5-20(b) and 5-20(c) show the typical DPE modeled EC fields induced in the plate when the EM is above the hole-center and at an offset along a radial path. Figures 5-20(d) to 5-20(f) compare the measured and simulated MFDs when the EC sensor swept over the hole (d_h = 6, 12, 15mm) along a radial path.

- The experimental curves share similar trends with the simulation. The curves obtained from two AMR sensors are approximately symmetric about $X = 0$.
- Unlike Fig. 5-20 where S+ registers a smooth S-shape magnitude curve between X=-1 and 1, S+ experiences a local peak as it moves pass the edge of a hole. The shape of the magnitude curve around the peak depend on d_h/a_o.
- The resolution of the meshes could have a significant effect on numerical error. This numerically illustrated in the zoom-in Fig. 5-20(g) where (3, 2.5 and 2) denote the three approximate global element-sizes in mm corresponding total numbers of elements (689, 938 and 1525). Due to the symmetry, the effects on the MFDs measured by S_+ were

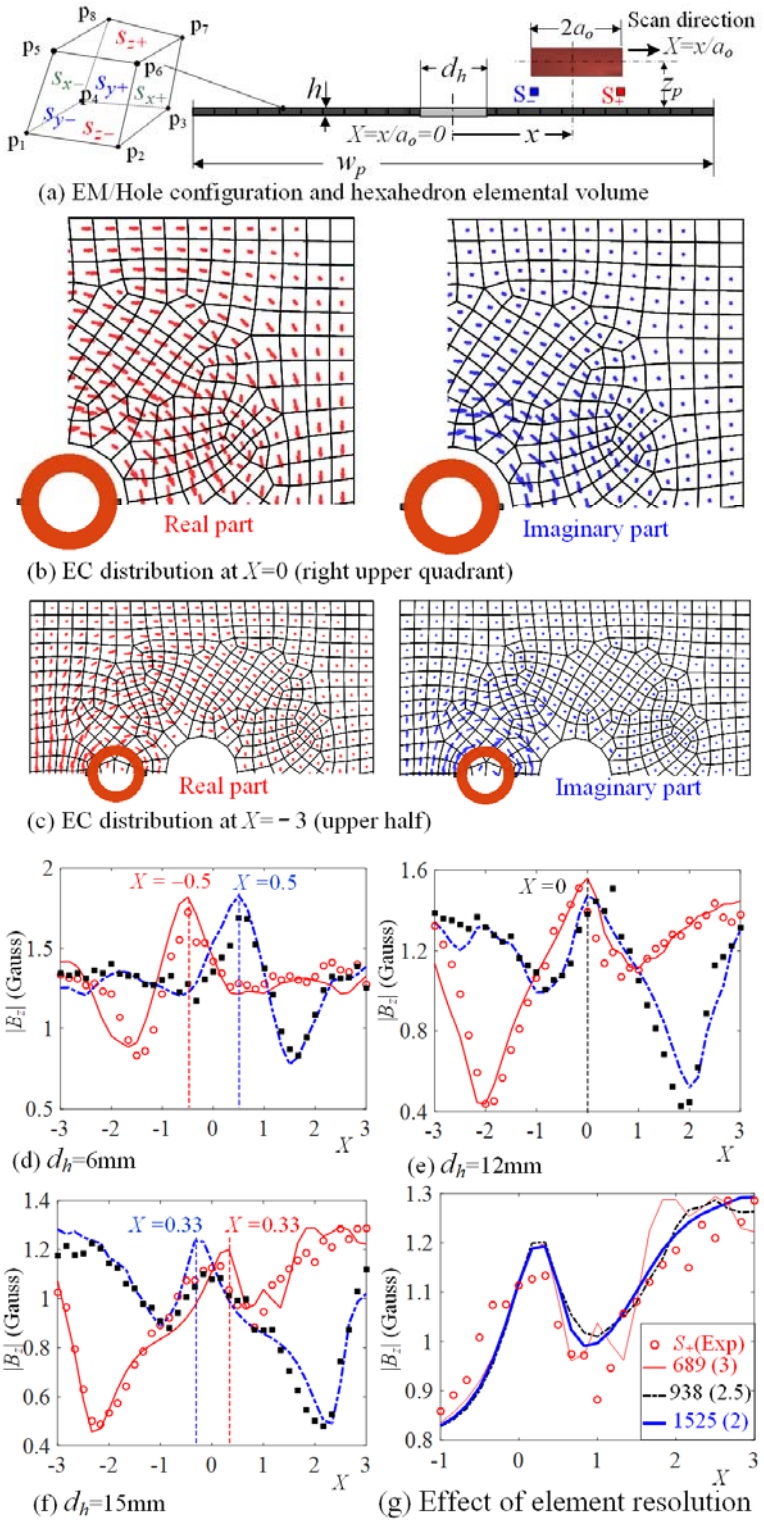

Figure 5-20 Effect of hole on ECD and z-component MFD

compared. As shown in Fig. 5-20(g), the local noisy peaks disappear when the meshes are sufficiently fine.

– The results show that the peaks of the three curves are at $X = -0.5$, 0 and 0.33 respectively, which correspond to the locations when S_+ is directly above the edge of the hole. The close agreements between the measured and simulated MFDs validate the DPE methods, and demonstrate its effectiveness for analyzing the M/EC fields of a configuration with a relatively complicated shape.

5.4 Summary

This chapter demonstrates three experiments to verify and validate the method in chapter 2 and 3. First, the 1D and 2D M/EC scanning methods are verified. Experiments results show that the z-component of the MFD generated by a cylindrical air-cored EM can be well characterized by a Gaussian approximation, and maximum error between specified and measured positions is within 4% demonstrating the high accuracy of non-mechanical 1D peak-MFD scanning. Second, an experiment of muscle electric stimulation by an electrode array with the visual tracking is utilized to demonstrate the scanning method for biological tissue stimulation. The time-dependent electric field of a biphasic wave stimulation is simulated by the DPE method to analyse the relationship between the electric field distribution and muscle contraction. Third, the DPE based EC models and their applications have been evaluated experimentally using measured MFDs, which involve three materials (copper, aluminum and titanium), and three object configurations (a semi-infinite conducting slab, an edge model and a plate with a through hole). The close agreements between the DPE method and experiments confirm that the method is capable

of handling the boundary effects of the object with complicated shapes, and offering high-fidelity physically intuitive predictions without sacrificing technical details.

CHAPTER 6. CONCLUSIONS AND FUTURE WORKS

6.1 Conclusions

A new actuating method utilizing the magnetic field as media has been presented, which enables manipulation of relatively high-resolution eddy-current patterns with a relatively small number of electromagnets along with the development of the distributed parameter element (DPE) method for design analysis of alternative perception and non-destructive testing applications. The following summarizes the contributions made in this thesis.

1. A continuous-field actuation method

A method for converting an optical color image to magnetic/eddy-current patterns which includes eddy-current density formulation, input current manipulation, and color-based image segmentation has been presented. The method can accurately control the synthetized magnetic/electric fields between adjacent EMs, which has been experimentally verification of its spatial accuracy of the 1D and 2D peak-MFD scanning. The use of magnetic and eddy-current scanning for a potential retinal prosthesis application was demonstrated numerically.

2. The distributed parameter element (DPE) method

The two or three-dimensional irregular shape physical fields have been formulated in state-space representation where the divergence theorem is applied on each element to satisfy the conservation law and boundary conditions to account for the object geometry.

This formulation provides a basis for the subsequence stationary, time dependent, and harmonic analysis of the physical field.

3. The artificial perception applications

Two examples have been illustrated to demonstrate the feasibility of utilizing the continuous-field actuation method for transducing optical color images for design analysis of some artificial perception applications. For the retinal stimulation simulation, a design concept to use the μ-EM array to transduce eddy-current patterns for retinal prosthesis is proposed and compared with the traditional electrical stimulation of μ-electrode array. The magnetic and electric fields of the biological tissues for the magnetic stimulation are formulated by the distributed parameter modeling method. Second, a muscle electric stimulation experiment by using an electrode array with the visual tracking is utilized to demonstrate the scanning method. The time-dependent electric field of a biphasic wave stimulation is simulated by the DPE method to analyse the relationship between the electric field distribution and muscle contraction. It is expected that the DPE method can be utilized in broad applications.

4. Eddy-current sensing in manufacturing applications

The DPE method for analyzing the magnetic and eddy-current fields of an eddy-current-based sensing system has been presented. The distributed EC modeling method and its applications have been evaluated experimentally using measured MFDs, which involve three materials (copper, aluminum and titanium), and three object configurations (a semi-infinite conducting slab, an edge model and a plate with a through hole). In addition,

the application of non-mechanical scanning method of an EM array for hole and edge detections are illustrated numerically.

6.2 Future Works

This thesis presented a physical field scanning method to transduce an optical color images to magnetic or electric patterns and distributed parameter modeling method for analyzing the corresponding magnetic and electric field. This research provides a foundation for the physical fields modeling based mechatronics system design. Future works are summarized as followed.

1) The magnetic and electric scanning method can be utilized in a broad spectrum of applications which include haptic devices, micro-robot manipulation, retinal prosthesis and nondestructive detection.
2) The DPE method can be extended to various physical fields, such as the heat transfer, solid mechanics, and fluids. This method can be applied not only a single physical field bust also multi-physical field coupling.
3) The DPE method can formulate the physical problem as an optimization problem for optimal design of the mechatronics system.

   The optimization and inverse problem can be formulated as

   $$\min \|\mathbf{x} - \mathbf{x}^*\|, \text{find } \mathbf{u}^*$$

   where $\mathbf{x}^*$ is the column vector of desired physical values and $\mathbf{u}^*$ is the column vector of element and boundary source values to be predicted.

APPENDIX A. ANALYTICAL SOLUTIONS

The analytical solutions of the ECD induced in the non-ferrous metallic plate and MFD in air are expressed by three non-dimensional parameters (Δ: skin dept, Z_p: lift-off distance, H: thickness) for skin depth, sensor-plate distance, thickness of the plate for facilitating to investigate the sensor plate system in [78].

Induced Eddy Current Density (ECD)

Figure A-1shows the CAD model of a Magnetic-field based Eddy-Current Sensor (MECS), and the 2D axisymmetric coordinate system, parameters and variables for modeling the sensor. In terms of the dimensionless parameters, the analytical solution describing the ECD ***J*** induced in the plate due to a harmonic-current-carrying EM with uniform current density J_o has been derived in widely accepted classical solutions [5] for an intermediate frequency range ($f \le 10^6$ Hz). For the large conductor ($a_o \ll w/2$), the induced eddy-current is 2D axis-symmetric:

$$\frac{J_A(R,\mathrm{Z})}{J_o} = \mathrm{j}\frac{2}{\Delta_1^2}\int_0^\infty \left\{ \int_{\rho,\psi}^{\psi} \varphi\beta_s(\varphi)d\varphi \right\} \chi(\psi)\, d\psi \tag{A.1}$$

where $\Delta_i = \frac{\delta_i}{a_o} = \frac{1}{a_o}\sqrt{\frac{2}{\omega\sigma_i\mu_i}}$

$$\chi(\psi) = \frac{\beta_1(\psi R)\left[D\left(Z_p-1\right)-D\left(Z_p+1\right)\right]\left[D_1\left(Z+Z_p+H\right)-1\right]}{\psi^2\left[\left(\psi+\psi_1\right)-\left(\psi-\psi_1\right)D_1\left(H\right)\right]}$$

$$D(L) = \exp\left[\psi_1\rho_a\left(Z+Z_p\right)\right]\exp\left(-\psi\rho_a L\right);$$

$$D_1(L) = \left(\frac{\psi_2-\psi_1}{\psi_2+\psi_1}\right)\exp\left(-2\psi_1\rho_a L\right)$$

and $\psi_i = \sqrt{\psi^2 + \mathrm{j}\left(\frac{2}{\Delta_i^2}\right)}$

$$J_A = \frac{C_E}{a_o a} I, \text{where } C_E = \frac{\pi}{\rho_a}\left[\frac{N_w D_w}{4(1-\rho_i)}\right]^2 \text{ and } D_w = \frac{d_w}{a_o}$$

The characteristic geometrical parameters of the EM are normalized to its outer radius a_o and half-length a as follows:

$$\rho_i = \frac{a_i}{a_o};\ \rho_a = \frac{a}{a_o};\ H = \frac{h}{a};\ Z_p = \frac{z_p}{a};\ Z = \frac{z}{a} \text{ and } R = \frac{r}{a_o} \tag{A.2}$$

To reduce the solutions to a tractable form, the conductive plate is discretized into n_v elements; each consists of an elemental eddy-current $\mathbf{j}_i$ flowing through area c_i (where i=1, 2…, n_v) as shown in Fig. A-1:

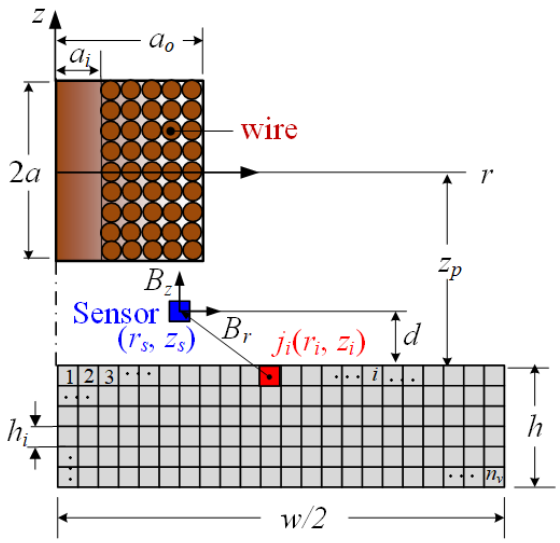

Figure A-1 Variables and parameters used in 2D axis-symmetrical modelling

In Eq. (A.1), σ_i (where i = 1, 2) are the conductivities of the 1st conductor with finite thickness h and the infinitely thick 2nd conductor; $\beta_s(\varphi)$ and $\beta_s(\psi R)$ are the first-order Bessel

equations; and δ_i is the skin-depth. Without loss of generality, the following discussion assumes a non-ferrous conductor ($\sigma_1\mu_1 = \sigma\mu$) in contact with non-conductor in air.

2D Axial-Symmetrical MFD Measurement Model

Given the current density, the MFD at any point k in the neighborhood of the conductor can be derived from the Biot-Savart's law. $\mathbf{B}_s(\mathbf{r}_k,t)$ can then be expressed in terms of discretized eddy-current as an output equation in Eq. (A.3) where $\mathbf{B}_{sc}$ and $\mathbf{B}_{se}$ are the MFD contributed by the induced eddy-current in the conductor and by the EM respectively:

$$\mathbf{B}_s(\mathbf{r}_\mathbf{k},t) = \begin{bmatrix} B_{sr} & B_{sz} \end{bmatrix}^{\mathrm{T}} = \mathbf{B}_{sc} + \mathbf{B}_{se} \tag{A.3}$$

$$\frac{\mathbf{B}_{sc}(\mathbf{r}_\mathbf{k},t)}{B_o} = \frac{1}{B_o}\begin{bmatrix} B_{cr} \\ B_{cz} \end{bmatrix} = \begin{bmatrix} \boldsymbol{\eta}_{cr}(\mathbf{r}_k) \\ \boldsymbol{\eta}_{cz}(\mathbf{r}_k) \end{bmatrix}\mathbf{I}_c(t) \tag{A.4a}$$

$$\text{where } \mathbf{I}_c = \frac{1}{I_o}\begin{bmatrix} \mathbf{j}_1 c_1 & \cdots & \mathbf{j}_i c_i & \cdots & \mathbf{j}_n c_n \end{bmatrix}^{\mathrm{T}}; \tag{A.4b}$$

$$\begin{bmatrix} \eta_{cri} \\ \eta_{czi} \end{bmatrix} = \int_{\theta=0}^{2\pi} \begin{bmatrix} \rho_a(Z_k - Z_i)\cos\theta \\ (R_i - R_k\cos\theta) \end{bmatrix} \frac{R_i\, d\theta}{|\mathbf{R}_k - \mathbf{R}_i|^3}; \tag{A.4c}$$

$$|\mathbf{R}_k - \mathbf{R}| = \sqrt{(R - R_k\cos\theta)^2 + R_k^2\sin^2\theta + \rho_a^2(Z - Z_k)^2};$$

$$B_o = \mu_0 I_o / (4\pi a_o); \mathbf{I}_c \in \mathbb{R}^{nv\times 1}; \boldsymbol{\eta}_{cr}, \boldsymbol{\eta}_{cz} \in \mathbb{R}^{1\times nv}$$

μ_o is the magnetic permeability of free space. $\mathbf{B}_{se}$ is real and can be pre-computed numerically from Eq. (A.5a) where η_{Er} and η_{Ez} are scalar given in (A.5b):

$$\frac{\mathbf{B}_{se}(\mathbf{r}_\mathbf{k},t)}{B_o} = \frac{1}{B_o}\begin{bmatrix} B_{er} \\ B_{ez} \end{bmatrix} = C_E\begin{bmatrix} \eta_{Er}(\mathbf{r}_k) \\ \eta_{Ez}(\mathbf{r}_k) \end{bmatrix}\frac{I_E(t)}{I_o} \tag{A.5a}$$

$$\text{where } \begin{bmatrix} \eta_{Er} \\ \eta_{Ez} \end{bmatrix} = \int_{\theta=0}^{2\pi}\int_{z=-1}^{1}\int_{r=\rho_i}^{\rho_o} \begin{bmatrix} \rho_a(Z_k - Z)\cos\theta \\ (R - R_k\cos\theta) \end{bmatrix} \frac{R\, dRdZd\theta}{|\mathbf{R}_k - \mathbf{R}|^3} \tag{A.5b}$$

APPENDIX B. BIOT-SAVART LAW

For the subjects are non-ferrous metal where the effects of displacement current can be neglected, the Maxwell's equations which relate the magnetic and electric fields are given by (B.1a, b) along with the constitutive relations in (B.1c, d):

$$\nabla \times \mathbf{H} = \mathbf{J};\ \ \nabla \times \mathbf{E} = -\partial \mathbf{B} / \partial t;\ \ \mathbf{B} = \mu_o \mathbf{H} \text{ and } \mathbf{J} = \sigma \mathbf{E} \qquad \text{(B.1a~d)}$$

In (B.1), **H** and **E** are the magnetic and electric field intensities respectively, **J** is the eddy-current density (ECD) induced by the time-varying magnetic fields of the EM and conductor elements; **B** is the magnetic flux density; and μ_o is the permeability of free space the EC density. Using the two fundamental magneto-static postulates that specify the divergence and curl of **B**, **B** can be expressed as the curl of the magnetic vector potential **A** defined by (B.2a) and has an integral form in (B.2b) where Ω denotes the volume of the electric conductor; and $\mathbf{r}'$ and $\mathbf{r}$ are the position vectors of the EM and the observation point respectively:

$$\mathbf{B} = \nabla \times \mathbf{A} \text{ where } \mathbf{A}(\mathbf{r}, t) = \frac{\mu_0}{4\pi} \int_{\Omega} \frac{\mathbf{J}(\mathbf{r}', t)}{|\mathbf{r} - \mathbf{r}'|} dV \qquad \text{(B.2a, b)}$$

The ECD **J** in (B.1d) can be explicitly expressed in terms of **A** by substituting **B** from (B.2a) into (B.1b) leading to

$$\mathbf{E} = -\frac{\partial \mathbf{A}}{\partial t}; \text{ hence } \mathbf{J} = -\sigma \frac{\partial \mathbf{A}}{\partial t} \qquad \text{(B.3a, b)}$$

Using (B.2a), **B** (generated by the combined effects of the input current to the EM and eddy current induced in the conductor respectively) can be derived from the curl of **A** leading to the Biot-Savart's law:

$$\mathbf{B}(\mathbf{r}) = \frac{\mu_0}{4\pi}\int_{\Omega} \frac{\mathbf{J}(\mathbf{r}')\times(\mathbf{r}-\mathbf{r}')}{|\mathbf{r}-\mathbf{r}'|^3} dV \tag{B.4}$$

APPENDIX C. MAGETIC VECTOR POTENTIAL OF A TILT EM

The Cartesian coordinate transformation from the world coordinate to an EM coordinate can be modeled as a homogeneous transformation ($\mathbf{H_{we}}$) which consists of a rotation matrix ($\mathbf{R_{we}}$) and translation matrix ($\mathbf{T_{we}}$). $\mathbf{R_{we}}$ can be formulated by rotating by an angle (θ_r) around an axis $\mathbf{n}=\begin{bmatrix} n_1 & n_2 & n_3 \end{bmatrix}^T$ [71]:

$$\mathbf{H}_{WE} = \begin{bmatrix} & \mathbf{R}_{WE} & & \mathbf{T}_{WE} \\ 0 & 0 & 0 & 1 \end{bmatrix} \tag{C.1}$$

$$\mathbf{T}_{WE} = \begin{bmatrix} t_x & t_y & t_z \end{bmatrix}^T \tag{C.2b}$$

$$\mathbf{R}_{\mathrm{WE}} = \begin{bmatrix} n_1^2 + (1-n_1^2)\cos\theta_r & n_1 n_2 (1-\cos\theta_r) - n_3 \sin\theta_r & n_1 n_3 (1-\cos\theta_r) + n_3 \sin\theta_r \\ n_1 n_2 (1-\cos\theta_r) + n_3 \sin\theta_r & n_2^2 + (1-n_2^2)\cos\theta_r & n_2 n_3 (1-\cos\theta_r) - n_1 \sin\theta_r \\ n_1 n_3 (1-\cos\theta_r) - n_2 \sin\theta_r & n_2 n_3 (1-\cos\theta_r) + n_1 \sin\theta_r & n_3^2 + (1-n_3^2)\cos\theta_r \end{bmatrix} \tag{C.3}$$

A point $\mathbf{r}_{\mathrm{p,w}}$ in the world coordinate can be transformed to the point in EM coordinate $\mathbf{r}_{\mathrm{p,e}}$ by the homogeneous transformation in (C.4). The magnetic vector potential in the world coordinate can be determined by multiplying $\mathbf{R}_{\mathrm{WE}}$ with the magnetic vector potential in the world coordinate in (C.5).

$$\mathbf{P_E} = \mathbf{H}_{EW}\mathbf{P_w} = \begin{bmatrix} \mathbf{r}_{\mathbf{p,e}}^{\mathbf{T}} & 1 \end{bmatrix}^T, \mathbf{P_w} = \begin{bmatrix} \mathbf{r}_{\mathbf{p,w}}^{\mathbf{T}} & 1 \end{bmatrix}^T \tag{C.4}$$

$$\boldsymbol{\eta}_{\mathbf{E}}\left(\mathbf{r}_{\mathbf{p,w}}\right) = \mathbf{R}_{WE} \cdot \boldsymbol{\eta}_{\mathbf{E}}\left(\mathbf{r}_{\mathbf{p,e}}, \mathbf{t}\right) \tag{C.5}$$

REFERENCES

[1] M. Mazza, P. Renaud, D. C. Bertrand, and A. M. Ionescu, "CMOS Pixels for Subretinal Implantable Prosthesis," *IEEE Sensors Journal*, vol. 5, No. 1, pp. 32-37, 2005.

[2] D. Zhou, and E. Greenbaum, Implantable Neural Prosthesis 1: Devices and Applications, Springer, 2009.

[3] G. Bonmassar, S. W. Lee, D. K. Freeman, M. Polasek,S. I. Fried , and J. T. Gale, "Microscopic magnetic stimulation of neural tissue," *Nature Communication*, Vol. 3, p921-931 , 2012.

[4] L. M. Yang, K. –M. Lee, and K. Bai, "Thermal Field Modeling Algorithm based on Flexible Space Division for High-power, High-precision Mechatronic Systems," *IEEE/ASME Int. Conf. on Advanced Intelligent Mechatronics (AIM) 2014*. Besancon, France, July-8-11, 2014.

[5] C. V. Dodd and W. E. Deeds, "Analytical Solutions to Eddy-Current Probe-Coil Problems," *J. Appl. Phys.*, vol. 39, pp. 2829-2838, 1968.

[6] J. T. Jeng, H. E. Horng, H.C. Yang, J. C. Chen, J. H. Chen, "Simulation of the magnetic field due to defects and verification using high-Tc SQUID, " *Physica C*, pp 298-302, 2002.

[7] T. P. Theodoulidis, and J. R. Bowler, "The Truncated Region Eigenfunction Expansion Method for the Solution of Boundary Value Problems in Eddy Current Nondestructive Evaluation," *AIP Conference Proceedings*, vol. 760, pp. 403-408, 2005.

[8] T. Theodoulidis and E. Kriezis, "Series Expansions in Eddy Current Nondestructive Evaluation Models," *J. of Materials Processing Technology*, vol. 161, pp. 343-347, 2005.

[9] N. D. Geeter, G. Crevecoeur, and L. Dupre, "An Efficient 3-D Eddy-Current Solver Using an Independent Impedance Method for Transcranial Magnetic Stimulation," *IEEE Trans. on Biomedical Engineering*, vol. 58, No. 2, pp. 310-320, Oct., 1984.

[10] N. D. Geeter, G. Crevecoeur, and L. Dupre, "Eddy-Current Simulations Using an Independent Impedance Method in Anisotropic Biological Tissues," *IEEE Trans. on Magnetics*, vol. 47, No. 10, pp. 3845-3848, Oct., 2011.

[11] O. P. Gandhi, J. F. DeFord, and Hiroshi Kanai, "Impedence Method for Calculation of Power Deposition Patterns in Magnetically Induced Hypertherimia," *IEEE Trans. on Biomedical Engineering*, vol. 31, No. 10, pp. 644-651, Oct., 1984.

[12] N. D. Geeter, G. Crevecoeur, and L. Dupre, "An Efficient 3-D Eddy-Current Solver Using an Independent Impedance Method for Transcranial Magnetic Stimulation," *IEEE Trans. on Biomedical Engineering*, vol. 58, No. 2, pp. 310-320, Oct., 1984.

[13] K.-M. Lee and H. Son, "Distributed multipole model for design of permanent-magnet-based actuators," *IEEE Trans. on Magnetics*, vol. 43, no. 10, pp. 3904- 391, Oct., 2007.

[14] H. Son and K. -M. Kee, "Distributed Multi-Pole Models for Design and Control of PM Actuators and Sensors," *IEEE/ASME Trans. on Mechatronics*, vol. 13, no. 2, pp 228-238, Apr., 2008.

[15] K.-M. Lee, K. Bai, and J. Y. Lim, "Dipole models for forward/inverse torque computation of a spherical motor," *IEEE/ASME Trans. on Mechatronics*, vol. 14, no. 1, pp 46-54, Feb. 2009.

[16] J. Y. Lim, and K.-M. Lee, "Distributed multilevel current models for design analysis of electromagnetic actuators," *IEEE/ASME Trans. on Mechatronics*, vol. 20, no. 5, pp 2413-2424, Oct. 2015.

[17] J. Y. Lim, and K.-M. Lee, "Design of Electromagnetic Actuators using Layout Optimization with Distributed Current Source Models," *IEEE/ASME Trans. on Mechatronics*, vol. 20, no. 6, pp 2726-2735, Dec. 2015.

[18] Humayun M, de Juan E, Dagnelie G, et al., "Visual perception elicited by electrical stimulation of the retina in blind humans," *Arch Ophthalmol*, Vol.114, p40-46.

[19] Eckmiller R, "Learning retina implants with epiretinal contacts," *Ophthalmic Research*, Vol.29, p281-289

[20] Rizzo J, Wyatt J. "Prospects for a visual prosthesis," *Neuroscientist*, Vol.3, p251-262.

[21] Chow AY, Chow VY, "Subretinal electrical stimulation of the rabbit retina," *Neurosci Lett*, Vol.225, p13-16.

[22] Zrenner E, Miliczek KD, Gabel VP, et al., "The development of subretinal microphotodiodes for replacement of degenerated photoreceptors," *Ophthalmic Res* Vol. 29, p269-280.

[23] Humayun M, Freda R, Fine I, et al. "Implanted Intraocular Retinal Prosthesis in Sin Blind Subjects," *Investigate Ophthalmology & Visual Science*, Vol. 46, p1144.

[24] Hornig R, Zehnder T, Velokay-Parel M, et al., "The IMI Retinal Implant System," *Artificial Sight, Basic Research, Biomedical Engineering, and Clinical Advances,* Chapter 6, Springer, New York, pp 111-128.

[25] Richard G, Hornig R, Keseru M, et al., "Chronic epiretinal chip implant in blind patients with retinitis pigmentosa: Long-term clinical results," Presented at *the ARVO Annu. Meeting*, Ft. Lauderdale, FL.

[26] Ralph J. J, Ofer R. Z, and Joseph F. R, III, "Threshold for Activation of Rabbit Retinal Ganglion Cells with Relatively Large, Extracellular Microelectrodes," *Investigative Ophthalmology & Visual Science*, Vol. 46, No. 4, 2005.

[27] K. H. Hsu, S. S. Nagarajan, and D.M. Durand, "Analysis of Efficiency of Magnetic Stimulation," *IEEE Trans. Biomed Eng.*, Vol. 50, No. 11, pp. 1276-1285, 2003.

[28] K. H. Hsu, and D.M. Durand, "Prediction of Neural Excitation During Magnetic Stimulation Using Passive Cable Models," *IEEE Trans. Biomed Eng.*, Vol. 47, No. 4, pp. 463-471, 2000.

[29] Ratty, F., "Analysis of Models for External Stimulation of Axons," *Journal of Theoretical Biology*, 1987, 125(3): 339-340.

[30] Ratty, F., "Ways to Approximate Current-Distance Relations for Electrically Stimulated Fibers," *IEEE Trans. on Biomedical Engineering*, 1986, 33(10): 974-977.

[31] Ratty, F., "Analysis of Models for Extracellular Giber Stimulation," *IEEE Trans. on Biomedical Engineering*, 1989, 36(7): 676-682.

[32] Roth, B.J. and P.J. Basser,"A model of the stimulation of a nerve fiber by electromagnetic induction," *IEEE Trans. on Biomedical Engineering*, 1990, 37(6): 588-597.

[33] T. A. Wagner, M. Zahn, A. J. Grodzinsky, and A. P.-Leone, "Three-dimensional head model stimulation of transcranial magnetic stimulation, " *IEEE Trans. on Biomedical Engineering*, Vol. 51, No. 9, pp. 1586–1598, Sep., 2004.

[34] L. Golestanirad, M. Mattes, J. R. Mosig, and C. Pollo, "Effect of Model Accuracy on the Result of Computed Current Densities in the Simulation of Transcranial Magnetic Stimulation," *IEEE Trans. on Magnetics*, Vol. 46, No. 12, pp. 4046–4051, Dec., 2010.

[35] S. Tsuyama, Y. Katayama, A. Hyodo, T. Hayami, S. Ueno, K. Iramina, "Effect of Coil Parameters on the Stimulated Area by Transcranial Magnetic Stimulation," *IEEE Trans. on Magnetics*, Vol. 45, No. 10, pp. 4845–4848, Oct., 2009.

[36] M. Sekino, M. Hirata, K. Sakihara, S. Yorifuji, and S. Ueno, "Intensity and Localization of Eddy Currents in Transcranial Magnetic Stimulation on the Cerebellum," *IEEE Trans. on Magnetics*, Vol. 42, No. 10, pp. 3575–3577, Oct., 2006.

[37] M. Sekino, and S. Ueno, "FEM-Based Determination of Optimum Current Distribution in Transcranial Magnetic Stimulation as an Alternative to Electroconvulsive Therapy," *IEEE Trans. on Magnetics*, Vol. 40, No. 4, pp. 2167–2169, Jul., 2004.

[38] H. A. Sodano, J.-S. Bae, D. J. Inman, and W. K. Belvin, "Concept and Model of Eddy Current Damper for Vibration Suppression of a Beam," *Journal of Sound and Vibration*, vol. 288, pp. 1177–1196. 2005.

[39] J.-S. Bae, M. K. Kwak, and D. J. Inman, "Vibration Suppression of a Cantilever Beam using Eddy Current Damper," *Journal of Sound and Vibration*, Vol. 284, pp. 805–824. 2005.

[40] L. W. Jin, J. Zheng, H. T. Li, J.P. Li, Z.J. Zhou, Y. Zhang, and Z.G. Deng, "Effect of Eddy Current Damper on the Dynamic Vibration Characteristics of High-Temperature Superconducting Maglev System," *IEEE Trans. on Applied Superconductivity*, Vol. 27, No. 3, pp. 805–824. Apr. 2017.

[41] J. Laborzenz, M. Krack, L. Panning, J. Wallaschek, M. Denk, and P.-A. Masserey, "Eddy Current Damper for Turbine Blading: Electromagnetic Finite Element Analysis

and Measurement Results," *Journal of Engineering for Gas Turbines and Power*, Vol. 134, Vol. 134, Apr. 2012.

[42] Y. Z. Hu, F. Zhao, P. Li, J. H. Chen, L. Dong, and C. Zhang, "A Novel Hybrid Excitation Eddy Current Damper for Vibration Suppression," *International Conference on Information and Automation*, Ningbo, China, pp. 642–647, August, 2016.

[43] S. C. Chen, H. S. Peng, J. A. Chang, and W. R. Jong, "Simulations and verifications of induction heating on a mold plate," *International Communications in Heat and Mass Transfer*, Vol. 31, No. 7, pp. 971–980. 2004.

[44] L. C. Meng, K. W. E. Cheng, and S. L. Ho, "Multicoils Design for Induction Cookers With Applying Switched Exciting Method, " *IEEE Trans. on Magnetics*, Vol. 48, No. 11, pp. 4053–4056, Nov., 2012.

[45] F. Moro and L. Codecasa, "A 3-D Hybrid Cell Method for Induction Heating Problems, " *IEEE Trans. on Magnetics*, Vol. 53, No. 6, Jun., 2017.

[46] Z. M. Wang, X. G. Yang, Y. H. Wang, and W. L. Yan, "Eddy Current and Temperature Field Computation in Transverse Flux Induction Heating Equipment for Galvanizing Line, " *IEEE Trans. on Magnetics*, Vol. 37, No. 5, Sep., 2001.

[47] H. Kurose, D. Miyagi, N. Takahashi, N. Uchida, and K. Kawanaka, "3-D Eddy Current Analysis of Induction Heating Apparatus Considering Heat Emission, Heat Conduction, and Temperature Dependence of Magnetic Characteristics," *IEEE Trans. on Magnetics*, Vol. 45, No. 3, Mar., 2009.

[48] G. M. Javier, G. G. Jaime, and V.-S. Ernesto, "Non-destructive techniques based on eddy current testing," *Sensors*, vol. 11, No. 3, pp. 2525–2565, 2011.

[49] M. R. Nabavi, S. N. Nihtianov, "Design strategies for Eddy-current displacement sensor systems: review and recommendations, " *IEEE Sensors Journal*, Vol. 12, No. 12, pp. 3346–3355. Dec. 2012.

[50] T. Yamaguchi, Y. Iwai, S. Inagak, M. Ueda, "A method for detecting bearing wear in a drain pump utilizing an eddy-current displacement sensor, " *Measruement*, Vol. 33, No. 3, pp. 205–211. April, 2003.

[51] G. Mook, O. Hesse, and V. Uchanin, "Deep Penetrating Eddy Currents and Probes, " *Material Testing*, vol. 49, no. 5, pp 258-264, May, 2007.

[52] T. Dogaru and S. T. Smith, "Giant Magnetoresistance-based Eddy-Current Sensor, " *IEEE Trans. on Magnetics*, Vol. 37, No. 5, pp. 3831-3838, Sep., 2001.

[53] J.-T. Jeng, G.-S. Lee, W.-C. Liao, and C.-L. Shu, "Depth-Resolved Eddy-Current Detection with GMR Magnetometer," *Journal of* Magnetism and Magnetic Material, pp. 470-473, 2006.

[54] N. Bowler, and Y. Q. Huang, "Electrical Conductivity Measurement of Metal Plates Using Broadband Eddy-Current and Four-Point Methods, " *Measurement Science and Technology*, vol. 16, no. 11, pp 2193-2200, Sep., 2005.

[55] X. Ma, and A. J. Peyton, "Eddy Current Measurement of the Electrical Conductivity and Porosity of Metal Foams, " *IEEE Trans. on Instrumentation and Measurement*, vol. 55, no. 2, pp 570-576, Apr., 2006.

[56] X. Ma, A. J. Peyton, and Y. Y. Zhao, "Measurement of the Electrical Conductivity of Open-celled Aluminum Foam Using Non-contact Eddy Current Techniques, " *NDT&E International*, vol. 38, no. 5, pp 359-367, Jul., 2005.

[57] M. Weiss, C. Wacharamanotham, S. Voelker, and J. Borchers, "Finger Flux: Near-surface haptic feedback on tabletops," *in Proc. of the 24th annual ACM symposium on User interface software and technology*, Santa BarBara, CA, USA, Oct. 16-19, 2011.

[58] T. H. Yang, S. Y. Kim, C. H. Kim, D. S. Kwon, and W. J. Book, "Development of a miniature pin-array tactile module using elastic and electromagnetic force for mobile devices," *Third Joint Eurohaptics Conference and Symposium on Haptic Interfaces for Virtual Environment and Teleoperator Systems*, Salt Lake City, UT, USA, March 18-20, 2009, pp. 13-17.

[59] F. Vidal-Verdu and M. Hafez, "Graphical tactile displays for visually-impaired people," *IEEE Trans. on Neural Systems and Rehabilitation Engineering*, vol. 15, no. 1, pp. 119–130, March, 2007.

[60] M. Benali-Khoudja, M. Hafez, J.-M. Alexandre, A. Kheddar, and V. Moreau, "VITAL: a new low-cost vibro-tactile display system," *in Proc. of the 2004 IEEE ICRA*, New Orleans, LA, USA, April 26-May 1, vol. 1, pp. 721-726.

[61] M. Weiss, F. Schwarz, S. Jakubowski, and J. Borchers. "Madgets: actuating widgets on interactive tabletops," *in Proc. of the 23nd annual ACM symposium on User interface software and technology*, New York, NY, USA, Oct. 3-6, 2010, pp. 293-302.

[62] M. Weiss, C. Remy, and J. Borchers, "Rendering physical effects in tabletop controls," *in Proc. of SIGCHI Conference on Human Factors in Computing Systems*, Vancouver, BC, Canada, May 7-12, 2011, pp. 3009-3012.

[63] M. Weiss, C. Wacharamanotham, S. Voelker and J. Borchers, "Finger Flux: near-surface haptic feedback on tabletops," in *Proc. 24th Annual ACM Symp. on User Interface Software and Technology*, Santa BarBara, CA, USA, Oct. 16-19, 2011.

[64] K. M. Lee, K. Bai and J. Y. Lim, "Dipole Models for Forward/Inverse Torque Computation of a Spherical Motor, " *IEEE/ASME Trans. on Mechatronics*, vol. 14, no. 1, pp 46-54, 2009.

[65] E. Diller, S. Floyd, C. Pawashe and M. Sitti, "Control of Multiple Heterogeneous Magnetic Micro-robots in two Dimensions on Non-specialized Surfaces, " *IEEE Trans. on Robotics*, vol. 28, no. 1 pp 172-182, 2012.

[66] M. P. Kummer, J. J. Abbott, B. E. Kratochvil, R. Borer, A. Sengul and B. J. Belson, "OctoMag, An Electromagnetic System for 5-DOF Wireless Micro-manipulation, " IEEE Trans. on Robotics, vol. 26, no. 6, pp. 1006-1017, 2010.

[67] X. R. Cao, D. Y. Cai, X. D. Zhang, R. T. Liu and J. T. Tang, "Optimization of Electric Field Distribution of Multichannel Transcranial Magnetic Stimulation based on Genetic Algorithm, " in 3rd Int. Conf. on BMEI, Yantai, China, Oct. 16-18, 2010, pp. 1544-1547.

[68] S. Yang, G. Xu, L. Wang, Y. Geng, H. Yu and Q. Yang, "Circular Coil Array Model for Transcranial Magnetic Stimulation, " IEEE Trans. on Applied Superconductivity, vol. 20, no. 3, pp. 829–833, 2010.

[69] M. Gramz and T. Stepinski, "Eddy-current Image, Array Sensors and Flaw Reconstruction, " Res. Nondestruct. Eval., vol.5, p157-17, 1994.

[70] G. Mook, F. Michel and J. Simonin, "Electromagnetic Imaging using Probe Arrays," *Journal of Mechanical Engineering*, vol. 57, no. 3, pp. 227-236, 2011.

[71] D. F. Rogers and J. A. Adams, *Mathematical Elements for Computer Graphics*. New York, NY: McGraw-Hill, 1976.

[72] C. Y. Chan, and C. Nicholson, "Modulation by applied electric fields of Purkinje and stellate cell activity in the isolated turtle cerebellum," *J. Physiol.* 371, pp. 89-114, 1986.

[73] I. Bekerman, P. Gottlieb, and M. Vaiman, "Variations in Eyeball Diameters of the Healthy Adults," *J. of Ophthalmology*, Nov., 2014.

[74] A. Dichtl, J. B. Jonas, G. O.H. Naumann, "Retinal nerve fiber layer thickness in human eyes," Graefes Arch Clin Exp Ophthalmol., 1999 Jun, Vol. 6, p474-479.

[75] C. J. Karwoski and X. Xu, "Current source-density analysis of light-evoked field potentials in rabbit retina," *Visual neuroscience*, vol. 16, pp. 369-377, 1999.

[76] H. A. Haus and J. R. Melcher, Electromagnetic fields and energy: Prentice Hall Englewood Cliffs, New Jersey, 1989.

[77] S. Gabriel, R. W. Lau, and C. Gabriel, "The dielectric properties of biological tissues: III. Parametric models for the dielectric spectrum of tissues," *Phys. Med. Biol.*, vol. 16, pp. 2271-2293, 1996.

[78] K.-M. Lee, C.-Y. Lin, B.J. Hao, and M. Li, "Coupled Parametric Effects on Magnetic Fields of Eddy-Current Induced in Non-Ferrous Metal Plate for Simultaneous Estimation of Geometrical Parameters and Electrical Conductivity," *IEEE Trans. on Magnetics*, vol. 53, no.10, pp. 1-9, 2017.